



THE UNIVERSITY *of* EDINBURGH

This thesis has been submitted in fulfilment of the requirements for a postgraduate degree (e.g. PhD, MPhil, DClinPsychol) at the University of Edinburgh. Please note the following terms and conditions of use:

This work is protected by copyright and other intellectual property rights, which are retained by the thesis author, unless otherwise stated.

A copy can be downloaded for personal non-commercial research or study, without prior permission or charge.

This thesis cannot be reproduced or quoted extensively from without first obtaining permission in writing from the author.

The content must not be changed in any way or sold commercially in any format or medium without the formal permission of the author.

When referring to this work, full bibliographic details including the author, title, awarding institution and date of the thesis must be given.

Modelling 3D Blockage Effects for Millimetre-Wave Communication Systems

Fahd Nasser Alsaleem

Supervised By: Prof. John S. Thompson



The thesis is submitted for the degree of Doctor of Philosophy
Institute for Digital Communications (IDCOM)
The School of Engineering
THE UNIVERSITY of EDINBURGH
October 2020

Abstract

The millimetre wave (mmWave) band, which has a frequency range of 30-300 GHz, can provide the desired requirements for future communication systems, such as wide bandwidth and high data-rate with very low latency. However, these advantages entail several consequences and challenges: compared with the microwave band, below 6 GHz, the mmWave band not only suffers from increased path loss but also higher sensitivity to blockage effects due to very short wavelengths. Considering the mmWave band, a human blockage, for example, could severely affect the transmitted signal by causing attenuation of 20 dB or more. With motion, the attenuation problem becomes even more serious. The rapid changes of dynamic blockages surrounding a moving transceiver can cause a significant and sudden impact on channel attenuation, which affects the overall quality of service for mmWave systems. The main scope of this thesis is to develop new mathematical models that accurately capture the dynamics of blockers affecting a moving transceiver in order to compute the resulting channel attenuation accurately.

The first Markov chain model studied in this work follows a simple approach by assigning a fixed-attenuation value to each blocker and using a geometric model to generate the transition probability matrices. The transition probabilities are calculated both analytically and via a geometric simulation, where the results are found to match well. The proposed model successfully captures the dynamics of the channel caused by blockers surrounding a moving transceiver. The model works well for stationary scenarios, and the proposed technique of switching between several Markov chains makes the model applicable to a non-stationary average number of blockers as well.

The adaptive sum of Markov chains (sum of MC) is another proposed model, which can model the dynamics of blockage effects more accurately than the simpler Markov Chain model. It is adaptive to non-stationary scenarios in any given environment, and it efficiently captures the dynamics of blockages arising from a moving transceiver. The sum of Markov chains model can integrate any desired attenuation function, in-

cluding the third-generation partnership project (3GPP) blockage model and any lab measurement attenuation profile. The sum of MC model could be a very useful tool for communication engineers, allowing them to perform an initial mmWave coverage analysis for a given environment in the presence of time-varying blockage effects.

Unlike human blockage, which has been widely studied in the literature, the impact of other small objects on signal strength, such as metal road signs, is not so well understood. This thesis has carried out a measurement campaign for these small blockers, which induce measured loss in the range of 15- 30 dB, depending on the type and size of the blocker. The thesis also compares those results with existing simulation blockage models for these small objects. These blockage models include the 3GPP model, the multiple knife-edge (MKE) model, and the mmMAGIC model, where the latter two models show a better fit to the measured attenuation of relatively small blockers than the 3GPP model. Finally, the thesis evaluates the impact of blockers on the overall performance of mmWave multiple-input multiple-output (MIMO) wireless systems, where a ray-tracing tool is used to establish all possible propagation paths for a moving transceiver in an outdoor scenario. The performance impact of the measured attenuation profiles for road signs are evaluated for an outdoor scenario using the sum of MC model.

Lay Summary

The innovation technology wave, especially in the communications field, is expected to continue growing in the next few years. Phones are becoming smarter, home devices are getting connected, and there is intensive work to build completely driverless vehicles. With more and more devices getting connected, there is an enormous data load to be shared over the communication networks. The fifth-generation (5G) and beyond wireless communication systems must have the ability to meet all the high demands of these applications, some of which are only one-millisecond point-to-point delay for transferring data, a high data rate in the range of Gigabits per second (Gbps), up to $100 \times$ the number of connected devices compared with a 4G network, and improved coverage and reliability.

Implementing new technologies are required for achieving these tremendous goals. The enormous available bandwidth in the millimetre wave (mmWave) bands, which is in the range 30 to 300 gigahertz (GHz), makes it a very promising solution. Although the mmWave band is a promising approach for providing the desired requirements of 5G communications, susceptibility to blockage is one of the challenging aspects needed to be addressed. For instance, the human blockage weakens the mmWave signal to be 0.1 % to 1 % of its original power. The issue is even more challenging when the user moves through the environment. The sudden drop in the signal power, due to the appearance of blockers, makes the communication link unreliable. Understanding the behaviour of the blockage effects is the first step towards resolving this issue. There is a need for a three-dimensional (3D) blockage modelling to enable telecommunications companies to have an initial coverage study in the presence of blockers. Although the more advance modelling approaches that have a 3D visualisation of the environment give a reasonable approximation of reality, they are computationally intensive. One of the main contributions of this thesis is to provide very efficient 3D blockage models that are based on a probabilistic blockage approach. This thesis investigates the blockage effects on the mmWave signal strength, and it provides a comprehensive

analysis of the channel attenuation introduced by blockages. The work of this thesis, also, contributes to understanding the effects of small-size blockers on the signal strength. It provides tools to investigate the received data rates of mmWave systems in the presence of blockers.

Acknowledgements

First and foremost, I am very grateful for almighty God, *Allah*, for blessing, giving me the strength, and knowledge to achieve the goal.

I sincerely express my deep sense of gratitude to the great supervisor, ***Prof. John S. Thompson***, for his endless support and valuable advice through this unique journey. I am short of words to thank him for being very patient, supportive, and very helpful during the whole period of my study. He believed in me, and his encouragement and guidance helped me to build my skills as an academic researcher. Our meetings have been inspiration times. I would always be grateful to him.

I would also like to thank my second supervisor, ***Dr David I. Laurenson***, for providing incredible support whenever needed. Also, I am grateful to *Cristian A Alistarh*, and his supervisor, *Dr Symon K. Podilchak*, for allowing access to Heriot-Watt University's RF lab, and for their great help in setting the measurements. Also, Thanks to my examiners, *Dr Tim Brown* and *Dr Chang Liu* for an intellectually stimulating viva.

To my great father, *Nasser*, death may have taken you away from me when I was a little boy, but your love will continue to grow with me, and you will always be missed. To my great mother, *Huda*, who raised me with heartfelt love and guidance, I would never be able to thank you enough. Many thanks to my wife, *Norah*, who has shared the great and tough times with me through this journey. To my family: *Nasser, Shadden, Almuthanna, Turki, Mada, and Saja*, thank you for your support and encouragement.

To all my great friends in Edinburgh, thank you for turning this journey to be a very joyful time.

Last but not least, special thanks go to the *Saudi government* and *Qassim University* who sponsored my study and gave me this great chance; I promise you to return-back and help to build a great nation.

Contents

Title Page	i
Abstract	ii
Lay Summary	iv
Acknowledgements	vi
Contents	vii
List of figures	xi
List of tables	xv
Acronyms and Abbreviations	xvi
Notations	xix
Symbols	xx
 1 Introduction	 1
1.1 Brief Background	1
1.2 Thesis Motivation and Contributions	3
1.3 Thesis Outlines	4
 2 Background	 6
2.1 Millimetre-wave Spectrum Overview	6
2.1.1 Main Advantages of mmWave	7
2.1.2 Challenges of mmWave	7
2.1.3 Some Possible Approaches to Overcoming the mmWave Chal- lenges	8
2.1.4 5G Requirements versus mmWave Advantages	9
2.1.5 Applications of mmWave	9
2.2 Propagation	10
2.2.1 Free Space Propagation	11
2.2.2 Reflection and Scattering	11
2.2.3 Huygens' Principle	12
2.2.4 Fresnel Zone	12
2.2.5 Diffraction Phenomena	13
2.2.6 Knife-edge Diffraction	13
2.3 Propagation Loss Factors	17
2.3.1 Free Space Path loss	18
2.3.2 Atmospheric Attenuation	20
2.3.3 Rain Attenuation	20
2.3.4 Foliage Attenuation	21
2.3.5 Material Penetration and Blockage Loss	21
2.4 mmWave Channel Models	22
2.4.1 AWGN Channel Capacity and Spectral Efficiency	22
2.4.2 mmWave MIMO Overview	24

2.4.3	Narrowband channel model	25
2.4.4	MIMO Channel Capacity	26
2.4.5	Beamforming Overview	28
2.4.6	Beam Switching for Resolving Blocked Path	29
2.4.7	Existing Standardisations and Projects for mmWave Channel Models	29
2.5	Blockage Modelling	30
2.5.1	The Importance of Understanding the Dynamic Blockage Effect on the mmWave Channel	31
2.6	Finite-State Markov Chain Model	32
2.7	Thesis Main Research Scope	33
2.8	Conclusion	33
3	Markov Chain for Modelling 3D Blockage In mmWave V2I Communications	34
3.1	Introduction	34
3.1.1	Considered Application (Vehicular Communications)	34
3.1.2	Possible Propagation Modelling Approaches	35
3.1.3	Main Contributions	37
3.2	The 3D Geometric Blockage Model	37
3.2.1	System Model	37
3.2.2	The Receiver Track Scenarios	40
3.2.3	Propagation Cases	41
3.2.4	Spectral Efficiency	43
3.2.5	Geometric Model Computation Process	45
3.3	The Markov Chain Model	45
3.3.1	Overview of Markov Chain	46
3.3.2	Straight-line Scenario and the Markov Reducible Characteristic	46
3.3.3	Converting the 3D Blockage Geometric Model into a Markov Chain Model	48
3.3.4	Transition Probability Matrices	49
3.3.5	One Markov Chain Model for the Stationary Scenario (Circle)	52
3.3.6	Multiple Markov Chain Model for the Non-stationary Scenario (Straight-line)	54
3.4	Comparisons and Results	57
3.4.1	Circular Scenario Results Comparisons	58
3.4.2	Straight-line Scenario Results Comparisons	60
3.4.3	Transition Probability (Simulation versus Analytical)	61
3.5	Conclusion	63
4	Adaptive Sum of Markov Chains for Modelling 3D Blockage in mmWave V2I Communications	64
4.1	Introduction	64
4.1.1	Limitations of the Simple Markov chain model of Chapter 3	65
4.1.2	Related Work on Human Blockage	65

4.1.3	How have human blockers been modelled in the literature? . .	67
4.1.4	The Main Contributions	67
4.1.5	Chapter Organisation	68
4.2	The System Model	69
4.2.1	Introducing the system model parameters	70
4.2.2	Propagation scenarios	72
4.2.3	Channel Capacity	73
4.3	Blockage Attenuation Approaches	74
4.3.1	Approach (1): Fixed-Attenuation Blockage Model	74
4.3.2	Approach (2): 3GPP Blockage Model	74
4.3.3	RF Lab Measurements	76
4.4	Methods to Model Blockages in Computer Simulation	77
4.4.1	The Geometric Model	78
4.4.2	Markov Chain Model	81
4.5	Sum of Markov Chains Model	82
4.5.1	Introducing the model	82
4.5.2	Analytical Calculation of Average Number of Blockers	83
4.5.3	Average Number of Blockers by Simulation	87
4.5.4	Blockage Attenuation	88
4.5.5	Complexity Order of the Adaptive Sum of MC Model:	88
4.6	Results and Discussions	89
4.6.1	Stationary Scenario: Circular-track Comparisons	90
4.6.2	Non-stationary Scenario Comparisons	95
4.6.3	Results of Integrating Lab measurements into the Sum of MC Model	100
4.7	Conclusion	101
4.8	Software	102
5	Small-Size Blockage Propagation Modelling for mmWave Communica- tions Systems	103
5.1	Introduction	103
5.2	Blockage Modelling Approaches	107
5.2.1	Model (1): 3GPP Blockage:	108
5.2.2	Model (2): Including the Antenna Gain:	109
5.2.3	Model (3): Multiple Knife-edge Diffraction (MKE):	111
5.2.4	Model (4): The mmMAGIC Blockage Model:	111
5.3	Modelling mmWave Channel with Ray-tracing	112
5.3.1	Channel Modelling	113
5.3.2	Simple Directional Beamforming Technique	114
5.3.3	The Spectral Efficiency of each path	114
5.3.4	Integrating Blockage with Channel Modelling	114
5.3.5	Simple Switching-beams Technique	116
5.4	Measurement Settings	116
5.4.1	Blockers Types and Sizes	118
5.5	Results and Discussions	118

5.5.1	Part 1 Results: Factors Affect the Attenuations of 3GPP . . .	119
5.5.2	Part 2 Results: Attenuation of the 5 Small Blockers (Lab-Measurements versus the 4 KED Simulation Models)	122
5.5.3	Part 3 Results: Blocker effects on the mmWave channel . . .	132
5.6	Conclusions	135
6	Conclusions and Future Work	137
6.1	The Research Questions and The Novelty of the Work	137
6.2	Conclusions of The Main Contributions	138
6.2.1	Modelling the Dynamic Channel Attenuation for V2I mmWave Communications	138
6.2.2	Small-sized Blockage Propagation Modelling for mmWave Bands	139
6.2.3	Evaluation of the Signal Strength of mmWave MIMO Systems for a Multi-path Scenario in the Presence of Blockers	140
6.3	Future Work	141
6.3.1	Multiple Transmitters and Small Cells	141
6.3.2	Multiple Blocker Measurements	141
6.3.3	The V2V Systems	141
A	List of Publications	143
A.1	Conference Papers	143
A.2	Journal Papers	143

List of figures

1.1	User-demands in the United States versus the LTE capacity limits. This figure is adopted from [1]. PB stands for petabyte.	2
2.1	The eight key factors that are targeted for the future 5G system. This figure is adopted from [2]. IMT-2020 represents the 5G systems, which is named by ITU-R, and it stands for International Mobile Telecommunications (IMT) for 2020 and beyond, while IMT-Advanced represents 4G systems and it stands for International Mobile Telecommunications-Advanced.	8
2.2	Diffraction and Huygens secondary source [3,4].	12
2.3	Fresnel zones.	13
2.4	Simplified KED model [3,4].	14
2.5	Knife-edge diffraction loss: 3GPP's approximation [5], Lee's approximation [6], and the exact calculation of the path loss [7].	17
2.6	The free space path loss over distance for several LTE bands, WiFi bands, and multiple mmWave bands.	18
2.7	The atmospheric absorption of mmWave. The figure shows the curves of Oxygen (O_2), water vapour (H_2O), and rain at sea level versus the carrier frequency. The density of (H_2O) is in g/m^3 is presented by the symbol. This figure is adopted from [8], which is originally generated from [9,10].	19
2.8	Simplified configuration of MIMO System.	24
2.9	MIMO spectral efficiency, with respect to the SNR, with a different number of TX and RX antenna arrays compared with Shannon channel capacity [11]. These capacity results are for the i.i.d. Rayleigh fading channel.	27
2.10	Example of 2-States Markov chain model.	32
3.1	An example the 3D geometric blockage model	38
3.2	The of the 3D geometric model. (a) Circular. (b) Straight-line.	40
3.3	The received power with and without a blocker crossing the LOS between BS and RX. For the brown doted curve we have one blocker that is located at random location with each run, 20 sample points, and $M=10$ runs.	43
3.4	The received spectral efficiency with and without a blocker crossing the LOS between BS and RX. For the green doted curve we have one blocker that is located at random location with each run, 20 sample points, and $M=10$ runs.	44
3.5	Example of reducible and irreducible Markov chains.	47

3.6	Example of Markov chain with 3 states representing 0, 1 or 2 blockers.	49
3.7	The best value of the transition probability P_{11} .	51
3.8	The Transition Probability Matrix of a circular scenario. The No. of $N_{BL}=200$, 400 RX sample points, and $M=50$ runs.	53
3.9	Average number of blockers seen by the moving transceiver - the circular scenario. The No. of $N_{BL}=200$, 400 RX sample points, and $M=50$ runs.	53
3.10	The Average number of blockers seen by the moving transceiver - the straight-line scenario. There are 34001 RX sample points along the RX track, which is divided into 11 sectors.	54
3.11	The gradient of the average number of blockers seen by a mobile transceiver - the straight-line scenario	56
3.12	Average ACF of the Capacity of the circular track with No. of BL=100, several radii, 400 sample points, and $M=150$ runs	59
3.13	The ECDF of the Capacity of the circular track with No. of BL=10, $r=15$ m, 400 sample points, and $M=150$ runs	59
3.14	The Average ACF of the Capacity of the straight-line track with No. of BL=50, $P_{BL} = 20$ dB, 34001 sample points, and $M=100$ runs	60
3.15	The ECDF of the Capacity of the straight-line track with No. of BL=50, 34001 sample points, and $M=100$ runs	61
3.16	Analytical and simulation comparison. (a) P_{01} . (b) P_{11} .	62
4.1	The System Model.	70
4.2	Shadowing screen model adopted from [5, 12].	75
4.3	Shadow of two overlapped blockers.	75
4.4	Lab-measurement - Attenuation caused by a rectangular copper sheet.	77
4.5	Scenarios of the Geometric Model.	79
4.6	Two Markov Chain Model states for one chain of the sum of MC.	82
4.7	Diagram explains the process of the sum of Markov Chains Model.	83
4.8	The relationship's curve between the input P_{01} and the output N'_S of the sum of Markov chains function, where $l_B = 30$ and $n = 5$.	87
4.9	Average ACF of the Capacity of the circular track, $r=10$ m, with No. of BL=200, 360 sample points, and $M=100$ runs - Fixed Attenuation.	93
4.10	The ECDF of the Capacity of the circular track, $r=10$ m, with No. of BL=200, 360 sample points, and $M=100$ runs - Fixed Attenuation.	93
4.11	Average ACF of the Capacity of the circular track, $r=10$ m, with No. of BL=300, 360 sample points, and $M=500$ runs - 3GPP Blocker.	94
4.12	The ECDF of the Capacity of the circular track, $r=10$ m, with No. of BL=300, 360 sample points, and $M=500$ runs - 3GPP Blocker.	94
4.13	Average number of blockers along the MT straight-line track with No. of BL=130, $r_{BL} = 0.55$ m, 34001 MT sample points, sample space $\lambda/2$, and $M=100$ runs - Fixed Attenuation.	96
4.14	The Average ACF of the Capacity of the straight-line track with No. of BL=130, $r_{BL} = 0.55$ m, 34001 MT sample points, sample space $\lambda/2$, and $M=100$ runs - Fixed Attenuation.	97

4.15	The ECDF of the Capacity of the straight-line track with No. of BL=130, $r_{BL} = 0.55$ m, 34001 MT sample points, sample space $\lambda/2$, and $M=100$ runs - Fixed Attenuation.	97
4.16	Average number of blockers along the MT Cosine-shape track with No. of BL=200, $r_{BL} = 0.2821$ m, 500 sample points, and $M=500$ runs - Fixed Attenuation.	98
4.17	The Average ACF of the Capacity of the Cosine track with No. of BL=200, $r_{BL} = 0.2821$ m, 500 sample points, and $M=500$ runs - Fixed Attenuation.	99
4.18	The ECDF of the Capacity of the Cosine track with No. of BL=200, $r_{BL} = 0.2821$ m, 500 sample points, and $M=500$ runs - Fixed Attenuation.	100
5.1	KED Shadowing screen model: (a) One screen blockage model [5] that represents the following models: 3GPP, 3GPP+antenna gain, and mmMAGIC. (b) Multiple KED screens [13] that represents the MKE model.	108
5.2	Cross-sectional view of the main antenna pattern and blocker.	110
5.3	3D View of the ray-tracing scenario.	113
5.4	A flowchart that shows how the measured blockage attenuation profiles, provided in this chapter, are integrated into the ray-tracing model of an outdoor scenario. The integration is done by a single Markov chain function based on Chapter 4 (published in [14]). This flowchart applies for each path independently.	115
5.5	The rectangular metal sheet blocking the LOS in the anechoic chamber.	117
5.6	Blockage attenuation versus blocker width in terms of λ . Comparison between measurements, 3GPP model (5.4), 3GPP (including the antenna gain) (5.5), and MKE model (X-shape) (5.7). The centre carrier frequency is 28 GHz.	119
5.7	Blockage attenuation versus blocker screen orientation, in degrees, referred to the LOS path. Four scenarios of the 3GPP model (5.4); two screens size at two different TX-RX dis The centre carrier frequency is 28 GHz.	121
5.8	The attenuation of BL(1): (16.5 cm by 16.5 cm) metal sheet. Comparison between measurements and the following models: a) 3GPP eq. (5.4), b) 3GPP (including the antenna gain) eq. (5.5), c) MKE (+)-shape eq. (5.7), and d) mmMAGIC eq. (5.8). The centre carrier frequency is 28 GHz.	123
5.9	The attenuation of BL(2)- Scenario (1): (36 cm by 28.2 cm) metal sheet. TX-RX distance is 2 m. Comparison between measurements and these models: a) 3GPP (4-sided eq. (5.2) & 2-sided eq. (5.4)), b) 3GPP (including the antenna gain) eq. (5.5), c) MKE (X)-shape eq. (5.7), d) mmMAGIC eq. (5.8). The carrier frequency is 28 GHz.	124

5.10	The attenuation of BL(2) - Scenario (2): (36 cm by 28.2 cm) metal sheet. Comparison between measurements and the following models: a) 3GPP eq. (5.4), b) 3GPP (including the antenna gain) eq. (5.5), c) MKE (X)-shape eq. (5.7), d) mmMAGIC eq. (5.8). The carrier frequency is 28 GHz.	125
5.11	The attenuation of BL(3): (33 cm by 33 cm) metal sheet for three different frequencies. Comparison between measurements and the following models: a) 3GPP eq. (5.4), and b) mmMAGIC eq. (5.8)	126
5.12	The attenuation of BL(4)- Scenario (1): the plastic cylinder. Comparison between measurements and these models: a) 3GPP eq. (5.4), b) Vertical 3GPP eq. (5.4), c) 3GPP (including the antenna gain) eq. (5.5), d) MKE (+)-shape eq. (5.7), and e) mmMAGIC eq. (5.8). The carrier frequency is 28 GHz.	127
5.13	The attenuation of BL(4): the plastic cylinder. Comparison between measurements and the following models: a) 3GPP eq. (5.4), b) Vertical 3GPP eq. (5.4), c) 3GPP (including the antenna gain) eq. (5.5), d) MKE (+)-shape eq. (5.7), and e) mmMAGIC eq. (5.8). The centre carrier frequency is 28 GHz.	128
5.14	The attenuation of BL(5): the metallic cylinder. Comparison between measurements and the following models: a) 3GPP eq. (5.4), b) 3GPP (including the antenna gain) eq. (5.5), c) MKE (+)-shape eq. (5.7), and d) mmMAGIC eq. (5.8). The centre carrier frequency is 28 GHz.	129
5.15	A flowchart summarizes Part 2 results, i.e. Section 5.5.2, and explains which blockage simulation model would fit the measurements better. .	130
5.16	The received SE (1 run) at a sector of the RX track in the presence of two blocker-types: $BL(3)$ and $BL(5)$. The first path, the second path, and selecting the highest among the two. In the first two subplots, the red curves represent the lab-measured attenuation of the blockers while the blue curves are the simulated attenuation (3GPP for $BL(3)$ and mmMAGIC for $BL(5)$).	133
5.17	The ECDF of the received SE of 15000 RX sample points along the (150 m) RX trajectory - 20 runs. Two cases: high and low blockage probabilities, $P_{01} = 0.35$ & $P_{01} = 0.0005$. For each case, three curves: 1) LOS Path. 2) Reflected-Path. 3) Selecting the non-blocked path among them.	134
6.1	Flowchart summarises all the main points of the thesis.	140

List of tables

2.1	The main mmWave Channel Models over the last two decades. The content of the table is chosen from [8].	30
3.1	System and Antenna Parameters	45
3.2	System and Antenna Parameters	57
3.3	Comparison between Markov chain and the Geometric models	58
4.1	System and Antenna Parameters	90
4.2	Overall Channel Capacity C & Average Number of Blockers N' comparison between the three models: 1) Geometric, 2) Markov chain (MC) model, and 3) sum of Markov chains (sum of MC) - Two Circular Shape Scenarios both with Fixed Attenuation Blockage Model . .	91
4.3	The average number of blockers N' comparison between all three models: 1) Geometric (simulation and theoretically), 2) Markov chain model, and 3) the sum of Markov chains (simulation and theoretically) - Fixed attenuation blockage model	92
5.1	Lab Measurement Settings	117
5.2	Frequency Comparison based on the Mean Value of the Main Body of the Measured Attenuation for All Blockage Models.	131
5.3	Comparisons Between the Simulation Blockage Models Based on MSE - Measurements are the Reference Point - $f_c=28$ GHz	131
5.4	The average received spectral efficiency (bits/s/Hz) for the first path, second path, and the best of them. Three different blockage probabilities and two blockers type ($BL(3)$ 33-Metal sheet and $BL(5)$ Metallic cylinder).	134

Acronyms and Abbreviations

2D	Two Dimensional
2G	second-generation
3D	Three Dimensional
3GPP	Third Generation Partnership Project
4G	Fourth Generation
5G	Fifth Generation
5GCM	5G Channel Models
ACF	Autocorrelation Function
AM	Amplitude Modulation
AWGN	Additive White Gaussian Noise
AoA	Angles of Arrival
AoD	Angles of Departure
BER	Bit-Error Rate
BF	Beamforming
BL	Blocker
BS	Base Station
CSI	Channel State Information
dB	Decibel
DKE	Double Knife Edge
ECDF	Empirical Cumulative Distribution Function
FM	Frequency Modulation
FSMC	Finite-State Markov Channel
FSPL	Free Space Path Loss
FWA	Fixed–Wireless Access
GSCM	Geometry Based Stochastic Channel Model
GTD	Geometrical Theory of Diffraction
HPBW	Half Power Beamwidth
I.I.D.	Independent and Identically Distributed

IMT	International Mobile Telecommunications
IoT	Internet of Things
ITU	International Telecommunication Union
ITU-R	International Telecommunication Union Radiocommunications
KED	Knife-Edge Diffraction
LiDAR	Light Detection and Ranging
LOS	Line of Sight
LTE	Long Term Evolution
MC	Markov Chain
METIS	Mobile and wireless communications Enablers for the Twenty-twenty Information Society
MIMO	Multiple-Input Multiple-Output
MKE	Multiple Knife-Edge
MMB	Mobile Broadband
mmMAGIC	Millimetre Wave Based Mobile Radio Access Network for Fifth Generation Integrated Communications
MMSE	Minimum Mean Squared Error
mmWave	Millimetre wave
MSE	Mean Squared Error
MT	Mobile Transceiver
NLOS	Non-Line of Sight
OFDM	Orthogonal Frequency-division Multiplexing
PPP	Poisson Point Process Distribution
QoS	Quality of Service
QuaDRiGa	Quasi Deterministic Radio Channel Generator model which is (Extension of WINNER II)
RaDAR	Radio Detection and Ranging
RF	Radio Frequency
RX	Receiver
SE	Spectral Efficiency
SISO	Single Input Single Output
SNR	Signal to Noise Ratio

Sum of MC	Sum of Markov Chains
SVD	Singular Value Decomposition
TGad	Task Group ad
UDNs	Ultra-Dense Networks
UPA	Uniform Plane Array
UTD	Uniform Geometrical Theory of Diffraction
V2I	Vehicle-to-Infrastructure
V2V	Vehicle-to-Vehicle
V2X	Vehicle-to-Everything
VR	Virtual Reality
WPAN	Wireless Personal Area Network
WiFi	Wireless Fidelity
WINNER	Wireless World Initiative New Radio
WLAN	Wireless Local Area Network

Notations

a <u>OR</u> A	Scalar
\mathbf{a}	Vector
\mathbf{A}	Matrix
\mathbf{A}^H	Complex conjugate transpose of \mathbf{A}
nC_k	Binomial coefficient which equals to $\binom{n}{k} = \frac{n!}{k!(n-k)!}$
$\text{atan}(x)$	Returns the inverse tangent (\tan^{-1}) of x in radians
$\mathcal{CN}(a, \mathbf{A})$	Complex Gaussian vector; mean (a), covariance \mathbf{A}
$ \cdot $ <u>OR</u> $\det(\cdot)$	Determinant operator
$\mathbb{E}(\cdot)$	Expectation operator
e <u>OR</u> $\exp(\cdot)$	Exponential function
\mathbf{I}	Identity matrix
\log	Logarithmic function with base 10
\log_x	Logarithmic function with base x
$\max(\cdot)$	Maximum value function
$\text{mod}(\cdot)$	Remainder after division function
$\min(\cdot)$	Minimum value function
$P(A B)$	Probability of A given B
$\mathcal{O}(\cdot)$	Complexity-order function
$\text{sgn}(\cdot)$	The signum function. It extracts the sign of a real number.
$\mathbf{X} \in \mathbb{C}^{A \times B}$	$A \times B$ size \mathbf{X} matrix with complex entries
$\mathbf{X} \in \mathbb{R}^{A \times B}$	$A \times B$ size \mathbf{X} matrix with real entries
$\sum_{i=1}^N x_i$	Sum the values of x , starting at x_1 and ending with x_N
$\prod_{i=1}^N x_i$	Multiply the values of x , starting at x_1 and ending with x_N

Symbols

A_{eff}	Effective area of an antenna (aperture)
A_T	The total area between TX BS and RX MT
$\mathbf{a}_T, \mathbf{a}_R$	Transmitter and receiver steering vectors respectively
$\alpha_{j,i}$	Complex gain of cluster j and path i
$BL(1)$	Small square sheet blocker - size: (16.5×16.5) cm - (Ch. 5)
$BL(2)$	Rectangular sheet blocker - size: (36×28.2) cm - (Ch. 5)
$BL(3)$	Large square sheet blocker - size: (33×33) cm - (Ch. 5)
$BL(4), BL(5)$	Plastic and Metallic cylinder blocker: $(r_{BL}=5.7, h=141)$ cm - (Ch. 5)
C	Channel capacity
$C(v)$	The real part of the complex Fresnel-integral
c	The velocity of propagation, i.e. light speed $\cong 3 \times 10^8$ m/s
D	Antenna dimension
D_1, D_2	Projected distance from TX BS & RX MT nodes to BL edges
D_T, D_R	Transmitter and receiver antennas' directivity respectively
D_f	Foliage depth
d	The direct distance between TX BS and RX MT nodes
d_1, d_2	Distances from TX RX nodes to the intersection point of LOS with BL
d_s	The separation distance between the antenna elements
Δ	The difference between the directed path and the diffracted path
E_D	The electric field of a diffracted path
E_{LOS}	The electric field of the LOS path
ε	Blockage density which equals to $\frac{N_{BL}}{A_T}$
$F(P_{BL})$	An arbitrary blocker attenuation function
$F(v)$	The Fresnel-integral
$F_{h1 h2}, F_{w1 w2}$	Diffraction values associated with the four blocker's edges
f_c	Carrier frequency
\mathcal{G}	Gradient of the average number of blockers, i.e. N'
G_x	Normalised gains of directional antennas, $x = D1_{w1 w2}, D2_{w1 w2}$

G_T, G_R	Antenna gain of transmitter and receiver respectively
$\gamma_{\text{Rain}}, \gamma_{\text{Foliage}}$	Rain attenuation and foliage attenuation respectively
\mathbf{H}	MIMO channel matrix
h	Height of the KED blockage screen
h_{BL}	Height of blocker
h_T, h_R	Height of TX BS and RX MT respectively
κ	The angular wavenumber
L	Total length of the receiver track
λ	Wavelength
λ_i^2	The i th eigenvalue of $\mathbf{H}\mathbf{H}^H$
l_B	The number of sample points that are shadowed by one blocker
l_{NB}	The number of non-blocked samples before each blocker
l_1, l_2	The dimensions of the total area A_T
M	Monte Carlo runs
N	Total number of RX MT sample points
N_T, N_R	Number of elements of TX RX antenna arrays respectively
N_{BL}	Total number of blockers in the area
N_{cl}	Total number of cluster
N'	Average number of blockers ($N'_G \rightarrow$ Geometric, $N'_S \rightarrow$ Sum of MC)
N_o	Noise power
N_P	Total number of paths
$\mathbf{n}_g \in \mathbb{C}^{N_R \times 1}$	The additive white Gaussian noise vector
n, n_i	Noise element
n_{jk}	The number of times of making the change from state j to state k
\bar{P}	Power constraint in Watt
P_{BL}	Attenuation loss power due to blockage
P_d	Antenna power density
P_L	Free-space path loss
P_i^*	Power of the i th transmitted vector
P_{jk}	Transition probability from state j to state k
P_R	Received power
P'_R	Received power including the attenuation function, i.e. $P_R - F(P_{BL})$

$P'_{R Best}$	Received power of the best path in the presence of blockers
P_T	Transmitted power
Φ	The electrical length
ϕ	The elevation angle of the LOS path
$\phi_{T R}^{j,i}$	Elevation angles of departure and arrival of path i of cluster j
ρ_i	The received power of path i
$ R $	Rayleigh fading amplitude
R_n	Rain rate
r	The 2D TX-RX distance in the xy-plane
r_{BL}	Radius of one blocker
r_n	Radius of the 3D elliptical Fresnel zone
\mathcal{S}	State space of a random process
$S(v)$	The imaginary part of the complex Fresnel-integral
S_i	State i at Markov chain model
$S_h(i)$	Shadow length of blocker i
\overline{Sh}	Average shadow length
Σ_H	Rectangular matrix of singular values in channel's SVD
σ_n^2	Gaussian noise variance
\mathbf{T}	Transition probability matrix of Markov chain model
t_i	Sample time at index i
$\theta_{T R}^{j,i}$	Azimuth angles of departure and arrival of path i of cluster j
θ_i	The angle width of the shadow created by a blocker i .
\mathbf{U}_H	Left singular matrix of channel's SVD
\mathbf{V}_H	Right singular matrix of channel's SVD
\mathbf{v}_{BL}	Vector of number of blockers
v	Fresnel-Kirchoff parameter
W	Channel bandwidth
W_{HPBW}	Length of intersection line between antenna beam and blocker across from of the half-power beamwidth (HPBW) angle
w	Width of the KED blockage screen, i.e. blocker width
X_{infl}	Distance between the two edges of the influence-ring (Ch. 4)
\mathcal{X}_n	Set of random variables

\mathbf{x}	Transmitted signal vector
x, x_i	Transmitted signal element
\mathbf{y}	Received signal vector
y, y_i	Received signal element

Chapter 1

Introduction

This chapter provides a brief background of the high demand that will be placed on future communication systems, as well as shedding light on the applicability of mmWave frequency bands for these communication systems. It outlines the motivation for the thesis and highlights the main contributions of the work. It then provides an overview of the thesis structure and content.

1.1 Brief Background

The exponential growth in communication and data sharing will soon exceed the capacity limit of the existing cellular communication network [1]. Several factors are leading to the predicted vast increase in data traffic, including: the continually growing number of users and the fact that cellular phones are no longer limited to calling and texting. The average demand of each user has sharply increased due to the advanced technology and entertainment applications of smart mobile devices, which allow users to enjoy high definition video streams and data sharing through social media on their phones. About 92 % of internet users go online via their mobile devices [15]. According to Ericsson [16], the average monthly data use per smartphone is expected to jump from the 2019 figure of 7.2 GB to 24 GB in 2025. Moreover, moving towards smart homes and smart cities, by applying the concepts of internet of things (IoT) and enabling many devices to be connected, will add a further load to the network. With the above high demands, the fifth generation (5G) is required to provide large data rate with low latency. As shown in Figure 1.1, Nokia Networks [1] predicts that the user demand in the United States will exceed the capacity limit of the long-term evolution (LTE) network by around 2022-2023, where the suggested approach is accelerating the work of implementing 5G. The very wide bandwidth available at mmWave bands,

i.e. 30-300 GHz, makes it a promising approach for 5G systems. However, sensitivity to blockage is one of the main challenges that face the applicability of mmWave band systems. This challenging aspect needs further investigation work to understand and model the behaviour of the blockage effects on the performance of the mmWave communication systems. Addressing this issue leads us to the motivation of this thesis.

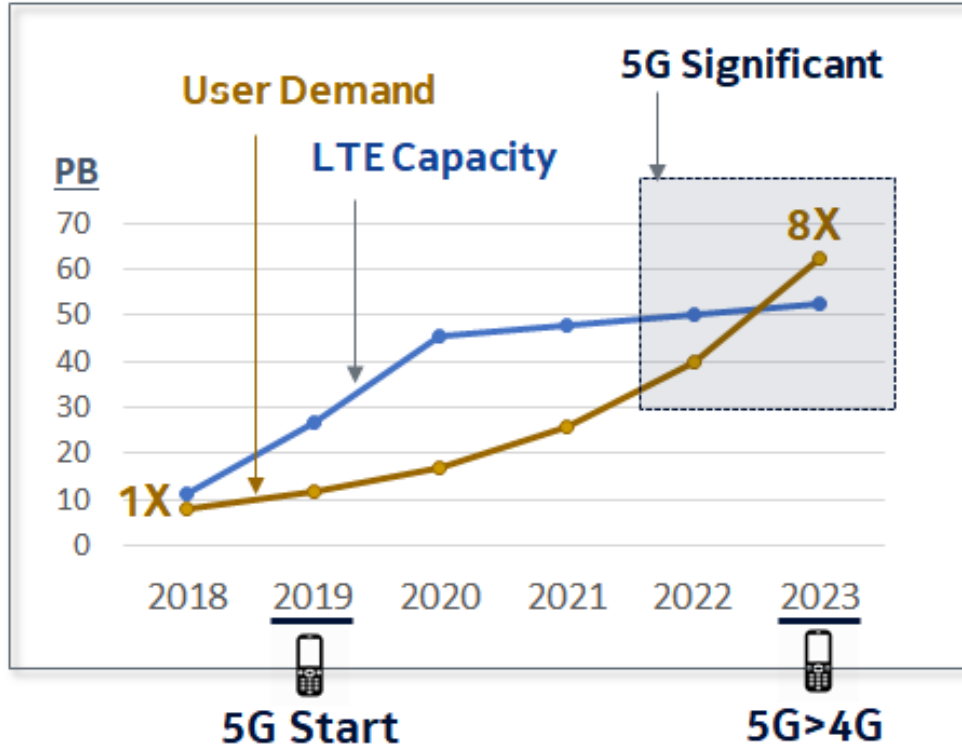


Figure 1.1: User-demands in the United States versus the LTE capacity limits. This figure is adopted from [1]. PB stands for petabyte.

However, the contiguous bandwidth of mmWave band, where it is possible to utilise several 100 MHz spectrum blocks, makes mmWave band attractive for many other technologies. The applicability of mmWave band is not limited to 5G, but it goes further beyond that. There are several other applications and technologies, some of which have already started to use of mmWave band. Some of these applications are short-range mmWave RaDAR that is used for weapon systems, point-to-point communications, inter-satellite links, disaster relief, radar, backhaul connections, etc.

1.2 Thesis Motivation and Contributions

There is a lack of understanding about the behaviour of the blockage impact on the mmWave signal strength and channel attenuation, in particular in relation to the dynamic case, where motion causes a sudden change in the channel attenuation. However, this knowledge is essential for designing a reliable mmWave communication system. Exploring this issue provides the motivation for this thesis.

The main contributions of the thesis are listed below:

1. Providing a simple Markov chain model that efficiently captures the dynamic channel attenuation with very low complexity. It assumes that each of the blockers surrounding a moving transceiver induces a fixed attenuation. The results of the simple proposed model show a good fit with the geometric model results, where the latter is a more complex model. For non-stationary scenarios, we provide a solution to make the proposed Markov model applicable by having several Markov chains in sequence, where switching from one to another is based on the current blockage density.
2. Capturing the blockage attenuation of complex scenarios requires a more advanced model. The second proposed model is the sum of Markov chains model, which can even adapt to a changing numbers of blockers with time. The model entails several advantages, such as integrating any blockage attenuation profile, including the 3GPP blockage model and all other measurements.
3. There is a lack of understanding in the existing literature about the attenuation resulting from objects that are smaller than human bodies. This thesis is one of the first studies to carry out new intensive measurement campaigns for five distinct types of blocker. It also examines the applicability of four existing simulation blockage models to predict the attenuation from these small blockers. We also show how measured blockage attenuations can be incorporated in simulation studies of mmWave wireless coverage.

1.3 Thesis Outlines

The remainder of the thesis is structured in the following way:

Chapter 2

The background chapter introduces the mmWave communication system and briefly discusses the relevant topics that readers need to be aware of to understand the main contributions of the thesis. It begins by introducing the mmWave band spectrum, defining the major advantages and the corresponding challenges, as well as highlighting the main prospective applications. The mmWave propagation mechanisms and main propagation losses are presented. This chapter also provides an overview of the relevant mmWave technologies, such as MIMO, beamforming and beam switching. The last section presents a general overview of the mmWave channel models and outlines the existing standards.

Chapter 3

This chapter provides an introduction to Markov chain approaches in general, then it introduces the proposed efficient Markov model and compares it with a geometric model. This chapter is partly based on [17], which proposes an efficient Markov chain model for modelling the dynamics of human and car blockages and the resulting attenuation in an outdoor scenario. It shows how the proposed model works for different stationary and non-stationary scenarios.

Chapter 4

The core of Chapter 4 is based on [14], which introduces a novel adaptive sum of Markov chains model that successfully and efficiently captures the dynamics of the blockage surrounding a moving transceiver in an outdoor scenario. It notes the advantages of the proposed model over the existing blockage models, including the Markov chain approach in Chapter 3. The chapter presents the major benefit of the model, which is the ability to integrate any attenuation profile.

Chapter 5

This chapter is based on two papers [18, 19]; it provides measurement campaigns for the attenuation caused by different types of relatively small blockages that have road-sign shapes. The chapter investigates the suitability of four existing knife-edge diffraction blockage in the literature for these small-sized blockages. An overall mmWave system evaluation in the presence of blockers for an outdoor scenario is also presented.

Chapter 6

The final chapter concludes and summarises the main contributions of the thesis, as well as discussing possible future research directions.

Chapter 2

Background

This chapter seeks to briefly cover all the related topics and concepts. It introduces the mmWave band, highlights the main advantages and related challenges. It also discusses the propagation mechanisms, the mmWave channel model and channel capacity. It explains the blockage issue and why it is necessary to capture the dynamic channel attenuation resulting from blockages.

2.1 Millimetre-wave Spectrum Overview

The millimetre-wave (mmWave) band is the name given to the extremely high frequency electromagnetic spectrum that ranges from roughly 30 to 300 GHz. Its name is drawn from the small wavelength, which is about 10 to 1 mm. The mmWave term has recently been used by industry referring more specifically to the range from 10 to 100 GHz [20]. However, the idea of utilising the mmWave band is not new; several systems are already operating in it; such as RaDAR, military communications and backhaul. One of the main advantages of the mmWave band is the vast available spectrum. For instance, at the unlicensed 57-66 GHz band, the available spectrum is 10 to 100 times the spectrum of the microwave band, which is below 6 GHz [20]. What draws the attention is that the bandwidth of all the existing modern wireless communication systems, including cellular, satellite, WiFi, AM/FM radio and TV, can be easily fitted within the unlicensed radio spectrum of around 60 GHz [20]. This illustrates the vast available bandwidth at the mmWave band, which is contiguous bandwidth compared with sub 6 GHz. This section provides a very brief overview of the main characteristics of the mmWave band, the advantages, challenges and some applications.

2.1.1 Main Advantages of mmWave

In comparison to the existing wireless systems, the mmWave band has some unique metrics that make it attractive for many applications in near future communication technologies. Some of these unique advantages are the 270 GHz of available spectrum and the small antenna elements that can be packed into a smaller space than for microwave frequency systems. Also, having large antenna arrays leads to very narrow beams, which is very useful for many applications [21]. The following are the main advantages of mmWave bands over the current communication systems [8]: vast bandwidth, large system capacity, low-latency, unlicensed bands, enhanced throughput, secure, very close frequency reuse, and directional communications. Among this list, the most attractive advantage of the mmWave band is the contiguous bandwidth.

2.1.2 Challenges of mmWave

As with any other new technology, some key challenges are faced in implementing the mmWave band. In this section, we highlight some of the main issues [22]:

1. *The high path loss and the atmospheric absorption* are significant in the mmWave band. These issues are presented in detail in Section 2.3.
2. *The susceptibility to blockage effects* is one of the main issues that mmWave communications face and this sets a limit to the transmitting distance. In the last decade, intensive work and measurement campaigns have been carried out by researchers to investigate a variety of blocker types at different mmWave frequency bands. The attenuation due to blockage can vary from 10 up to 40 dB depending on several factors, such as blockage material, location and size. For instance, the human body attenuates the mmWave signal in the range from 20 to 25 dB [9]. This issue is investigated in detail in Chapters 3 to 5 of this thesis.
3. *User and blockage mobility* is a crucial issue in the mmWave band since the small coherence time of mmWave leads to a high Doppler spread [23]. In the presence of blockers, movement causes a rapid and sudden change to the channel. This leads to high fluctuation in the received power, which will affect the

overall quality of service (QoS) of the mmWave band. The behaviour of dynamic attenuation requires further investigation. This is studied in Chapters 3 to 5 of this thesis.

2.1.3 Some Possible Approaches to Overcoming the mmWave Challenges

Several approaches have been suggested by researchers to address some of the above issues [22]: the high gain obtained by implementing massive MIMO would overcome the high power loss [24, 25]; directional beam-forming is another key strategy [26]; having an ultra-dense network of small cells (femtocell or pico cell size) is a suitable design strategy for the future mmWave cellular network [22]. Beam steering can also help to minimise rapid channel change [27].

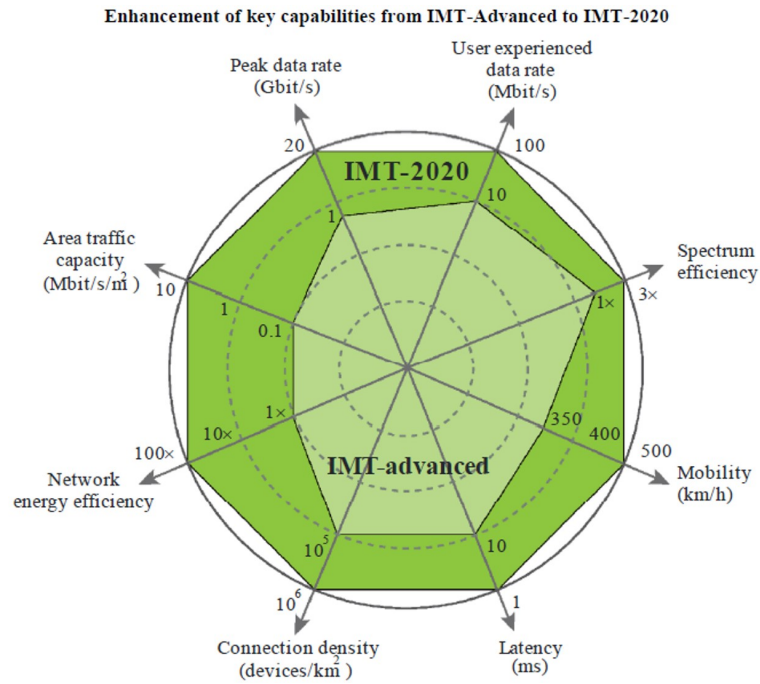


Figure 2.1: The eight key factors that are targeted for the future 5G system. This figure is adopted from [2]. IMT-2020 represents the 5G systems, which is named by ITU-R, and it stands for International Mobile Telecommunications (IMT) for 2020 and beyond, while IMT-Advanced represents 4G systems and it stands for International Mobile Telecommunications-Advanced.

2.1.4 5G Requirements versus mmWave Advantages

The fifth-generation (5G) of the cellular network will not be limited to cellular communication only. There is a high demand for the provision of connectivity to a large variety of applications where more devices are getting connected, i.e. the internet of things (IoT) concept [28]. Due to this high demand, 5G needs to provide $(100-1000\times)$ the capacity of the 4G network [29, 30]. The mmWave spectrum has ample capacity that could meet all these potential applications. The International Telecommunication Union (ITU) has defined eight key requirement terms for the 5G network, which are as follows: peak data rate, user experienced data rate, spectrum efficiency, mobility, latency, connection density, energy efficiency and area traffic capacity [2]. These requirements are illustrated in Fig. 2.1 and compared with the fourth-generation (4G) system. For instance, the latency is expected to reduce from 10 ms in the current 4G network to only 1 ms latency in the 5G network. The mmWave has beneficial features that can meet the 5G requirements. As stated in [31], a mmWave system incorporating massive multiple-input multiple-output (MIMO) and small cells is the key factor for the future 5G network; these are called the “big three” 5G technologies [32]. As a step towards a future commercial 5G mmWave system, mmWave applications for cellular communication have also been standardised by the 3GPP NR standards body [33].

2.1.5 Applications of mmWave

The attractive features of the mmWave system make it valuable for many applications. The following list shows some of numerous examples of how mmWave communication could be very useful [21]:

1. *mmWave fixed–wireless access (FWA)*: where a wireless link is used to connect two fixed locations. This is likely to be one of the first applications for mmWave. Verizon company for example is rolling this out in the USA [34].
2. *Future 5G cellular network*: which is discussed in Section 2.1.4.
3. *Wearable devices*: such as smartwatches, wireless headsets, fitness trackers and augmented reality glasses, require low latency and wide bandwidth [21]. Thus,

mmWave may have the potential to serve these applications [35, 36].

4. *Millimetre-wave in virtual reality (VR)*: the recent improvement in virtual reality (VR) technology has required mmWave band to connect VR headsets to VR servers [37].
5. *Communications for autonomous vehicles*: a further major step in autonomous vehicle technology is to make autonomous vehicles communicate with each other to exchange information, i.e. vehicle-to-vehicle (V2V), and with any other object in the surrounding environment, i.e. vehicle-to-infrastructure (V2I). These two systems can be combined to form vehicle-to-everything (V2X) networks [38]. In this particular application, low latency communication is crucial for safety, so mmWave is a promising technology [39]. Car accidents have become a major cause of death and this percentage is increasing dramatically as the number of cars on roads increases every year. According to the World Health Organization [40], car collisions kill around 1.25 million people around the world every year. It is predicted that by enabling autonomous vehicles, car crashes will decrease, but this may still not be sufficient since relying entirely on sensor systems such as Light Detection and Ranging (LiDAR) and Radio Detection and Ranging (RaDAR) may not provide full awareness of what is happening in the surrounding environment [41]. For instance, relying on LiDAR alone is inadequate due to some failure points, such as: 1- it cannot see through obstacles, fog and blind spots; 2- the gestures of a police officer may not be identified by LiDAR.

However, through the thesis, we apply our proposed blockage models for the V2I system as a study case.

2.2 Propagation

When radio waves propagate from a transmitting point to a receiving point as a form of electromagnetic wave, they may experience different phenomena, such as diffraction, reflection, absorption and scattering [42]. This section provides a brief background to

the main types of propagation that are considered in this thesis.

2.2.1 Free Space Propagation

Several propagation mechanisms lead the transmitting signal to travel and arrive at the receiving point. When the radio wave propagates in free space rather than being guided by a medium, this is called free space propagation, where the signal travels through the direct line between the transmitting and the receiving antennas far from any obstacle. When the source is an isotropic antenna, it propagates and distributes the signal uniformly in a spherical fashion. The transmit power of the isotropic antenna is divided by the total area of the surface of the sphere [43]. This is called the power density (i.e. power per unit area). At a distance d from the source, the power density is as follows:

$$P_d = \frac{P_T}{4\pi d^2} \quad (2.1)$$

By assuming that the transmitter is transmitting with gain G_T towards a receiver that has an effective area A_{eff} (which is known as the aperture), and a receiver gain G_R , we obtain the following equation [44]:

$$P_R = P_d A_{eff} = \frac{P_T G_T}{4\pi d^2} \left(\frac{\lambda^2 G_R}{4\pi} \right) \implies \frac{P_R}{P_T} = G_T G_R \left(\frac{\lambda}{4\pi d} \right)^2 \quad (2.2)$$

The last form of (2.2) is known as the Friis equation [45].

2.2.2 Reflection and Scattering

In a crowded area, it is more likely that there will not be a clear LOS path. However, due to the multipath that result from different propagation mechanisms, the signal can still travel to and reach the receiver. Reflection off a surface that is large in comparison to the wavelength is one of the main propagation mechanisms in the mmWave band. The smoothness level of the reflected surface, relative to the wavelength of the propagated signals, determines what type of reflection or scattering can occur [46]. These types are as follows: 1- specular reflection for a smooth surface; 2- diffused scattering

when the surface is rough.

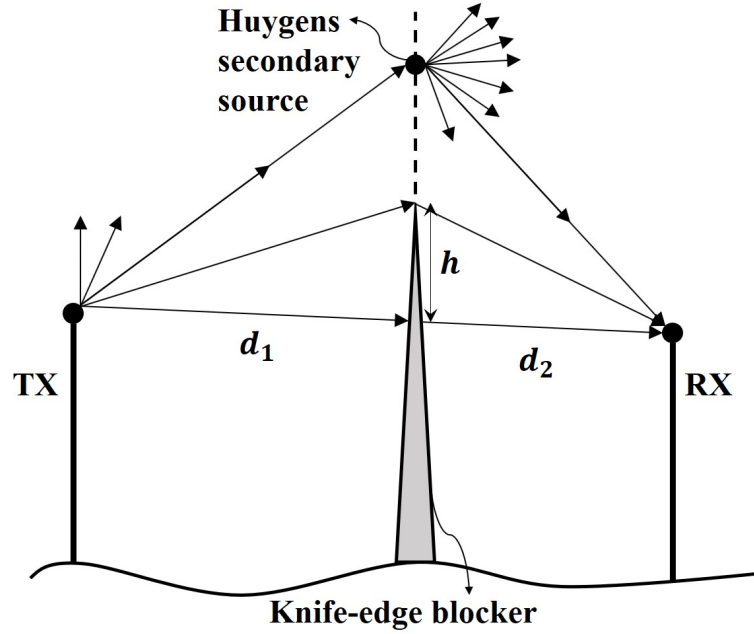


Figure 2.2: Diffraction and Huygens secondary source [3,4].

2.2.3 Huygens' Principle

As stated in [3], the reflection of objects is a type of propagation, where the object is assumed to be large compared to the wavelength, so that makes the wave reflect. However, when the wavefront confronts an object that is not large, Huygens' principle is applied. This concept can be obtained from Maxwell's equation, and it states that every point on the wavefront is a source point that could produce secondary spherical wavelets, as shown in Fig. 2.2. The wavelets from all these points will propagate in the shadow region behind the blocker. The electric field in the shadow region is the resultant field from the interference between these secondary wavelets.

2.2.4 Fresnel Zone

In wireless communication systems, the imaginary three-dimensional (3D) elliptical region between the transmitting and the receiving antennas, as shown in Fig. 2.3, is known as the Fresnel zone [47,48]. It is constructed of several layers, where the first is

the inner one. The size of the 3D elliptical is determined by the TX-RX distance and the carrier frequency, where the radius of the 3D elliptical area at point P is defined as:

$$r_n = \sqrt{\frac{n\lambda d_1 d_2}{(d_1 + d_2)}} \quad (2.3)$$

where n is an integer number representing the index of the zone.

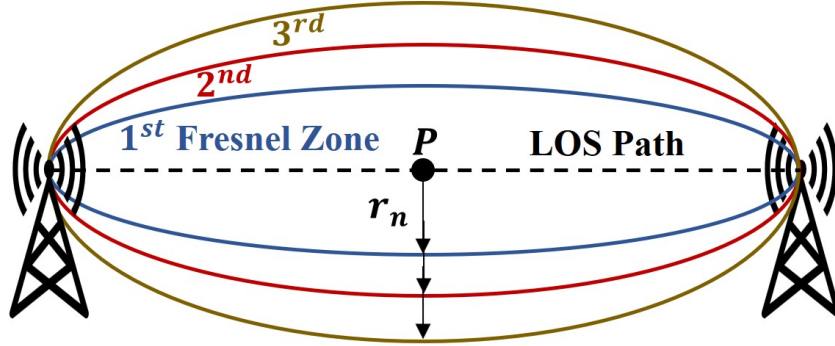


Figure 2.3: Fresnel zones.

2.2.5 Diffraction Phenomena

Diffraction is one of the main propagation techniques that allow the radio wave to travel around an obstacle using Huygens' secondary wavelets as a secondary source of propagation. Since the secondary source produces signals in a spherical shape, which cause the appearance of bending waves behind the blocker in the shadow region, this is called diffraction [4].

2.2.6 Knife-edge Diffraction

The simplest scenario of diffraction propagation is knife-edge diffraction (KED), where the obstacle or blocker between the transmitter and the receiver is assumed to be a very thin screen with infinite width and very sharp edge. The blocker blocks all the rays, so none can penetrate. Huygens' secondary source points are assumed to be along the vertical imaginary line above the blocker [4], as shown in Fig. 2.2.

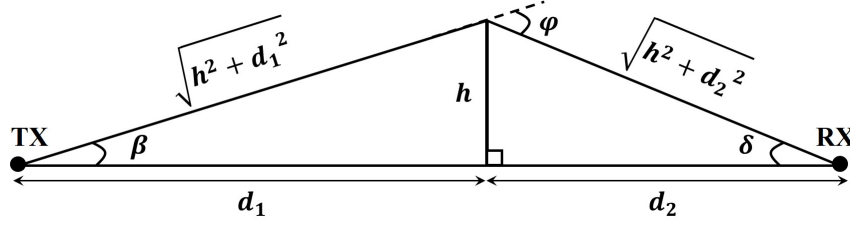


Figure 2.4: Simplified KED model [3,4].

The main scope of this thesis is investigating the attenuation caused by a blocker, and a large part of the thesis is based on the KED theory. Thus, it is crucial to explain the derivation of the KED blocker attenuation, which is obtained from the superposition electric field behind the KED screen. This is adopted from [4].

From the simplified geometry in Fig. 2.4, the difference between the directed path and the diffracted path Δ is:

$$\Delta = \sqrt{d_1^2 + h^2} + \sqrt{d_2^2 + h^2} - (d_1 + d_2) \implies d_1 \sqrt{1 + \frac{h^2}{d_1^2}} + d_2 \sqrt{1 + \frac{h^2}{d_2^2}} - d_1 - d_2 \quad (2.4)$$

$$\Delta \approx d_1 \left(1 + \frac{h^2}{2d_1^2} \right) + d_2 \left(1 + \frac{h^2}{2d_2^2} \right) - d_1 - d_2 \implies \frac{h^2}{2} \left(\frac{1}{d_1} + \frac{1}{d_2} \right) \quad (2.5)$$

$$\Delta = \frac{h^2}{2} \left(\frac{d_1 + d_2}{d_1 d_2} \right) \quad (2.6)$$

Based on the assumption that $d_1, d_2 \gg h$, the angles are as follows:

$$\beta = \tan^{-1} \frac{h}{d_1} \approx \frac{h}{d_1} \quad (2.7)$$

$$\delta = \tan^{-1} \frac{h}{d_2} \approx \frac{h}{d_2} \quad (2.8)$$

From angle geometry, the angle φ is:

$$\varphi = \beta + \delta \approx \frac{h(d_1 + d_2)}{d_1 d_2} \quad (2.9)$$

The electrical length is obtained by multiplying the angular wavenumber, i.e. $\kappa = \frac{2\pi}{\lambda}$,

by Δ as follows:

$$\Phi = \kappa\Delta = \frac{\pi}{2}h^2\frac{2}{\lambda}\frac{(d_1 + d_2)}{d_1d_2} \quad (2.10)$$

By introducing the Fresnel-Kirchoff parameter v as follows:

$$v = h\sqrt{\frac{2(d_1 + d_2)}{\lambda d_1 d_2}} = \varphi\sqrt{\frac{2d_1 d_2}{\lambda(d_1 + d_2)}} \quad (2.11)$$

the equation could be written as follows:

$$\Phi = \frac{\pi}{2}v^2 \quad (2.12)$$

The later form of v is only used when the distances and angles are known and the height of the antennas are different.

At the receiver point, the normalised electric field is expressed as:

$$\frac{E_D}{E_{LOS}} = \exp(-j\beta\Delta) = \exp\left(-j\frac{\pi}{2}v^2\right) \quad (2.13)$$

where E_D is the electric field of a diffracted path while E_{LOS} is the electric field of the LOS path. The magnitude difference between these two electric fields is assumed to be zero.

The electric strength at the receiver behind the KED screen is obtained by a Fresnel-integral that sums up all Huygens' secondary sources from v to ∞ as follows [44]:

$$\frac{E_D}{E_{LOS}} = F(v) = \frac{1+j}{2} \int_v^\infty \exp\left(-j\frac{\pi}{2}t^2\right) dt \quad (2.14)$$

$$F(v) = \frac{1+j}{2} \left[\int_v^\infty \cos\left(\frac{\pi}{2}t^2\right) dt - j \int_v^\infty \sin\left(\frac{\pi}{2}t^2\right) dt \right] \quad (2.15)$$

The complex Fresnel-integral is usually written as:

$$C(v) - jS(v) = \int_0^v \exp\left(-j\frac{\pi}{2}t^2\right) dt \quad (2.16)$$

$$C(v) - jS(v) = \int_0^v \cos\left(\frac{\pi}{2}t^2\right) dt - j \int_0^v \sin\left(\frac{\pi}{2}t^2\right) dt \quad (2.17)$$

To be able to integrate this function, we redefine it as follows:

$$\int_v^\infty \cos\left(\frac{\pi}{2}t^2\right) dt = \int_0^\infty \cos\left(\frac{\pi}{2}t^2\right) dt - \int_0^v \cos\left(\frac{\pi}{2}t^2\right) dt \quad (2.18)$$

The values of the Fresnel-integral at ∞ are:

$$C(\infty) = S(\infty) = \frac{1}{2} \quad (2.19)$$

$$F(v) = \frac{1+j}{2} \left\{ \left[\frac{1}{2} - C(v) \right] - j \left[\frac{1}{2} - S(v) \right] \right\} \quad (2.20)$$

However, instead of computing the complex integration to get the loss, Lee [6] provides a well-known approximation as follows:

$$|F(v)| \text{ (dB)} = \begin{cases} 0 & v \leq -1 \\ 20 \log(0.5 - 0.62v) & -1 \leq v \leq 0 \\ 20 \log(0.5 \exp(-0.95v)) & 0 \leq v \leq 1 \\ 20 \log\left(0.4 - \sqrt{0.1184 - (0.38 - 0.1v)^2}\right) & 1 \leq v \leq 2.4 \\ 20 \log\left(\frac{0.225}{v}\right) & v > 2.4 \end{cases} \quad (2.21)$$

Another approximation is provided by the 3GPP standards body [5]. This will be discussed in detail in Chapters 4 and 5. The approximation is expressed as follows:

$$P_{BL} \text{ (dB)} = -20 \log_{10}(0.5 - F_w) \quad (2.22)$$

where F_w equals to:

$$F_w = \frac{\text{atan}\left(\pm \frac{\pi}{2} \sqrt{\frac{\pi}{\lambda}} (D_1 + D_2 - d)\right)}{\pi} \quad (2.23)$$

where λ is the wavelength, D_1 and D_2 are the projected distance from the TX and RX

nodes to the screen, and d is the projected distance between the TX and RX nodes. The exact calculation of the path loss, and both approximations, i.e. Lee's and 3GPP's, are plotted in Fig. 2.5. The curves show that they match well.

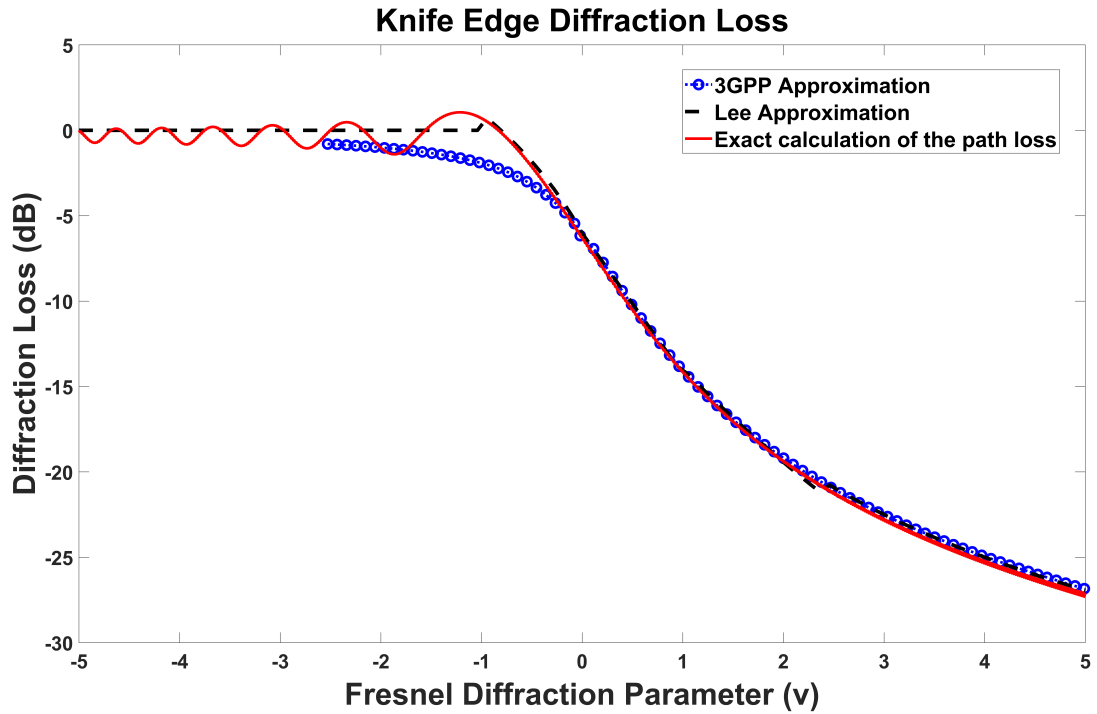


Figure 2.5: Knife-edge diffraction loss: 3GPP's approximation [5], Lee's approximation [6], and the exact calculation of the path loss [7].

2.3 Propagation Loss Factors

Besides the high path loss, having a short wavelength makes the mmWave band more vulnerable to some additional losses and attenuations, which are not apparent for radio signals in the microwave bands [10]. In this section, some main attenuation factors are briefly discussed.

2.3.1 Free Space Path loss

When the signal propagates in free space, it experiences some loss that is influenced by the frequency and travelling distance. The loss increases as either the travelling distance or the frequency gets higher, which means for mmWave frequencies, the loss is very high. The free space path loss (FSPL) is the inverse of the last form of (2.2), as follows [49]:

$$P_L = \frac{P_T}{P_R} = \left(\frac{4\pi d}{\lambda} \right)^2 = \left(\frac{4\pi f_c d}{c} \right)^2 \quad (2.24)$$

where $G_T = G_R = 1$ for an isotropic antenna, and c is the velocity of propagation, i.e. light speed. For a distance in km and a frequency in GHz, the FSPL can be expressed in dB as follows [50]:

$$P_L(\text{dB}) = 92.44 + 20 \log f_c[\text{GHz}] + 20 \log d_{[\text{km}]} \quad (2.25)$$

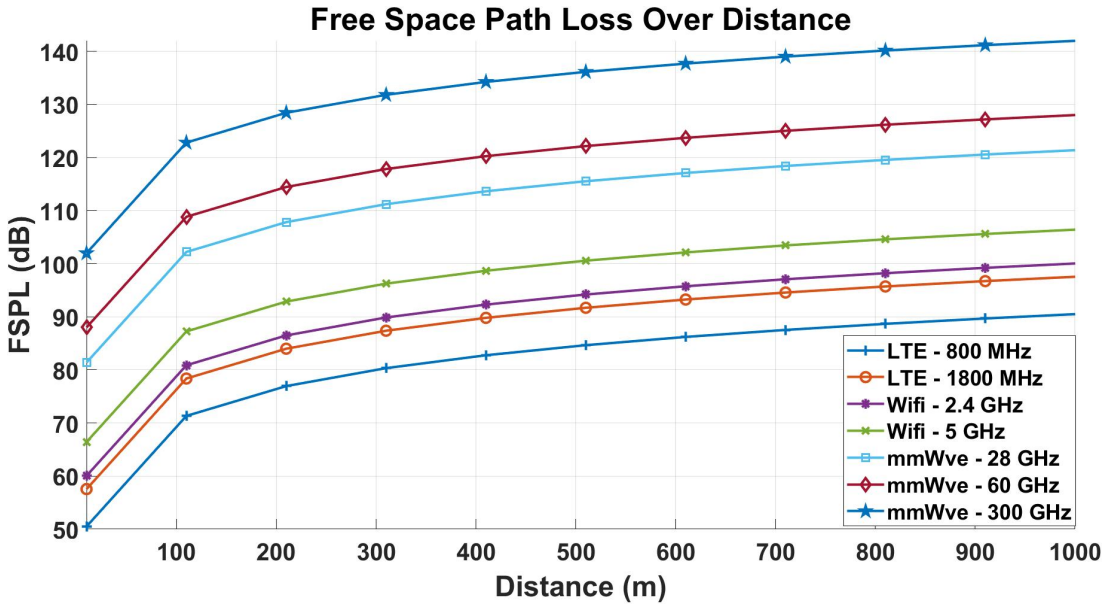


Figure 2.6: The free space path loss over distance for several LTE bands, WiFi bands, and multiple mmWave bands.

The high path loss is a major issue in mmWave band due to the high frequency; Fig. 2.6 shows an FSPL comparison between several UK LTE bands 800 and 1800 MHz,

the 2.4 and 5 GHz WiFi bands [8], and several mmWave bands 28, 60 and 300 GHz. The mmWave bands certainly experience higher path loss, e.g. the difference between the FSPL at the LTE 800 MHz, and the 28 GHz band experiences around 30 dB extra loss at 28 GHz. Several solutions could overcome the high path loss of the mmWave. Two of these are as follows:

1. Having massive MIMO [31].
2. Another interesting simple technique, proposed by [22, 51], is to keep the antenna aperture constant at both terminals, which will minimise the free space path loss with the squared carrier frequency f_c^2 .

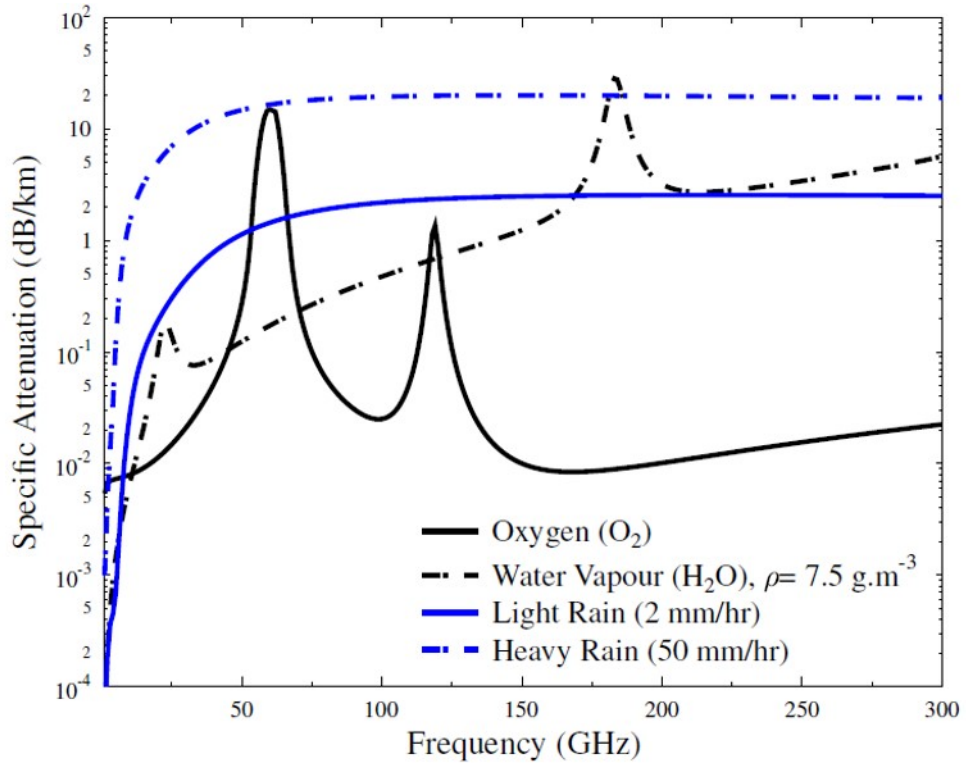


Figure 2.7: The atmospheric absorption of mmWave. The figure shows the curves of Oxygen (O_2), water vapour (H_2O), and rain at sea level versus the carrier frequency. The density of (H_2O) is in g/m^3 is presented by the symbol. This figure is adopted from [8], which is originally generated from [9, 10].

2.3.2 Atmospheric Attenuation

When a mmWave radio wave propagates through the atmosphere, an attenuation happens due to absorption by the atmosphere [8, 10]. The air-gas molecules absorb some energy from the propagated wave and they are vibrated [52]. This atmospheric absorption mainly happens via oxygen (O₂) and water vapour (H₂O) molecules. As shown in Fig. 2.7, the amount of gas absorption varies with the carrier frequency, where some bands are affected worse than others.

As shown in Fig. 2.7, the oxygen absorption reaches its peak around the 60 GHz band, which roughly equals 16 dB/km [53], and it experiences another lower peak around the 120 GHz band [54]. The absorption caused by water vapour molecules reaches its maximum around the 180 GHz band, which can reach up to several tens of dB [54, 55]. These high atmospheric absorption densities result in higher atmospheric attenuation values that limit the travel distance for the mmWave band. This has a significant impact on the propagation range; by switching from a 60 GHz band to around 80 GHz, the operation range extends from 400 m to 3 km [53, 56]. Between these absorption peaks, mmWave spectrum has some potential bandwidth windows that might be suitable for propagation with less atmospheric attenuation; these windows are around the 35, 94, 140 and 220 GHz bands [10, 21].

2.3.3 Rain Attenuation

Millimetre-wave propagation can be affected by rainfall [57]. The raindrop has a size of a few mm, which is analogous to the size of the mmWave wavelength (1-10) mm; this makes the mmWave band more likely to be affected by lower frequency bands [8]. The rainfall can severely affect the mmWave signal depending on how heavy or light it is [54]. Based on the rain rate (mm/h), the rain attenuation (dB/km) can be computed through a number of models in the literature; one of these is provided by the International Telecommunication Union (ITU) [58]. According to ITU, rain attenuation is expressed as follows [8, 58]:

$$\gamma_{\text{Rain}} (\text{dB/km}) = q R_n^u \quad (2.26)$$

where R_n is the rain rate, while u and q variables are functions of several factors, such as carrier frequency, altitude, the direction of polarisation, etc. For a heavy rain rate around 50 mm/km, the rain attenuation is about 10 dB/km [54]. Fig. 2.7 illustrates the rain attenuation versus the mmWave frequency band at two rain rate levels: light rain of 2 mm/hr and heavy rain of 50 mm/hr.

2.3.4 Foliage Attenuation

Foliage is another attenuation factor for mmWave radio waves that could be significant; this depends on how deep the foliage is [59]. When the depth is less than 400 m, the foliage attenuation is expressed empirically as [60, 61]:

$$\gamma_{\text{Foliage}} (\text{dB}) = 0.2 f_c^{0.3} D_f^{0.6} \quad (2.27)$$

where f_c is the carrier frequency in MHz and D_f is the foliage depth ≤ 400 m. For instance, for foliage with 10 m depth, the foliage attenuation at the 800 MHz, which is a UK LTE band, is 5.9 dB. On the other hand, the foliage attenuation is 17.1 dB at the 28 GHz band. This means there is roughly three times more attenuation at the mmWave band.

2.3.5 Material Penetration and Blockage Loss

2.3.5.1 Material Penetration Loss

Compared with sub-6 GHz frequencies, the penetration loss is much higher in the mmWave band due to its characteristics [62, 63]. The penetration loss varies depending on the material type and how thick it is. For instance, based on measurement campaigns reported in [62] at the 28 GHz band, the penetration loss created by the clear glass of different buildings was measured at between 3.6 and 3.9 dB, while the penetration loss caused by tinted glass was as high as 20-40 dB. The increased loss is due to the different material type since the external glass of buildings is usually integrated with metal for heating and visibility reasons [64]. Several studies in the

literature, such as [46, 62, 63, 65–67], have carried out intensive measurements at different mmWave frequency bands for several material types and thicknesses, such as a wall, brick, wooden door, steel door, etc.

2.3.5.2 Blockage Attenuation

The mmWave band shows high sensitivity to blockage attenuation, which is one of the main challenges. Any object crossing the LOS path between the transmitter and the receiver points will induce an attenuation that could severely affect the signal strength. Human blockage, as an example, causes attenuation of 20-25 dB [9]. The attenuation resulting from a lorry blockage could also be more than 30 dB [68]. This thesis focuses on the modelling and evaluation of the blockage effect. In Chapter 3 the effect of human and car blockages will be investigated. Human blockage is also analysed in more detail in Chapter 4. Relatively small blockages are investigated in Chapter 5.

2.4 mmWave Channel Models

2.4.1 AWGN Channel Capacity and Spectral Efficiency

The Shannon capacity theorem defines a limit for the maximum achievable data rate that can be transmitted, nearly error-free, i.e. with very small bit-error rate (BER) ≈ 0 , over a noisy communication channel [69]. Exceeding this limit leads to an error probability of 1/2, so that no data can be communicated. The memoryless band-limited continuous-time communication channel with zero mean additive white Gaussian noise is known as the additive white Gaussian noise (AWGN) channel, which can be expressed as follows [70]:

$$y[m] = x[m] + n[m] \quad (2.28)$$

where $y[m]$ and $x[m]$ respectively are the complex output, and the complex input at time m . The additive white noise $w[m]$ is independent and identically distributed and follows a Gaussian distribution with zero mean and variance of σ_n^2 , i.e. $\sim \mathcal{CN}(0, \sigma_n^2)$.

The channel capacity for this basic model is derived as follows:

$$C_{\text{AWGN}}(\bar{P}, W) = W \log_2 \left(1 + \frac{\bar{P}}{N_o W} \right) \quad (\text{bits/s}) \quad (2.29)$$

where \bar{P} is the power constraint in Watt, and the power spectral density of Gaussian noise is $N_o/2$. The maximum spectral efficiency (SE) of the AWGN channel can then be expressed as follows [70]:

$$\text{SE}_{\text{AWGN}} = \log_2 (1 + \text{SNR}) \quad (\text{bits/s/Hz}) \quad (2.30)$$

where SNR is the signal-to-noise ratio per complex degree of freedom, which is equal to $\text{SNR} = \bar{P}/N_o W$.

2.4.1.1 Power and Bandwidth Dependency

The main resources of the AWGN channel capacity are the received power \bar{P} and the bandwidth W [70]. For a fixed given SNR and varying the bandwidth from nearly zero to infinity, the AWGN channel capacity can be divided into different regimes:

1. **Bandwidth-limited regime:** a small bandwidth W yields a large SNR, i.e. $\text{SNR} = \frac{\bar{P}}{N_o W} \gg 1$; the channel capacity shows a logarithmic relationship with the received power, and it is approximately linearly related with bandwidth. Equation (2.29) is expressed as follows:

$$C_{\text{AWGN}}(\bar{P}, W) = W \log \left(\frac{\bar{P}}{N_o W} \right) \quad (\text{bits/s}) \quad (2.31)$$

2. **Power-limited regime:** when the bandwidth W is large, i.e. the $\text{SNR} = \frac{\bar{P}}{N_o W} \ll 1$, the channel capacity has a linear relationship with the received power, and it is insensitive to the bandwidth. Equation (2.29) is redefined as:

$$C_{\text{AWGN}}(\bar{P}, W) = W \log \left(1 + \frac{\bar{P}}{N_o W} \right) \approx W \left(\frac{\bar{P}}{N_o W} \right) \log_2 e = \frac{\bar{P}}{N_o} \log_2 e \quad (2.32)$$

where as $W \rightarrow \infty$, $C_\infty = \frac{\bar{P}}{N_o} \log_2 e$ (bits/s).

2.4.2 mmWave MIMO Overview

As mentioned in Section 2.1.4, 5G has quite high demand requirements, one of which is the system capacity, which needs to provide (100-1000 \times) the capacity of the 4G network [29, 30]. From information theory, the capacity can be increased in three possible ways [24, 29, 30]: 1- ultra-dense networks (UDNs), which can be achieved by reducing the cell size and increasing the overall cell density; 2- large quantities of new bandwidth, as in the case of the mmWave band; 3- high spectrum efficiency, which requires the implementation of a very large number of antennas, i.e. MIMO or massive MIMO [71, 72]. These three approaches reinforce each other; the short mmWave wavelength would enable engineers to pack a large number of antennas together to achieve MIMO, and due to the mmWave propagation characteristics, small cells are essential [30]. MIMO technology could significantly improve the overall performance of the communication system by providing the following gains: *array gain*, *spatial diversity gain*, *interference reduction gain* and *spatial multiplexing gain* [73, 74].

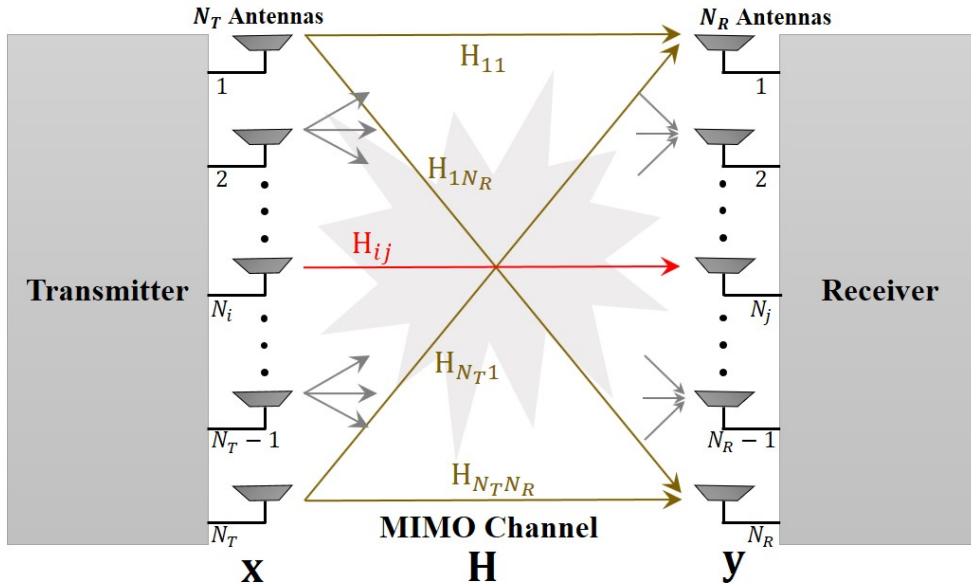


Figure 2.8: Simplified configuration of MIMO System.

Fig. 2.8 shows a simple diagram for the mmWave MIMO system, which is a multi-antenna system. The number of the transmitter's antennas is denoted by N_T and N_R for the number of the receiver's antennas. The MIMO channel matrix has $N_T \times N_R$ entries, i.e. $\mathbf{H} \in \mathbb{C}^{N_T \times N_R}$, where the entry H_{ij} represents the channel component from the transmit antenna i to the receiver antenna j , as shown in the figure. Each RX antenna receives a direct channel component, e.g. H_{11} , and all non-direct components such as H_{21} , H_{31} , etc. The MIMO channel matrix can be a narrowband or wideband channel. The received signal vector $\mathbf{y} \in \mathbb{C}^{N_R \times 1}$ is as follows:

$$\mathbf{y} = \mathbf{H}\mathbf{x} + \mathbf{n} \quad (2.33)$$

where the transmitted signal vector is denoted by $\mathbf{x} \in \mathbb{C}^{N_T \times 1}$. The additive white Gaussian noise vector $\mathbf{n} \in \mathbb{C}^{N_R \times 1}$, which is independent and identically distributed (I.I.D.) with complex Gaussian distribution, i.e. $\mathbf{n} \sim \mathcal{CN}(0, N_0 \mathbf{I}_{N_R})$.

2.4.3 Narrowband channel model

Following the work of [8, 75, 76], for the mmWave narrowband channel model, the Saleh Valenzuela model is extended [77, 78]. For N_{cl} scatters and N_P paths for each scatter, the narrowband channel matrix is expressed as follows:

$$\mathbf{H} = \frac{N_T N_R}{N_P} \sum_{j=1}^{N_{cl}} \sum_{i=1}^{N_P(j)} \alpha_{j,i} \mathbf{a}_R(\phi_R^{j,i}, \theta_R^{j,i}) \mathbf{a}_T(\phi_T^{j,i}, \theta_T^{j,i})^H \quad (2.34)$$

where j is the cluster index and i is the path index. The scalar $\alpha_{j,i}$ is the path complex gain, and $N_T N_R$ are the number of transmitter and receiver antennas respectively. The azimuth and the elevation angles of arrival (AoA) are $(\phi_R^{j,i}, \theta_R^{j,i})$ and angles of departure (AoD) $(\phi_T^{j,i}, \theta_T^{j,i})$. The steering transmitter and the receiver vectors are represented respectively by $\mathbf{a}_T(\phi_T^{j,i}, \theta_T^{j,i})$, $\mathbf{a}_R(\phi_R^{j,i}, \theta_R^{j,i})$.

The response vector depends on the array configuration and the sample space; for

uniform plane array (UPA), the steering vector is expressed as follows [76]:

$$\mathbf{a}(\phi, \theta) = \frac{1}{N} [1, e^{j2\frac{\pi}{\lambda}d_s(a \sin(\phi) \sin(\theta) + b \cos(\theta))}, \dots, e^{j2\frac{\pi}{\lambda}d_s((A-1) \sin(\phi) \sin(\theta) + (B-1) \cos(\theta))}] \quad (2.35)$$

where N is the total number of array elements, which is $N = AB$. The scalar a and b indicate the antenna element where $0 \leq a \leq A$ and $0 \leq b \leq B$. The scalar d_s is the separation distance between the antenna elements, and λ is the wavelength.

2.4.4 MIMO Channel Capacity

2.4.4.1 Channel State Information (CSI) is Known at the Transmitter (Waterfilling):

The MIMO channel matrix can be written in a singular value decomposition (SVD) form as follows [75]:

$$\mathbf{H} = \mathbf{U}_H \Sigma_H \mathbf{V}_H^H \quad (2.36)$$

where the unitary matrices are denoted by $\mathbf{U}_H \in \mathbb{C}^{N_R \times N_R}$ and $\mathbf{V}_H \in \mathbb{C}^{N_T \times N_T}$. The matrix $\Sigma_H \in \mathbb{R}^{N_R \times N_T}$ is a diagonal matrix whose elements are non-negative [74]. The diagonal entries of Σ_H are the singular values of the channel matrix \mathbf{H} in decreasing order, where $\lambda_1 \geq \lambda_2 \geq \dots \geq \lambda_{r_{min}}$. The rank of the channel matrix \mathbf{H} is r_{min} where $r_{min} = \min(N_T, N_R)$. The scalar λ_i^2 is the i th eigenvalue of $\mathbf{H}\mathbf{H}^H$ [79].

Then equation (2.36) can be expressed as follows [75]:

$$\mathbf{H} = \sum_{i=1}^{r_{min}} \lambda_i \mathbf{u}_i \mathbf{v}_i^H \quad (2.37)$$

Multiplying the transmit vector by the matrix \mathbf{V} and then multiplying the receive vector by the matrix \mathbf{U} turns the MIMO channel matrix \mathbf{H} into r_{min} independent orthogonal parallel channels [80]. Now the optimum method for power allocation is achieved by applying the waterfilling approach at the transmitter side, which is obtained as follows [80]:

$$P_i^* = \left(\mu - \frac{1}{\lambda_i^2} \right)^+, 1 \leq i \leq r_{min} \quad (2.38)$$

where P_i^* is the power of the i th transmitted vector. The waterfilling power allocation μ should satisfy the condition $\sum_{i=1}^{r_{min}} P_i^* = P_T$.

The MIMO channel spectral efficiency is then obtained by summing the sub-channels' spectral efficiency (SE) values as follows [74, 79]:

$$SE_{MIMO} = \sum_{i=1}^{r_{min}} \log_2 \left(1 + \frac{P_i^* \lambda_i^2}{\sigma_n^2} \right) \quad (2.39)$$

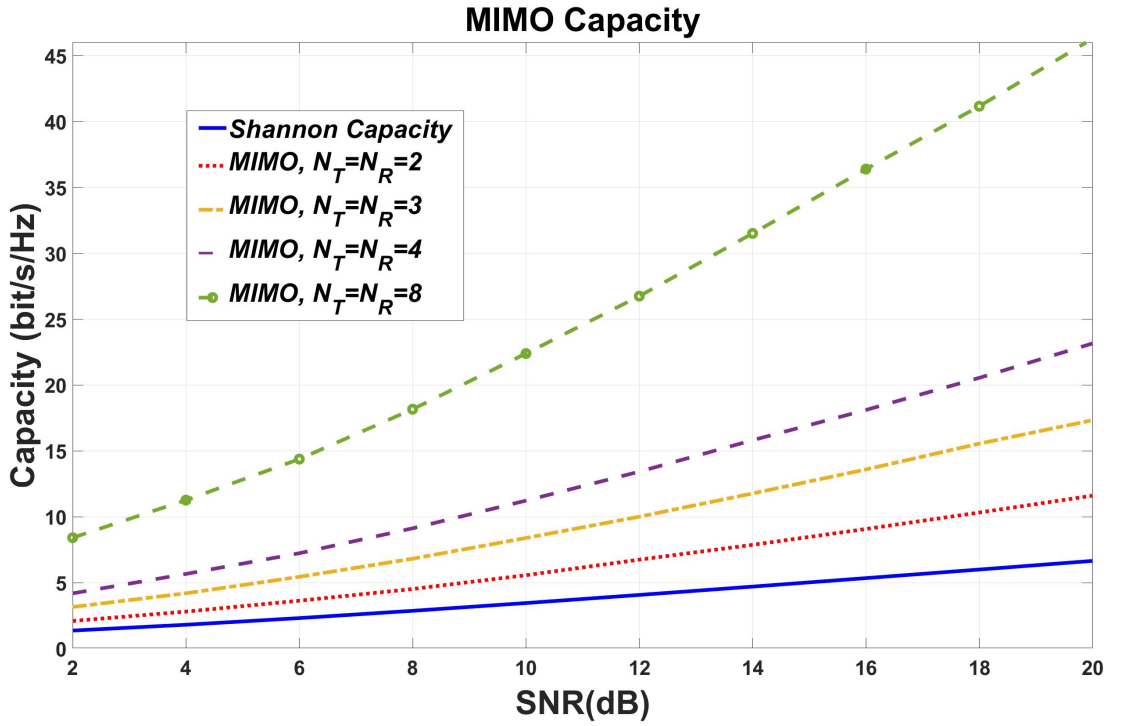


Figure 2.9: MIMO spectral efficiency, with respect to the SNR, with a different number of TX and RX antenna arrays compared with Shannon channel capacity [11]. These capacity results are for the i.i.d. Rayleigh fading channel.

The capacity results, of Fig. 2.9, are for the i.i.d. Rayleigh fading channel. As shown in the figure, at SNR = 20 dB, the 2×2 MIMO SE = 11.6 bits/s/Hs, which is around 5 bits/s/Hs more than the Shannon capacity. Also, 8×8 MIMO SE shows an improvement of 40 bits/s/Hs over the Shannon capacity at SNR = 20 dB, which is a significant enhancement that shows the advantages of having a MIMO system.

2.4.4.2 Channel State Information (CSI) is Unknown at the Transmitter:

If the channel state is unknown at the transmitter side, the power is equally divided among the sub-channels and then the spectral efficiency is expressed as follows [80]:

$$SE_{\text{MIMO}} = \log_2 \left(\det \left(\mathbf{I}_M + \frac{P_T}{\sigma_n^2 N} \mathbf{H} \mathbf{H}^H \right) \right) \quad (2.40)$$

where \mathbf{I}_M is the identity matrix.

2.4.5 Beamforming Overview

Beamforming (BF) is a signal processing technique that enables the communication system to steer the beam in the desired direction, leading to antenna gain. By applying the BF technique with multiple data streams between transmitter and user, the mmWave spectral efficiency is also enhanced further [81]. The 3D beamforming is a promising technique for the mmWave MIMO system [82]. The beamforming technique can be applied in several ways: analogue, digital, hybrid (i.e. combined analogue and digital) [83]. For analogue BF, at each terminal a digital baseband is connected to a single radio frequency (RF) chain with several phase shifters. Although this is an efficient technique regarding the hardware complexity and the power consumption [75], it is limited to a single user and a single transmitted stream. On the other hand, for the fully digital BF, each antenna element is connected to a separate RF chain; this would be impractical for mobile devices with a large number of antennas, i.e. massive MIMO, due to the high power consumption and introduced hardware complexity [76, 81, 84]. However, hybrid precoding is the most suitable technique, and it is the most likely to be applied for mmWave massive MIMO where a lower number of RF chains is required, which reduces the hardware complexity and the power consumption [84]. A hybrid MIMO system for mmWave communications is a popular topic, and there are many recent studies that attempt to reduce the complexity and enhance the overall energy and spectral efficiency; however this is beyond the scope of this thesis.

2.4.6 Beam Switching for Resolving Blocked Path

For a mmWave communication system, beamforming is essential, not only due to the extra gain it introduces, but also because it could be an effective solution to minimise the blockage effect issue, which is a serious problem in mmWave communications. When the line of sight (LOS) path is blocked, switching the main beam to the next available non-line of sight (NLOS) is an approach considered by IEEE 802.15.3c activities [85,86]. Reference [86] is one of the first papers that evaluates the beam-switching approach for 60 GHz. In the situation where the LOS is blocked, the authors introduce two mechanisms for undertaking the beam-switching technique: instant decision, and a decision based on learning the environment. The beam-switching technique, in the presence of blockers, is applied in Chapter 5 of this thesis, where a ray-tracing tool is used to establish all possible propagated paths for an outdoor environment.

2.4.7 Existing Standardisations and Projects for mmWave Channel Models

The mmWave propagation characteristics discussed in Sections 2.2 and 2.3 require intensive work for accurate channel modelling. Over the last two decades, several body standards and projects have launched comprehensive work on mmWave channel modelling. Reference [8] have undertaken an inclusive survey for the existing mmWave channel models: narrowband and wideband. Table 2.1 presents a timeline and the frequency band for the main channel models. Some of these standards and projects have also provided a simulation blockage model, such as the METIS project [12], 3GPP standard body [5], NYU WIRELESS group [87], and mmMAGIC project [88]. As part of this thesis work, these blockage models have been adopted and evaluated in part in Chapter 4, with more detail in Chapter 5.

Year	Standard/Project/Paper Name of the Channel Model	Frequency Band	Technology
2005 - 2007	IEEE 802.15.3c standardisation project - Task Group 3c (TG3c) [89]	60 GHz	Wireless Personal Area Network (WPAN)
2009 - 2010	IEEE 802.11ad - Task Group ad (TGad) [90]	60 GHz	Wireless Local Area Network (WLAN)
Since 2011	NYU WIRELESS 5G Channel Models (5GCM) [91–93]	28, 38, 72 GHz	5G
2012	METIS project [12]	up to 100 GHz	5G
2013	NYU WIRELESS's paper on mobile broadband (MMB) [27]	28, 38 GHz	MMB
2014	MiWEBA project [94]	60 GHz	5G
2014	Quasi Deterministic Radio Channel Generator model (QuaDRiGa) (Extension of WINNER II) [95]	30 GHz	5G
2015	ETSI-ISG project [96–98]	50-300 GHz	5G
2016	mmMAGIC project [88]	up to 100 GHz	5G
2017	3GPP TR 38.900 - 3D channel model [5]	up to 100 GHz	5G

Table 2.1: The main mmWave Channel Models over the last two decades. The content of the table is chosen from [8].

2.5 Blockage Modelling

Blockage modelling at the mmWave band has attracted researchers' attention in the past few years. Two main approaches have been followed: intensive measurement campaigns, especially for human blockages for different frequency bands, and simulation modelling for blockage attenuations. In the literature, the simulation modelling for blockage effect on the received signal at any point located within a limited cell size could be summarised into two main steps:

1. The first step in simulation modelling is defining the blockers' distribution and density within the cell. Two well-known distributions have been considered by

researchers: a) The homogeneous Poisson point process (PPP) distribution for defining blocker locations. Most of the studies that use the PPP distribution need it to derive the probability density function of the number of blockers from the equations of the PPP distribution, such as the following: references [99, 100]. b) The uniform distribution for blockers, which is followed by many studies, such as: [101–104].

2. The second important step in the simulation modelling for blockage effects is to compute the attenuation that each blocker induces when it blocks the LOS path. In this approach, different diffraction theories are used to compute the attenuation in the deep shadow of the blocker, such as: the knife-edge diffraction theory (KED), the geometrical theory of diffraction (GTD), and the uniform geometrical theory of diffraction (UTD). Due to the simplicity of the first, i.e. KED theory, the 3GPP standards body [5] considers it for modelling blockage in mmWave band. This is discussed in detail in Chapters 4 and 5.

2.5.1 The Importance of Understanding the Dynamic Blockage Effect on the mmWave Channel

As stated in Section 2.1.2, dynamic blockage is a serious issue in mmWave communication systems. Dynamic blockages, such as moving people, cars and buses, cause rapid fluctuations in the mmWave channel, leading to losses in the signal strength of up to 30-40 dB [68, 105, 106]. Therefore, accurate modelling of the dynamics of blockage is essential for developing reliable transceivers for mmWave systems [107]. The authors of [107] introduce a novel spatial dynamic channel sounding system at a frequency of 60 GHz. Based on the results in [100, 108], the authors propose that dynamic blockage plays an important role in the engineering design of mmWave cellular systems. Blockages impact on the channel propagation and achieving the optimum antenna configuration for a given environment [109]. Understanding the behaviour of dynamic blockages could provide an important assessment of the future fully adaptive beamforming. Reference [110] state that the process of environment digitalisation is one of the factors that will enable advanced beamforming approaches to be used. They

used ray-tracing tools to investigate pencil-beam forming techniques, assuming full knowledge of the channel characteristics. Thus, we believe that a more in-depth understanding of dynamic blockage behaviour in directional mmWave communications, especially in V2I communication, will help to improve the overall quality of service of the mmWave system.

2.6 Finite-State Markov Chain Model

For any sequence of a limited number of events, if the probability of one event depends only on the previous event, then this stochastic model is called a Markov chain model. The behaviour of any sequence of repeated events can be described by a Markov chain model that consists of several states, where each state represents one of the possible events. The transition probabilities between the events are obtained by observation or by some statistical knowledge. Fig. 2.10 shows a simplified example of two states Markov chain model. Chapter 3 discusses Markov chain in more detail.

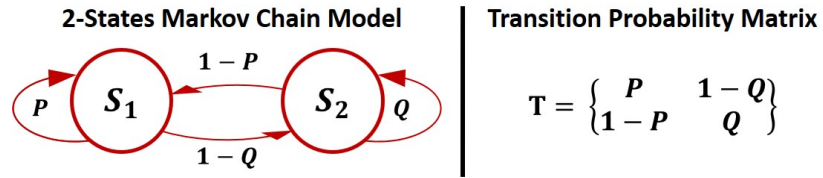


Figure 2.10: Example of 2-States Markov chain model.

The finite-state Markov chain model (FSMC), which consists of a limited number of states, has been a very useful modelling approach for different aspects and applications of communication systems. For example, Gilbert and Elliott modelled the burst-noise over a communication channel using a two-state Markov model to simulate low noise/high noise [111]. Also, for the second-generation (2G) communication systems, finite-state Markov channel has been applied [112]. One Markov chain of two-states, *Good* and *Bad* states representing the shadowing level, was used to simulate land mobile satellite channel modelling [113, 114]. The Markov chain model can be used further to efficiently simulate the dynamic channel attenuation resulting due to blockage effects, which this thesis aims to achieve. That is discussed in the next section.

2.7 Thesis Main Research Scope

Having discussed most of the related topics to mmWave systems, it is clear from the above subsection that capturing the behaviour of dynamic blockages is essential for channel modelling; however, this remains a topic that needs further investigation. Modelling the dynamic channel attenuation surrounding a moving transceiver can be done with complex models such as ray tracing tool or 3D geometric models. However, these models come with very high computational complexity. There is an essential need to develop new efficient mathematical models, such as using the Markov chain approach discussed in Section 2.6, that accurately captures the dynamic channel attenuation. Thus, one of the main aims of this thesis is to efficiently model the effect of dynamic blockage for a V2I mmWave communication system using two proposed Markov chain models, which is studied in Chapters 3 and 4. This includes computing the resulting dynamic attenuation and how the mmWave channel changes subject to this. The attenuation of small-sized blockage objects, such as those the size of road signs, has also not been sufficiently investigated in the literature, so Chapter 5 of the thesis provides an intensive measurement campaign, simulation modelling, and full system evaluation.

2.8 Conclusion

This chapter has provided a fundamental overview of the mmWave band in general. It discussed different phenomena of signal propagation with mainly focus on diffraction phenomena. Also, it entailed a detailed discussion about several propagation loss factors which appear to be serious challenges for mmWave band in comparison with sub-6 GHz band. The chapter also reviewed the main aspects of mmWave channel modelling and highlighted the main existing standards and projects in this regard. That is followed by a brief introduction to Markov chain model and how it has been used in the literature for channel modelling and other communications aspects. Finally, the chapter meant for shedding light on the blockage issue for mmWave band and explained how it is essential to have a further investigation, which explains the research scope of this thesis.

Chapter 3

Markov Chain for Modelling 3D Blockage In mmWave V2I Communications

3.1 Introduction

As discussed in Chapter 2, sensitivity to blockage is a serious challenge that faces the application of mmWave communications. Motion makes the problem even more challenging. The sudden appearance and disappearance of the blockers surrounding a transceiver causes rapid fluctuations and severely affects the performance of the overall system. Therefore, accurate modelling of the dynamics of blockage is essential for developing reliable transceivers for mmWave systems [107]. As such, there is a need for a reliable model that accurately captures the dynamic channel attenuations, which this thesis aims to achieve. In this chapter we present a simple and efficient model.

The following subsections present a brief overview of the application considered in this chapter, which is vehicular communications since the dynamic feature is clear. Then, we briefly discuss the possible modelling approaches and highlight the main related work that has used the Markov chain as a modelling approach. The last two subsections outline the main contributions of the chapter and describe the structure of this chapter.

3.1.1 Considered Application (Vehicular Communications)

Autonomous vehicles are equipped with many sensors that collect data up to hundreds of megabits per second [115]. It is predicted that autonomous vehicles will be

A major part of this chapter is published in IEEE VTC, 2019 [17].

equipped with as many as 200 sensors per car by 2020 [116]. This would provide a vast amount of data that may need to be shared with other vehicles for safety purposes [117]. Thus, the fourth generation (4G) [118], which can offer data rates of 100 Mbits/s, may not be sufficient for future vehicular communication [119]. Nonetheless, some attractive features of the millimetre wave (mmWave) band frequency range (from 30 GHz to 300 GHz) include very high data rates, and low latency, making this a promising candidate to be applied in future vehicle-to-everything (V2X) communication systems [39], [120]. One of the challenges for mmWave communication systems is the blockage effect due to the narrow beams of the mmWave band [51]. Since it is very sensitive to blockage, this effect on the performance of the mmWave system, particularly for V2I, needs to be understood.

3.1.2 Possible Propagation Modelling Approaches

As stated in [121], there are several methods for radio propagation modelling and defining the statistical characteristics of the received signal. These can be determined in two categories: empirical, e.g. WINNER projects [122], and three-dimensional (3D) geometric-based propagation models, where the latter can be done either by simulation or analytically. The geometric-based propagation models fall into two categories: first, the full ray optic tool is an accurate method for modelling the radio propagation, which uses computer programs to solve Maxwell's equations [123]. The advantage of the ray-tracing tool is the ability to establish all possible propagation paths, and this provides the angular information, delay and the received power for each path. However, by understanding the concept of path propagation [124], the ray-tracing approach can be simplified into a 3D map-based geometric model [121], which is a well-known approach. This is the second category of the map-based models.

There are some advantages and disadvantages to each of these propagation tools. The empirical methods do not account for the impact of the antenna pattern or the BS-RX distance, which is the main disadvantage of this method [121]. On the other hand, the ray-tracing approach is a very accurate model, but its computational complexity is greater than the others. Assessing the impact of blockage on the signal strength using

the simplified 3D map-based approach gives a reasonable approximation of reality, but it is still computationally intensive. We are interested in simplifying these propagation models even further. Thus, in this chapter, we propose an efficient Markov chain model that accurately captures the dynamics of blockages and the resulting attenuations. We first, in the following section, briefly present the exiting studies that use the Markov chain to study the blockage effects.

3.1.2.1 Markov Chain Blockage Models in the Related Literature

Modelling the blockage event using the Markov chain is not a new concept. A simple two-state Markov model has been used in several studies in the literature; the author of [125] introduces a two-state Markov chain approximation, using fade and non-fade states, for slow Rayleigh fading channels. Likewise, reference [126] uses two-state Markov, shadowed and non-shadowed states, to capture the blockage for indoor populated environments. Reference [127] developed two approaches using a Markov model for modelling the blockage event: a two-state Markov chain and a four-state piecewise linear modelling approach. These are used to model a human blocker in an outdoor environment where there is only a single TX-RX LOS. Moreover, reference [128] defines a Markov model with three states: non-line of sight (NLOS), line of sight (LOS) and no signal. Reference [129] investigated the spatial correlation of the blockage LOS and NLOS probabilities in urban mmWave systems, showing that the dependency between the receiver states at different times due to the motion of the receiver. Reference [130] extracted transition probabilities of the evolution in the line of sight (LOS) blockage of the V2V system using a three-state Markov chain with actual measurements of different environments. However, this study did not outline when the signal gets blocked, how many blockers there are and how much attenuation they cause. The frequency band used was between 2 GHz and 6 GHz, rather than considering mmWave frequencies. Understanding the effect of blockage on the V2I links therefore still requires further research.

3.1.3 Main Contributions

The main contributions of this chapter are as follows:

1. Investigating the impact of blockers on the received signal strength of a mobile receiver and the behaviour of the dynamics of the blockage surrounding the moving transceiver. The key focus of this chapter is to capture the spatial dependency between adjacent sample points along the mobile receiver track.
2. Simplifying the 3D geometric blockage model into a very efficient Markov chain model.
3. Although a Markov chain requires stationarity, we introduce a novel approach to make the model applicable even in non-stationary cases: splitting the sample point track into several sectors and then representing each one with a different Markov chain.

This chapter is organised as follows: in Section 3.2 the three-dimensional (3D) geometric blockage model is introduced, with two scenarios: stationary and non-stationary. The propagation scenarios and the computation of the channel capacity are also discussed in this section. The next section, Section 3.3, presents the Markov chain model, explaining how it is constructed and how the transition probabilities are computed. In this section, the solution for the non-stationary scenario is also proposed. Simulation comparisons and results are outlined in Section 3.4, and finally Section 3.5 presents the conclusion.

3.2 The 3D Geometric Blockage Model

3.2.1 System Model

We have created a three-dimensional (3D) geometric model in MATLAB, which models an outdoor scenario for a mobile transceiver that moves around a base station. The base station (BS) with h_T height is located around the centre of an area A_T . The area

between the BS and the receiver is filled with blockers that are uniformly distributed with a blockage density $\varepsilon = \frac{N_{BL}}{A_T}$, where N_{BL} is the total number of blockers. The mobile transceiver, with height h_R , moves along the receiver track that goes around the BS, as in Fig. 3.1.

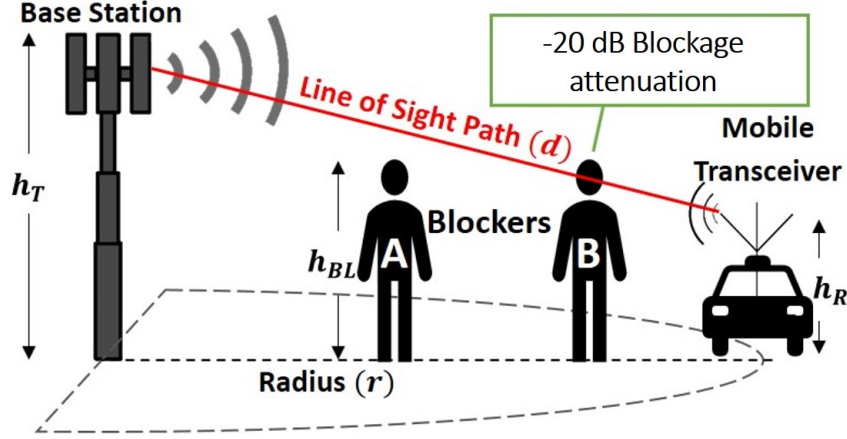


Figure 3.1: An example the 3D geometric blockage model

We are interested in investigating the effect of blocker dynamics surrounding the mobile transceiver on the line of sight (LOS) path. Thus, in this chapter, we only consider the LOS path, whilst ignoring all other reflected or diffracted paths. The effects of only two types of blocker are considered. The blockers are either human bodies or other cars. For the sake of simplicity, and based on measurements provided by several other studies, we assume that each blocker introduces a fixed attenuation value. This approach has been adopted by several studies in the field. If the LOS signal passes through one human blocker, its power will drop by 20 dB [9], while it will drop by 40 dB [62] if the blocker is another car or a tinted glass window. The more blockers that cross the LOS path, the more attenuation the signal experiences. This model can easily be extended to more realistic models, as in [5].

3.2.1.1 The Average Number of Blockers

As the mobile transceiver moves along the receiver track over the RX sample points, the MATLAB function counts the number of blockers that block the LOS path between the mobile transceiver and the BS. This number is then stored in a vector called the

average number of blockers sequence \mathbf{v}_{BL} with the dimension $1 \times N$, where N is the number of uniformly distributed RX sample points. This also corresponds to the sample times t_1 to t_N . However, due to the height difference between the BS and the RX, sometimes the signal travels over the blocker. Thus, only blockers that cross the LOS signal path are counted, such as blocker B in Fig. 3.1, while blocker A is not. Running the simulation repeatedly with a M Monte Carlo run results in an $M \times N$ matrix, which will be used later in this chapter to construct the transition probability matrix for the Markov chain model. We have defined a simple analytical approach for computing the average number of blockers affected by the BS-RX d distance and the blocker width w , which is expressed as follows:

$$N' = \varepsilon \times w \times d \quad (3.1)$$

where $\varepsilon = \frac{N_{BL}}{A_T}$ is the blocker density per unit area. The variable A_T represents the total area, and N_{BL} is the total number of blockers that exist in area A_T . The variable w is the cross-sectional width of one blocker. As shown in Fig. 3.2 (b), the BS location is at coordinates (x_0, y_0, z_0) . The scalar d is the length of the direct LOS path from the BS to each RX sample point (x, y, z) , which changes based on how far the RX sample point is from the BS. This is computed as follows:

$$d = \sqrt{(x_0 - x)^2 + (y_0 - y)^2 + (z_0 - z)^2} \quad (\text{m}) \quad (3.2)$$

3.2.1.2 The Gradient of the Average Number of Blockers

It is clear from (3.1) that the ε and w parameters are fixed across the receiver track, while the scalar d is the only term that changes with the RX movement. However, we assume that the BS and RX heights do not change, so the only variables in (3.1) that change, due to the RX movement, are the x-coordinate or the y-coordinate. If we assume that the mobile transceiver is moving straight along the x-axis, the only parameter that changes with the movement in (3.1) is the x-coordinate value; therefore,

$d = x$. Thus, the gradient \mathcal{G} of the average number of blockers N' is as follows:

$$\mathcal{G} = \frac{\partial N'}{\partial x} = \frac{\varepsilon \times w \times x}{\sqrt{(x_0 - x)^2 + (y_0 - y)^2 + (z_0 - z)^2}} \quad (3.3)$$

3.2.2 The Receiver Track Scenarios

The average number of blockers crossing the LOS path is influenced by the BS-RX distance. Hence, it is influenced by the shape of the receiver track that the mobile transceiver is following. However, to convert the geometric model into a Markov chain model, statistical stationarity is required for the average number of blockers N' , i.e. (3.1). The stationary term here means that the average number of blockers does not show a significant fluctuation over time. This point is explained in detail in Section 3.3. In the following subsection, we discuss two scenarios: a stationary trajectory (circular) and then a non-stationary case (straight-line).

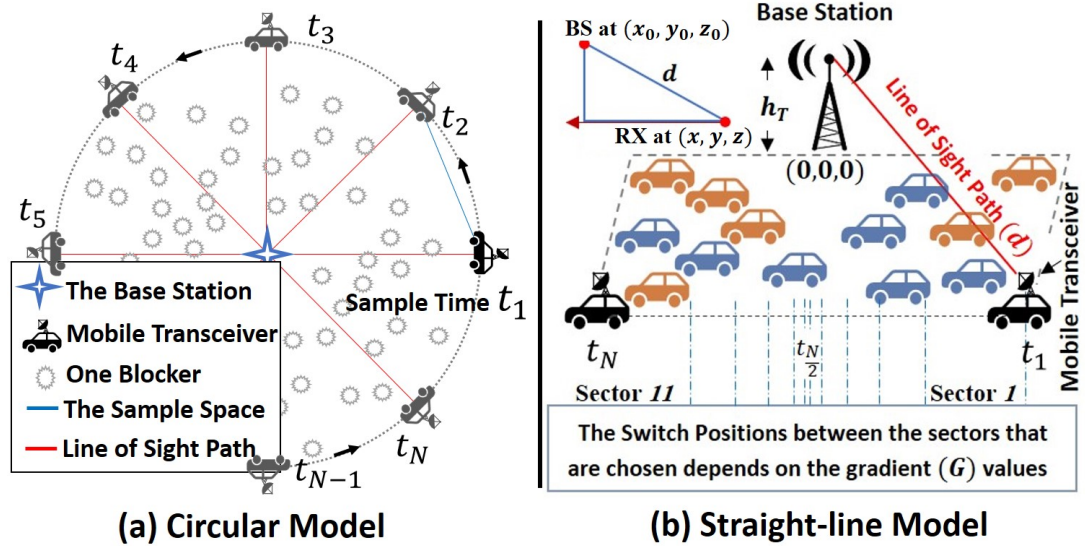


Figure 3.2: The of the 3D geometric model. (a) Circular. (b) Straight-line.

3.2.2.1 Stationary Scenario (Circular-shape Track)

In this scenario, the BS is at the centre of the circle and the receiver track is laid on the circumference, as in Fig. 3.2 (a). The purpose of having a circular track, where the distance to the base station is the same, r , is to keep the same average number of blockers at all sample locations. This scenario is stationary, so the average number of blockers in (3.1) will be $N' = K_1$, where K_1 is a constant. In this scenario, the blockers are assumed to be human bodies.

3.2.2.2 Non-stationary Scenario (Straight-line Track)

In this scenario, the mobile transceiver is moving along a straight-line track and passing the base station, as shown in Fig. 3.2 (b). The transceiver track is a straight line with a total length of 170 m, and it is 15 m from the BS. Since the BS is located around the centre of the track, the BS-RX separation distance towards the two ends of the track is longer than in the middle of the track. The longer the BS-RX distance, the greater the chance that more blockers will cross the LOS path. Unlike the previous scenario, there is a significant difference in the average number of blockers in a sample point located in the middle compared with a sample point toward the end of the track. The average number of blockers in (3.1) will be $N' = K_2 \times d$, where K_2 is a constant. The scalar d is the direct length of the LOS path, i.e. (3.2). The blockers here are cars that follow the same direction.

3.2.3 Propagation Cases

As stated above, we only consider the LOS path propagation. Since there is a limited number of blockers distributed in the area between the base station and the mobile transceiver, two possible scenarios could take place at each RX sample point along the receiver track: either the LOS path is clear with no blocker, or it is blocked by one or more blockers. Thus, we consider two propagation cases:

1- LOS Propagation: When no blocker crosses the LOS path between the BS and the RX, the main factor that affects the received signal is the path loss, which should

be high, considering the high frequency of mmWave. Thus, from Friis' equation, the received power [131] can be written as a function of the antennas' directivity, D_R and D_T , and the free-space path-loss, $P_L = (4\pi d/\lambda)^2$. The wavelength λ is much smaller than the separation distance d , so the farfield assumption is made, and assuming 100% efficient antennas for theoretical analysis.

$$P_R = \frac{P_T D_T D_R}{P_L} \quad (\text{W}) \quad (3.4)$$

2- Blocked LOS Propagation: In the presence of blockers, since the attenuation that each blocker causes is known, this attenuation term can be added to (3.4). As mentioned above, this depends on the blocker type; if it is another car, then it introduces 40 dB [62] of attenuation, while a human body blockage causes a 20 dB loss [9]. In this propagation scenario, i.e. when the LOS path is blocked, we also assume that the received signal suffers from Rayleigh fading due to the blocker effect. The unit power is equal to $|R^2|$, where $|R|$ is the Rayleigh fading amplitude. Equation (3.5) is only considered when the signal passes through one or more blocker, i.e. $N' \geq 1$; otherwise, for the sake of simplicity, it is not considered.

$$P_R = \frac{P_T D_T D_R |R^2|}{P_L N' P_{BL}} \quad (\text{W}) \quad (3.5)$$

To show the difference between the two propagation scenarios, the received power of both have been plotted in Fig. 3.3, which illustrates a small sector of the receiver track that has several RX sample points. In this example, the carrier frequency $f_c=30$ GHz, and the BS-RX distance is 10 m. The antennas' directivity and the Rayleigh fading terms are ignored here. As shown in the figure, when a human body blocker appears, it causes a 20 dB drop in the received signal, i.e. the red dashed curve in Fig. 3.3. This shadow effect lasts for several sample points depending on the blocker's width and how far it is from the mobile transceiver. The brown dotted curve in the figure is the received power averaged over 10 Monte Carlo runs; for each run, the blocker is located at a random position. However, it is possible in some other scenarios that the shadow of two or more blockers overlaps, which results in higher attenuation.

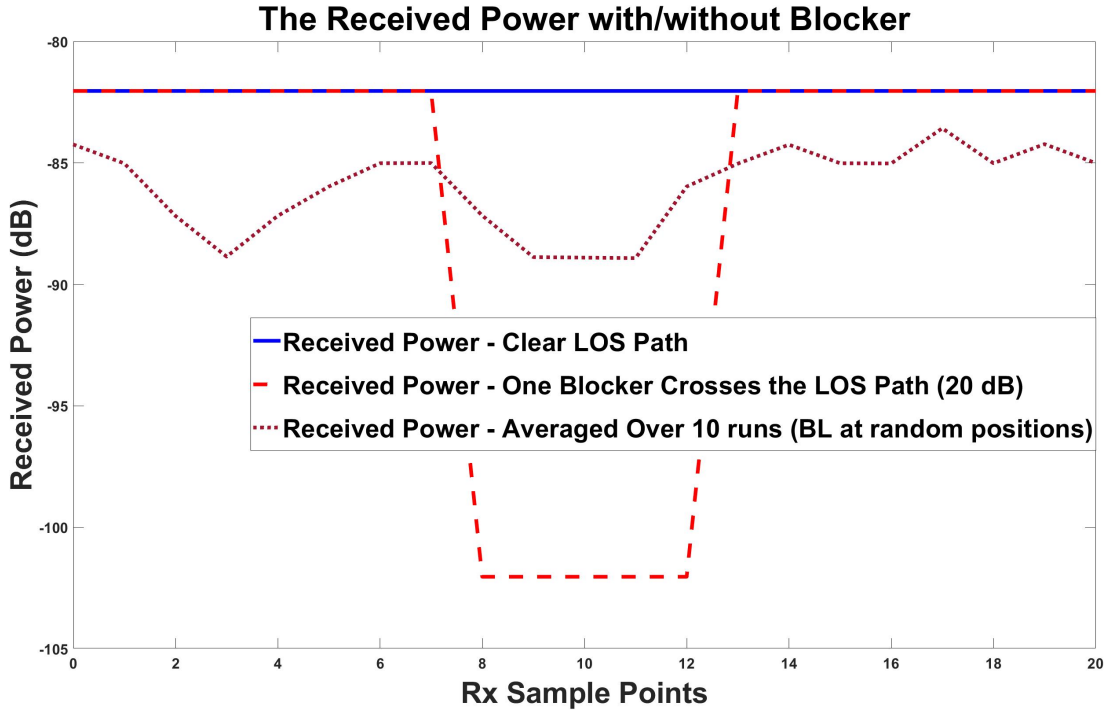


Figure 3.3: The received power with and without a blocker crossing the LOS between BS and RX. For the brown doted curve we have one blocker that is located at random location with each run, 20 sample points, and $M=10$ runs.

3.2.4 Spectral Efficiency

The maximum spectral efficiency achieved through the additive white Gaussian noise (AWGN) channel at each RX sample point is obtained using the well-known Shannon equation, which is expressed as a function of the signal-to-noise ratio [132]:

$$C = \log_2\{1 + P_R/N_o\} \quad (\text{bits/s/Hz}) \quad (3.6)$$

The received spectral efficiency is used as a metric to compare the performance of the proposed Markov chain model with the geometric model. The channel capacity shows clear dependence on the signal-to-noise SNR ratio value. According to [70], the relationship between the channel capacity and the SNR is divided into two regions as

follows:

$$\log_2(1 + \text{SNR}) \approx \text{SNR} \log_2(e) \quad \text{when} \quad \text{SNR} \approx 0 \quad (3.7)$$

$$\log_2(1 + \text{SNR}) \approx \log_2(\text{SNR}) \quad \text{when} \quad \text{SNR} \gg 1 \quad (3.8)$$

When the SNR value is low, the channel capacity increases linearly with it, which means doubling the SNR value yields whilst doubling the channel capacity. Increasing the SNR by 3 dB doubles the output capacity. However, the higher the SNR value, the less effect it has on the output channel capacity. Based on the second region, it has a logarithmic relationship, i.e. we only get one more bit per dimension for every 3 dB increase in the SNR value.

Based on the received power of Fig. 3.3, the corresponding spectral efficiency for all the three curves is plotted in Fig. 3.4. Since the SNR is high, a 20 dB drop in the received power, due to the blocker, produces ≈ 7 bits/s/Hz drop in the received spectral efficiency, i.e. 1 bit/s/Hz for every 3 dB.

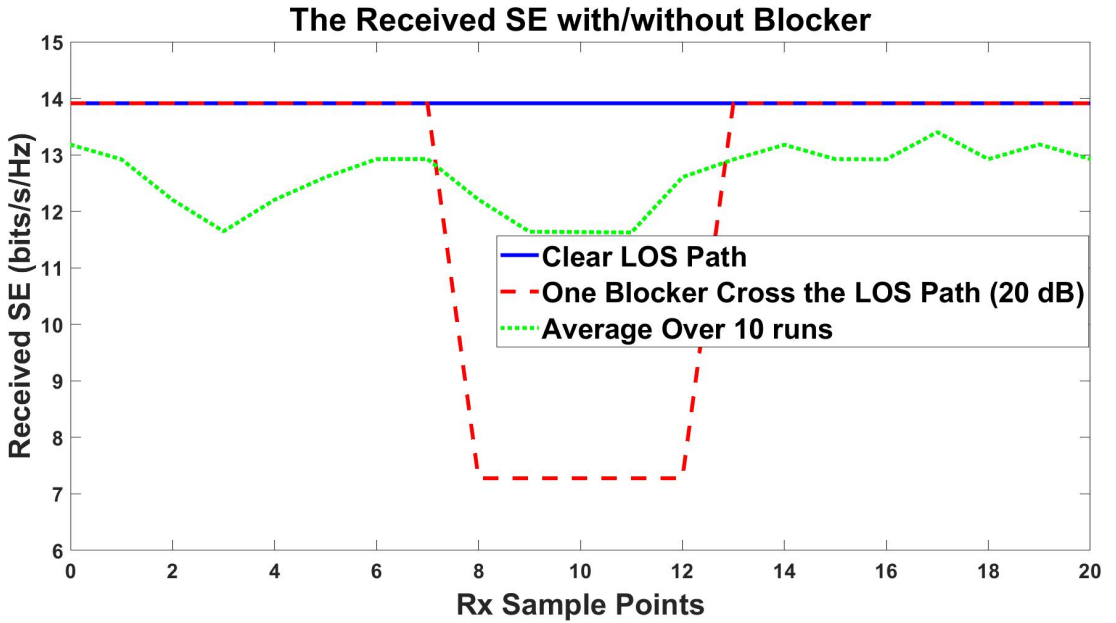


Figure 3.4: The received spectral efficiency with and without a blocker crossing the LOS between BS and RX. For the green dotted curve we have one blocker that is located at random location with each run, 20 sample points, and $M=10$ runs.

3.2.5 Geometric Model Computation Process

Although the simplified 3D geometric model is a good approach to study the radio propagation for a given field in the presence of time-varying blockage effects, the computational process is quite complex. It is also necessary to consider that at each sample point along the receiver track we need to check how many blockers cross the LOS path. Whenever we change the settings or the field, the whole process should be repeated to count the number of blockers that block the LOS path. However, what is proposed in this chapter is a Markov chain model that efficiently captures the dynamics of the blockers surrounding a moving transceiver. This will be explained in detail in the following section. Table 3.1 shows a comparison between the three models: ray-tracing, geometric and Markov chain.

Model	Complexity	Performance	Time Consumption
Full Commercial Ray Tracing	Very High	Best	Very High
Simplified Geometric	High	Good	High
Markov Chain	Very low	Good	Very low

Table 3.1: System and Antenna Parameters

3.3 The Markov Chain Model

Markov chain is a very useful tool for simplifying a complex stochastic scenario. Based on the present event, we can predict the future event since the future and past events are independent and the present event is known. Thus, in order to capture the dynamics of the average number of blockers encompassing a moving transceiver, we can replace the high-computational 3D geometric model with the efficient Markov chain model. Our goal in this chapter is to convert the 3D geometric model that counts the effective number of blockers crossing the LOS path into a Markov chain model.

3.3.1 Overview of Markov Chain

First, this subsection is a very brief overview of the Markov chain model. We begin by defining the random variable, \mathcal{X} , as an output of a random event. The random process, or the stochastic process, is a set of random variables over time $\{\mathcal{X}_n; n = 0, 1, 2, \dots\}$ with finite or infinite state space \mathcal{S} [133]. If the set consists of a natural number then it is called a discrete-time random process, while if the numbers are real, it is called a continuous-time random process. There are several categories of random process, one of which is Markov chain [134].

As stated in [134, 135], the Markov chain model has a particular property that makes it a very useful tool: the Markov or memoryless property. Each Markov chain has a state space that contains all possible states; we define it here as $\mathcal{S} = \{S_0, S_1, \dots\}$. The random process is called the Markov process if the following condition applies: for future states, the conditional distribution, given the current and past states of the process, depends only on the current states. This means the future state is independent of the past state. If U is an event that depends only on the subset $\{\mathcal{X}_{n-1}, \mathcal{X}_{n-2}, \dots, 0\}$, then for any state j and k in the state space \mathcal{S} is as follows [133]:

$$P_{jk} = P(\mathcal{X}_{n+1} = k | \mathcal{X}_n = j) \quad (3.9)$$

3.3.2 Straight-line Scenario and the Markov Reducible Characteristic

First, let us define the “irreducible” and “reducible” terms. The Markov chain process is “irreducible” only if any state can reach any other state within the chain no matter how many steps are required, or how long it takes to reach it [134]. Although not every state of the Markov chain in Fig. 3.5 (a) is directly connected to the other states, this Markov chain is irreducible because any state can reach the others, no matter how many steps are required to reach the destination. On the other hand, a Markov chain is “reducible” if there are one or more states that are not reachable by all the other states, where there is a portion of the Markov chain that has only one way, and no coming back as in Fig. 3.5 (b) [136].

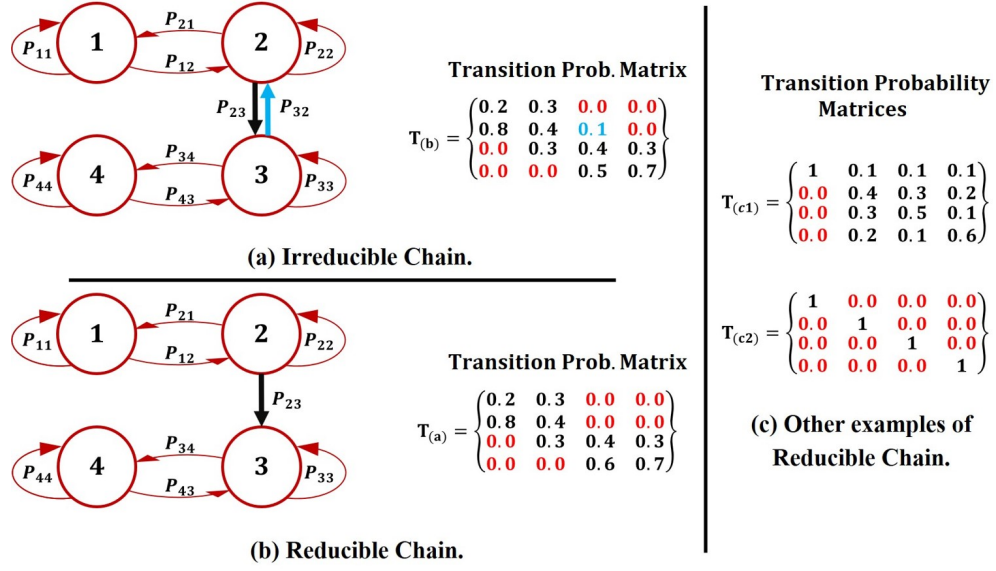


Figure 3.5: Example of reducible and irreducible Markov chains.

Fig. 3.5 shows some examples of Markov chains with dummy transition matrices. Each column of a transition matrix represents the set of transition probabilities of movement from this state to all other states. The transition probabilities of each column should sum to one. Taking Fig. 3.5 (b) as an example, the second column of the transition matrix shows all the possible arrows connecting state 2 to itself or other states. Since state 2 has no connection to state 4, the transition probability P_{24} is zero. However, the second row of the transition matrix shows how the second state is approached by other states. There are no arrows connecting state 3 or 4 to state 2. These are backward-disconnected, with neither a direct nor indirect connection. Thus, Fig. 3.5 (b) is a reducible chain since states 1 and 2 are not reachable from state 3 or 4. For instance, if we run a Markov chain sequence based on the transition probability matrix $T_{(a)}$, we would get a sequence similar to $\{1, 2, 1, 2, 2, 3, \dots, 3, 3, 4, 3\}$. There is no way back to the first part. However, one reducible Markov chain could be split into two small irreducible Markov chains. If we split states 1 and 2 from states 3 and 4 in Fig. 3.5 (b), we have two small irreducible Markov chains. Fig. 3.5 (c) shows more examples of reducible Markov chains. However, this reducible characteristic is what happens when we directly convert the straight-line scenario of the geometric model into one Markov chain. This will be explained in detail in the following subsections.

Let us take two examples of propagation scenarios for the two cases. We assume that each state represents the number of blockers crossing the direct LOS path between the base station and the receiver, i.e. state 1 means one object blocks the LOS, etc. First, for the irreducible case, i.e. Fig. 3.5 (a), that could happen if we assume that a receiver (RX), surrounded by blockers, moves through three different areas with different blockage densities, (i.e. from non-crowded to crowded then again back to a non-crowded place). First, the RX is either blocked by one or two blockers maximum. Then, when the RX moves to a crowded place, it is more likely to be blocked by three or four blockers; once it passed the congested area, it is then blocked by one or two blockers. However, for the reducible case, i.e. Fig. 3.5 (b), that could happen if we assume that the RX was blocked by three very wide buildings that completely block the receiver location. That means there is no way back from state three to state two.

3.3.3 Converting the 3D Blockage Geometric Model into a Markov Chain Model

The 3D geometric blockage model could be converted into a simple discrete Markov chain model [137] based on a transition matrix, \mathbf{T} , as shown in Fig. 3.6. The probabilities here are created from data samples of the 3D geometric model. The Markov chain model consists of several states where each state represents the number of blockers that cross the signal path. As shown in Fig. 3.6, the first state, S_0 , indicates that there is no blocker between the mobile transceiver and the BS, while S_1 is the state when there is one blocker, etc. P_{01} is the transition probability from state S_0 – no blocker – to state S_1 – 1 blocker – and so on. The transition probabilities from any state sum to one. However, when the mobile transceiver moves from one sample point to another, the transition can go from any state to itself again, or to any other state, to represent the LOS path status based on the given transition probability, as shown in the v_{BL} blocker sequence example at the bottom of Fig. 3.6.

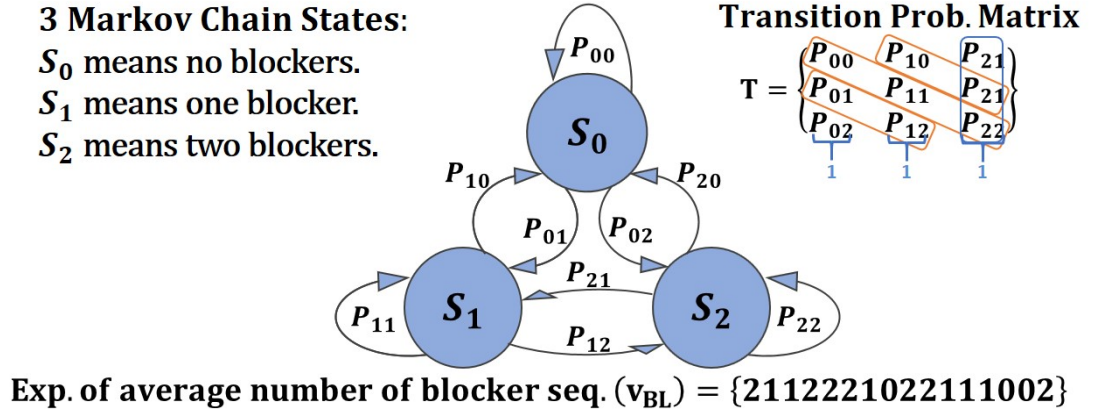


Figure 3.6: Example of Markov chain with 3 states representing 0, 1 or 2 blockers.

The main goal is to make the Markov chain model produce an average number of blockers sequence, v_{BL} , which matches the statistical behaviour of the geometric model by only using the transition probability matrix \mathbf{T} , where \mathbf{T} is already obtained from the geometric model. In order to be able to compare the results of the two models, their vectors and matrices should have the same dimensions. Therefore, the dimension of the one-run sequence should be size N . Repeating the process of the Markov model M times using the same matrix \mathbf{T} gives $M \times N$ matrix of samples.

3.3.4 Transition Probability Matrices

The transition probability matrix of the Markov chain model can be computed using two approaches: simulation based on the MATLAB geometric model data; or deriving the transition probability analytically.

3.3.4.1 Transition Probability Matrices by Simulation

From the geometric model, we have M number of v_{BL} vectors resulting from M Monte Carlo simulations. These vectors contain the number of blockers that cross the LOS path at each sample point. By analysing the dynamic transition across each vector, we obtain the transition probability matrices. We have M transition probability matrices, one for each iteration. Then, averaging these matrices introduces one matrix \mathbf{T} , on

which the Markov chain model is based. The transition probability matrix is a square matrix with a dimension equal to the maximum possible number of blockers obtained from the geometric model, i.e. $\max(\mathbf{v}_{BL})$. In Fig. 3.6, the transition probability, P_{jk} , from state j to state k is defined by:

$$P_{jk} = \frac{n_{jk}}{\sum_{l=1}^m n_{jl}} \quad (3.10)$$

where n_{jk} is the total number of times that the number of blockers in vector \mathbf{v}_{BL} changes from state j to state k along the receiver track, and m is the number of possible states. Repeating this process for all states allows the matrix \mathbf{T} in Fig. 3.6 to be constructed.

3.3.4.2 Analytical Approach to Computing Transition Probabilities

The transition probability matrix of the Markov chain can also be computed analytically based on some basic knowledge about the environment. For the low-blockage density case, a two-state Markov chain model is used, i.e. no blockers or one blocker. We have a 2-by-2 transition matrix \mathbf{T} . The transition probability from the no-blockers state to the one-blocker state P_{01} is given as:

$$P_{01} = \frac{N_{BL}}{N} \quad (3.11)$$

where N_{BL} is the total number of blockers encountered over the total number of RX sample points N .

However, P_{11} represents the probability that the mobile transceiver remains blocked by the same blocker over time. Blocker size plays an important role in this. The shadow caused by one blocker continues for several sample points, and once it passes the blocker, it switches back to the non-blocker state like an ON-OFF curve. Since blockers have a finite size, the likelihood of staying in the one-blocker state decreases exponentially with the sample time according to the value of P_{11} . The computation of the transition probability P_{11} involves two steps: finding the optimum value for a very small blocker; then, based on the relationship between the blocker size and the

transition probability P_{11} , finding the corresponding value for every possible blocker size.

To derive the optimum value of P_{11} analytically, consider a small blocker that blocks only two sample points; i.e. the state at t_1 , $S(t_1) = 1$ and $S(t_2) = 1$, $S(t_3) = 0$, etc. The best analytical value of P_{11} in this case is found by computing the minimum mean-squared error (MMSE) between the exponential Markov chain and ON-OFF curves:

$$\text{MSE} = \frac{1}{N} \sum_{k=1}^N (S(k) - P_k)^2 \quad (3.12)$$

where $P_k = P_{11}^k$ and it represents the exponential decay of the Markov chain.

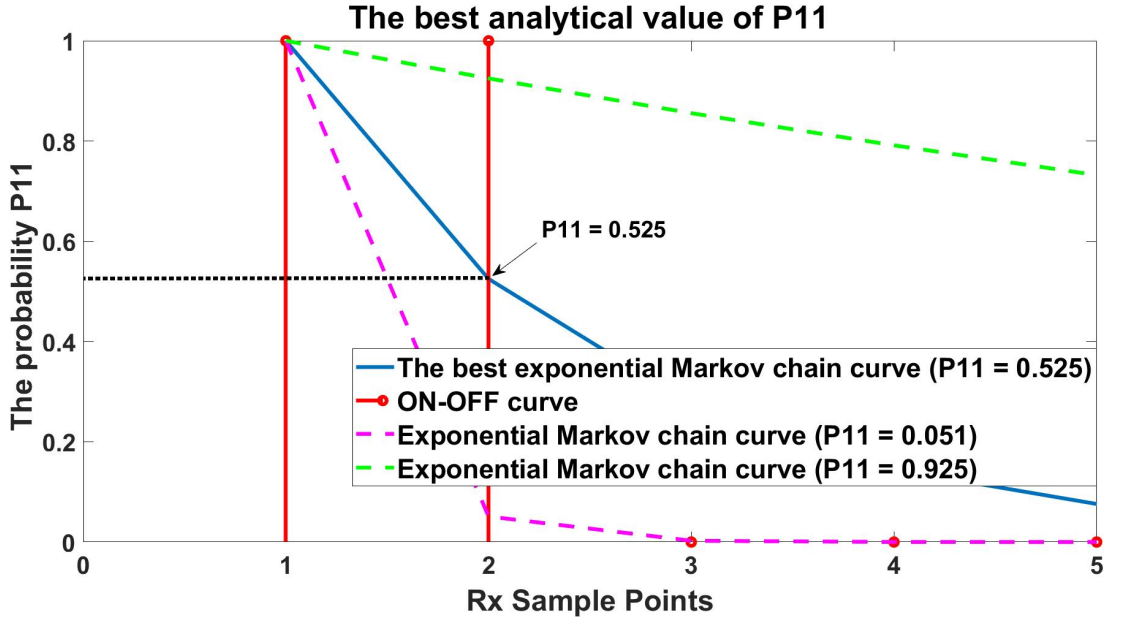


Figure 3.7: The best value of the transition probability P_{11} .

As shown in Fig. 3.7, the optimum value of the transition probability P_{11} corresponding to a very small blocker that leads to the minimum-squared error is $P'_{11}(\text{MMSE}) = 0.525$. In Fig. 3.7, we have plotted the ON-OFF curve that represents a small blocker blocking only two RX sample points, and, after that, it switches to zero. As explained above, the Markov chain model has an exponential decay curve for P_{11} since the probability of being blocked by the same blocker decreases with every new sample point.

We have scanned all possible probabilities, but plotted only the best P_{11} curve – the blue line – and the other two examples – the dash-curves – to show the difference.

The next step after computing the transition probability P_{11} analytically for a small blocker that blocks only two RX sample points, is to use this value as a reference point to compute the transition probability P_{11} for any blocker size. The transition probability P_{11} has a logarithmic relationship with the blocker size. We can use this relationship to find the transition probability for any blocker size. For example, increasing the blocker size from $w_{\text{Ref.}}=0.2$ to $w_{\text{New}}=0.4$ (m) means that the corresponding value $P_{11}(0.4)$ must equal the square root of P_{11} to achieve the MMSE fit. P_{11} of any blocker size can be obtained as follows:

$$P_{11}(w_{\text{New}}) = P_{11}'^{(w_{\text{Ref.}}/w_{\text{New}})} \quad (3.13)$$

A detailed comparison between the simulation and the analytical approaches is provided in Section 3.4.1.

3.3.5 One Markov Chain Model for the Stationary Scenario (Circle)

Due to the stationarity of the circular scenario, one Markov chain is sufficient to model the average number of blockers affecting each RX sample point along the whole track. The first main step is to compute the transition probability matrix. Fig. 3.8 represents the transition probability matrix computed from a geometric model of a circular track. The circle radius is 10 m, and 200 human blockages are uniformly distributed across the area. Considering the size and the number of blockers the blockage density is low. From the matrix, we can see that the maximum number of overlapped blockers is four. Each column of the matrix represents the movement from this state to another, and it should sum to one. The bar on the right shows the corresponding value of each colour. The first column represents the zero-blocker state S_0 , i.e. clear LOS path. Since the blockage density is low, movement from S_0 to S_0 is more likely than from S_0 to any other state, so the first cell is yellow. The second cell in the column representing the

movement from S_0 to S_1 has a lower probability, so it is light blue, and so on.

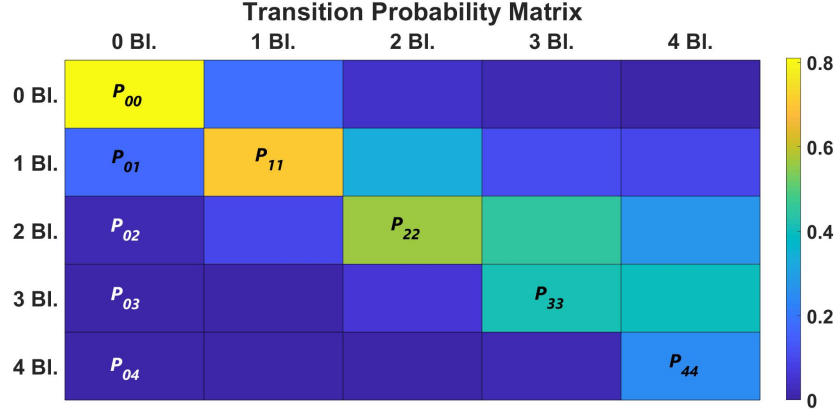


Figure 3.8: The Transition Probability Matrix of a circular scenario. The No. of $N_{BL}=200$, 400 RX sample points, and $M=50$ runs.

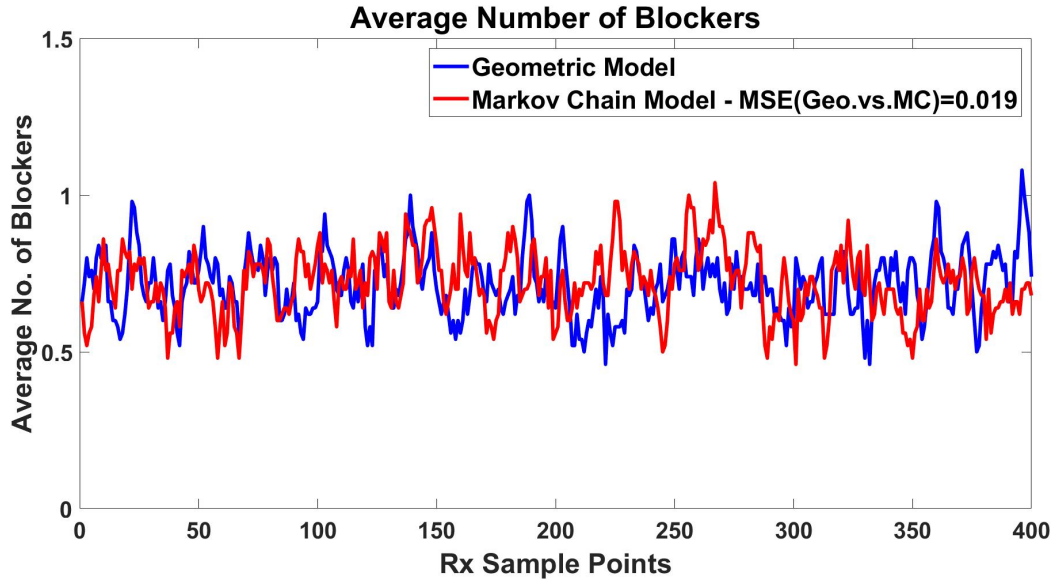


Figure 3.9: Average number of blockers seen by the moving transceiver - the circular scenario. The No. of $N_{BL}=200$, 400 RX sample points, and $M=50$ runs.

With the transition probability matrix ready, we can now efficiently compute the average number of blockers using the Markov chain model. We have significantly reduced the computation process by switching from the geometric to the Markov chain model. Fig. 3.9 shows a comparison between the average number of blockers computed by each model. The MSE between the two curves is 0.019. This low value indicates how good the efficient Markov chain model is.

3.3.6 Multiple Markov Chain Model for the Non-stationary Scenario (Straight-line)

In motorway scenarios, it is more realistic to have a straight-line track (Section 3.2.2.2) than a circular shape (Section 3.2.2.1). The average number of blockers, N' , changes depending on the distance of the mobile transceiver from the BS. The longer the BS-RX distance is, the greater the chance of more blockers. When the mobile transceiver is far from the BS at time t_1 or t_N , i.e. at either edge of the track, it is more likely that the signal will suffer from more blockers than when it is passing by at time $t_{N/2}$. Thus, there is a significant difference in the average number of blockers along the track, as shown in Fig. 3.10.

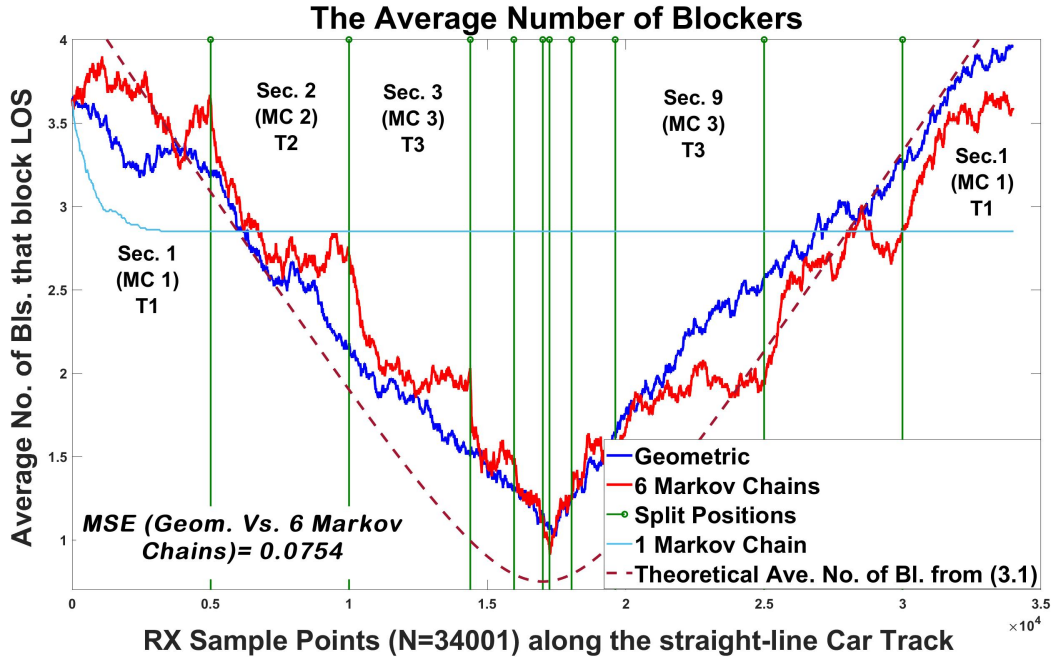


Figure 3.10: The Average number of blockers seen by the moving transceiver - the straight-line scenario. There are 34001 RX sample points along the RX track, which is divided into 11 sectors.

In Fig. 3.10, it is clear that the average number of blockers curve obtained from the simulation results of the geometric model follows the same trend as the theoretical one. However, the Markov chain requires statistical stationarity in the average number of blockers in order to produce results that match the geometric model. This condition

will be difficult to meet in any other mobile transceiver track than the circular shape. Having one Markov chain produced from one transition matrix for the whole mobile transceiver track has been investigated and it fails to achieve the goal of matching the geometric model results, as shown in Fig. 3.10. Due to the high fluctuation in the average number of blockers curve, we found that computing only one transition matrix for the whole track results in a reducible transition matrix, as explained in Section 3.3.1. Thus, the Markov chain constructed using this transition matrix will fail to match the V-shape curve of the geometric model since it will be stuck in one state at some point along the track, as the cyan curve shows in Fig. 3.10.

However, we provide a solution that will make the Markov chain model applicable to the straight-line track scenario. The solution is to split the mobile transceiver track into multiple small sectors aiming to keep the variance of the average number of blockers, N' , within each sector as small as possible. The approach of having multiple Markov chains works very well with the non-stationary scenario. As shown in Fig. 3.10, the MSE value between the geometric model and the six-Markov chains model is very small – 0.075.

In selecting the split-position locations along the mobile transceiver track, the goal is to keep the part of the N' curve that belongs to each sector in an almost steady-state condition. To do so, the gradient \mathcal{G} of the average number of blockers – (3.3) – is obtained and plotted. Then, this curve is divided into small parts along the y-axis, where the split-points are symmetrical with respect to the origin, as shown in Fig. 3.11. This step is subjective; we try to make the sectors small, especially in the regions where the slope of the \mathcal{G} curve is high. Finally, the projections of these points on the \mathcal{G} curve on the x-axis are the best positions to split the x-axis (the sample points along the mobile transceiver track) into small sectors.

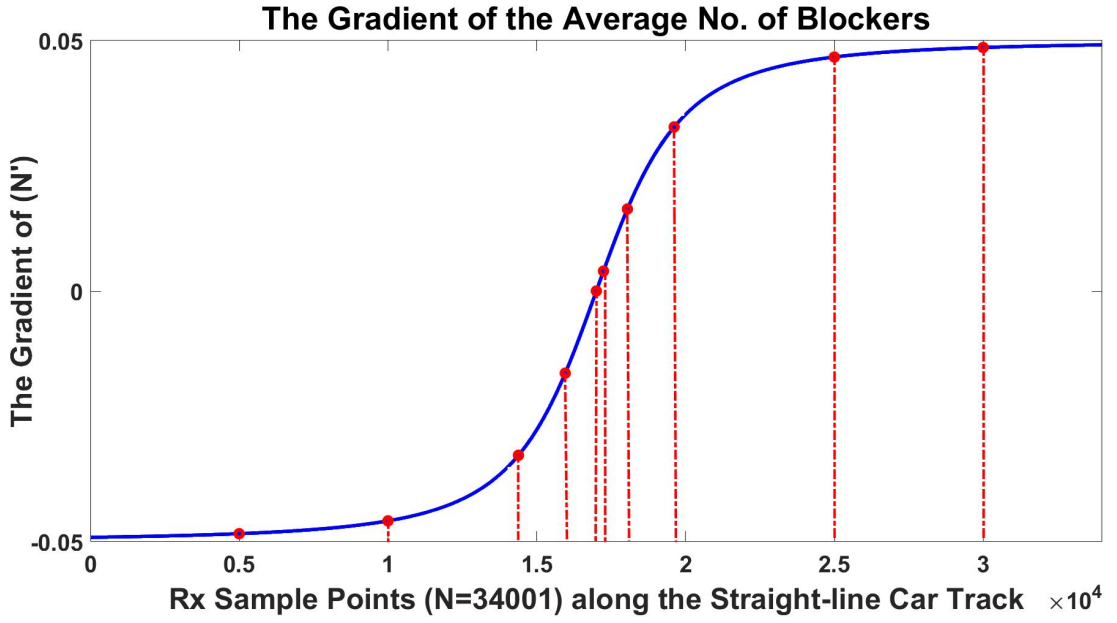


Figure 3.11: The gradient of the average number of blockers seen by a mobile transceiver - the straight-line scenario

The new transition matrices of all small sectors are irreducible, which means each state in the Markov chain is accessible by all other states. Now, the dynamic of the Markov chain will flow smoothly; hence the problem is solved. The parameters of each of these transition probability matrices are computed from the related sectors of the blocker sequence, v_{BL} , of the offline geometric model or by following the analytical approach in Section 3.3.4.2. Each sector is represented by a different Markov chain that is based on the corresponding transition probability matrix \mathbf{T} . Now, for one track, we have multiple Markov chains, that come in sequence order.

However, in Fig. 3.10, due to the symmetrical structure, although the mobile transceiver track has been divided into eleven sectors, only six Markov chains based on six transition probabilities are needed. Sector one and sector eleven are represented by the same Markov chain, and the same \mathbf{T}_1 , and so on. The middle sector is represented by the sixth Markov chain and \mathbf{T}_6 . However, for the handoff process, when switching from one Markov chain to another, the state of the first sample point of the new Markov chain is equal to the last point of the previous chain, (or the nearest state to it) to maintain spatial consistency.

Transmit power	$P_T(Total) = 1\text{W}$	No. of MC states S	up to 10
Noise power	$N_O = -123.91\text{dB}$	Blocker height	$h_{BL} = 1.8\text{m}$
BS height	$h_T = 2.5\text{m}$	Blocker radius (Human)	$r_{BL} = 0.5\text{m}$
RX height	$h_R = 1.5\text{m}$	Car blocker dimensions	$4.75 \times 1.8\text{m}^2$
Carrier frequency	$f_c = 30\text{GHz}$	D_T, D_R in (3.4) and (3.5)	8 Dipole antennas
Sample space	$\lambda/2$	w in (3.1)	2.545 m
The Circular Scenario		The Straight-line Scenario	
Sample points	$N = 400$	Sample points	$N = 34001$
No. of runs	$M = 50$	No. of runs	$M = 100$
Total No. of Bl.	(10, 50, 100, 200, 500)	Total No. of Bl.	$N_{BL} = 50$
Circle Radius r	(10, 15, 20, 25, 30)m	A_T Dimensions (m)	$l_1 = 15, l_2 = 170$

Table 3.2: System and Antenna Parameters

3.4 Comparisons and Results

A comparison between the performance of the two models is required to see how well the Markov chain model captures the blockage phenomena in both circular (Fig. 3.2 (a)) and straight-line (Fig. 3.2 (b)) scenarios. Table 3.2 specifies all the parameters used in the simulation for the two scenarios. First, in the straight-line scenario, we observe that the run-time of the geometric model is 1,000 times the run-time of the Markov chain model. The channel capacity evaluated at each sample point is affected by the average number of blocker vectors over the number of iterations. Therefore, the pattern of the averaged autocorrelation function (ACF) of the channel capacity along the whole track of the proposed Markov chain model is compared with the geometric model in different cases, i.e. different circle radii, and different densities. Up to 10 blocker states are considered for the Markov chain model in order to capture different densities. The ACF is computed as follows:

$$\text{ACF}(\Delta t) = \mathbb{E}[C(t)C(t + \Delta t)] \quad (3.14)$$

Another key comparison is to investigate the empirical cumulative distribution function (ECDF) of the channel capacity obtained using the geometric and Markov chain models, which is computed as follows:

$$\text{ECDF}(c(t)) = P(C \leq c(t)) \quad (3.15)$$

3.4.1 Circular Scenario Results Comparisons

As stated in Section 3.2.2.1, the circular scenario is stationary since the average number of blockers seen at each sample point along the mobile transceiver track remains constant. In this chapter, several circular radii and blocker density scenarios have been investigated. In Table 3.3, the values of the average capacity with very small MSE values indicate that the Markov chain model works very well. It is important to emphasise here how much the appearance of blockers could severely affect the performance of the mmWave system. As is clear in the first part of Table 3.3, the blockage density is affecting the received spectral efficiency. The received spectral efficiency drops significantly as the blockage density increases.

The Overall Average Capacity Along all the Circle Track (bits/s/Hz)							
No. of Bl. N_{BL}	Radii $r=15\text{m}$			Radii r	Bl. No. $N_{BL} = 200$		
	Markov	Geometric	MSE		Markov	Geometric	MSE
10	12.01	12.12	0.0124	10	0.81	0.91	0.01
50	9.19	9.23	0.0016	15	2.73	2.72	0.0001
100	6.44	6.4	0.0016	20	3.78	3.85	0.0049
200	2.72	2.73	0.0001	25	4.43	4.62	0.0361
500	0.07	0.05	0.0004	30	5.12	5.10	0.0004

Table 3.3: Comparison between Markov chain and the Geometric models

Fig. 3.12 also shows a comparison of the average ACF of the Markov chain and the geometric models of different circle radius, ranging from a radius of 10 m to 30 m. The Markov chain curves successfully replicate the results of the geometric model with very limited error for the five different scenarios. Fig. 3.13 shows the ECDF comparison of the two models. At 10% of the overall ECDF of the average capacity,

there is a small error of 0.1 bits/s/Hz; otherwise the Markov chain model fits the geometric model distribution very well.

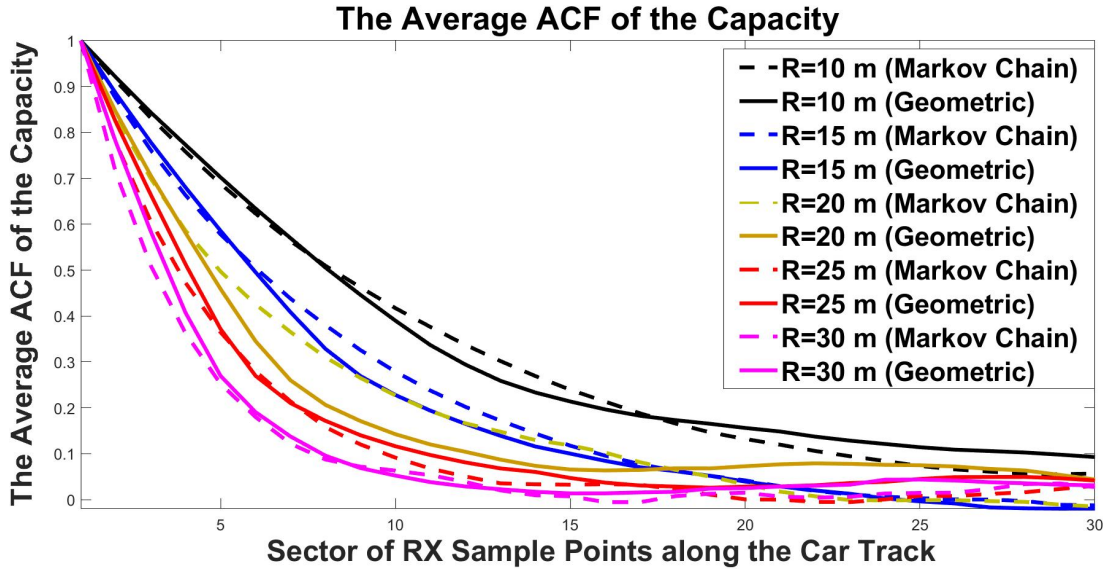


Figure 3.12: Average ACF of the Capacity of the circular track with No. of BL=100, several radii, 400 sample points, and $M=150$ runs

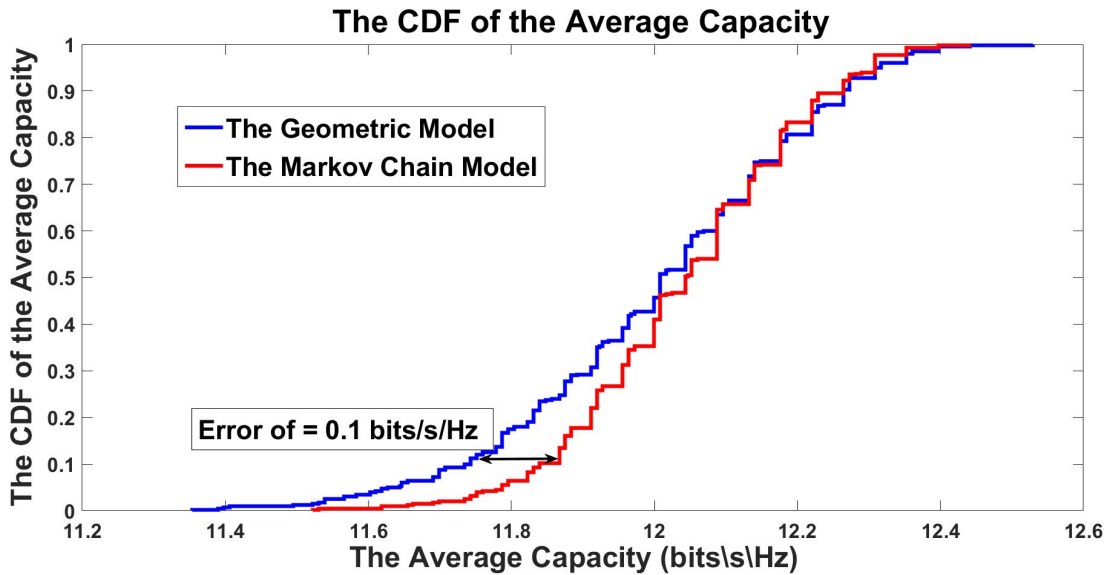


Figure 3.13: The ECDF of the Capacity of the circular track with No. of BL=10, $r=15m$, 400 sample points, and $M=150$ runs

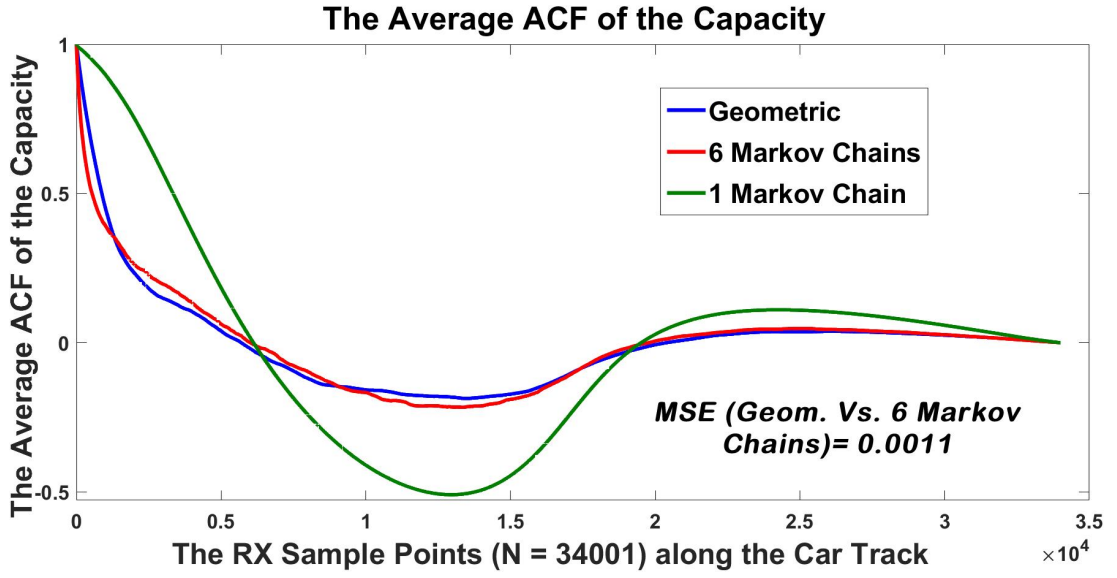


Figure 3.14: The Average ACF of the Capacity of the straight-line track with No. of BL=50, $P_{BL} = 20$ dB, 34001 sample points, and $M=100$ runs

3.4.2 Straight-line Scenario Results Comparisons

As mentioned in Section 3.3.6, the straight-line scenario is non-stationary regarding the average number of blockers. As explained in Fig. 3.2 (b) and Fig. 3.10, the track should be split into small sectors to achieve stationarity within these. Otherwise, the Markov chain model will fail to match the geometric model results, as shown in Fig. 3.14 (the green curve). However, six Markov chains are able to provide an overall average number of blockers that matches the curve of the geometric model (Fig. 3.10). The splitting positions are chosen carefully, ensuring each split has limited variance in the average number of blockers using the gradient of the average number of blockers, \mathcal{G} , as described in Section 3.3.6. The result is that the average ACF curve in Fig. 3.14 fits the geometric curve with a small MSE of 0.0011.

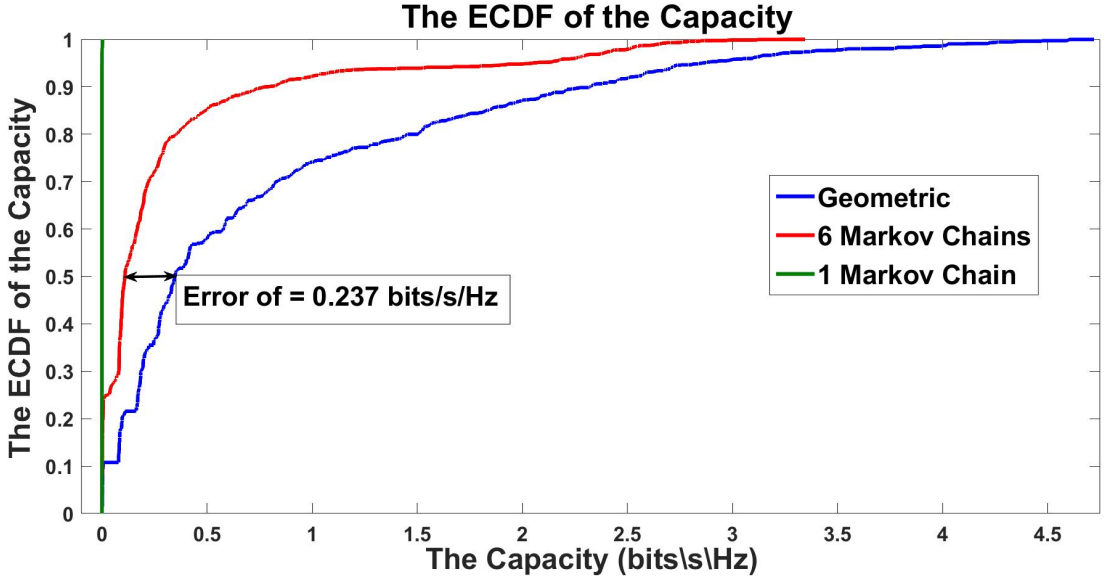


Figure 3.15: The ECDF of the Capacity of the straight-line track with No. of BL=50, 34001 sample points, and $M=100$ runs

The ECDF curve in Fig. 3.15 of the six combined Markov chains also follows the same pattern as the geometric model. At 50% of the overall ECDF of the average capacity, there is a small error of 0.237 bits/s/Hz. The error here is higher than in Fig. 3.13 due to the higher blocker attenuation, 40 dB, caused by a car. Even a small difference in N' , between the Markov chain and the geometric, would result in a higher error than in a case where the blocker attenuation is 20 dB. One Markov chain produces around three blockers as an average number over the entire track (see Fig. 3.10), and each one of them attenuates the signal by 40 dB. This results in almost zero capacity, as shown in Fig. 3.15. Having several Markov chains, instead of one chain, significantly improves the modelling accuracy.

3.4.3 Transition Probability (Simulation versus Analytical)

Fig. 3.16 presents a comparison of the analytical (Section 3.3.4.2) and the simulation approaches to computing the transition probabilities. The results of the two methods match each other, which means that the transition probability matrix could be generated analytically without using the geometric model. Fig. 3.16 (a) presents the transi-

tion probability P_{01} as a function of the number of blockers in the area. They have a linear relationship. However, Fig. 3.16(b) shows the transition probability P_{11} against the dimension of the blocker and, as shown in the figure, they have a logarithmic relationship. The reference blocker size in (3.13) is 0.235 m, which is equal to the sample space, i.e. two sample points are blocked, and the transition probability $P_{11} = 0.525$. Based on this, we used (3.13) to generate the rest of the curve.

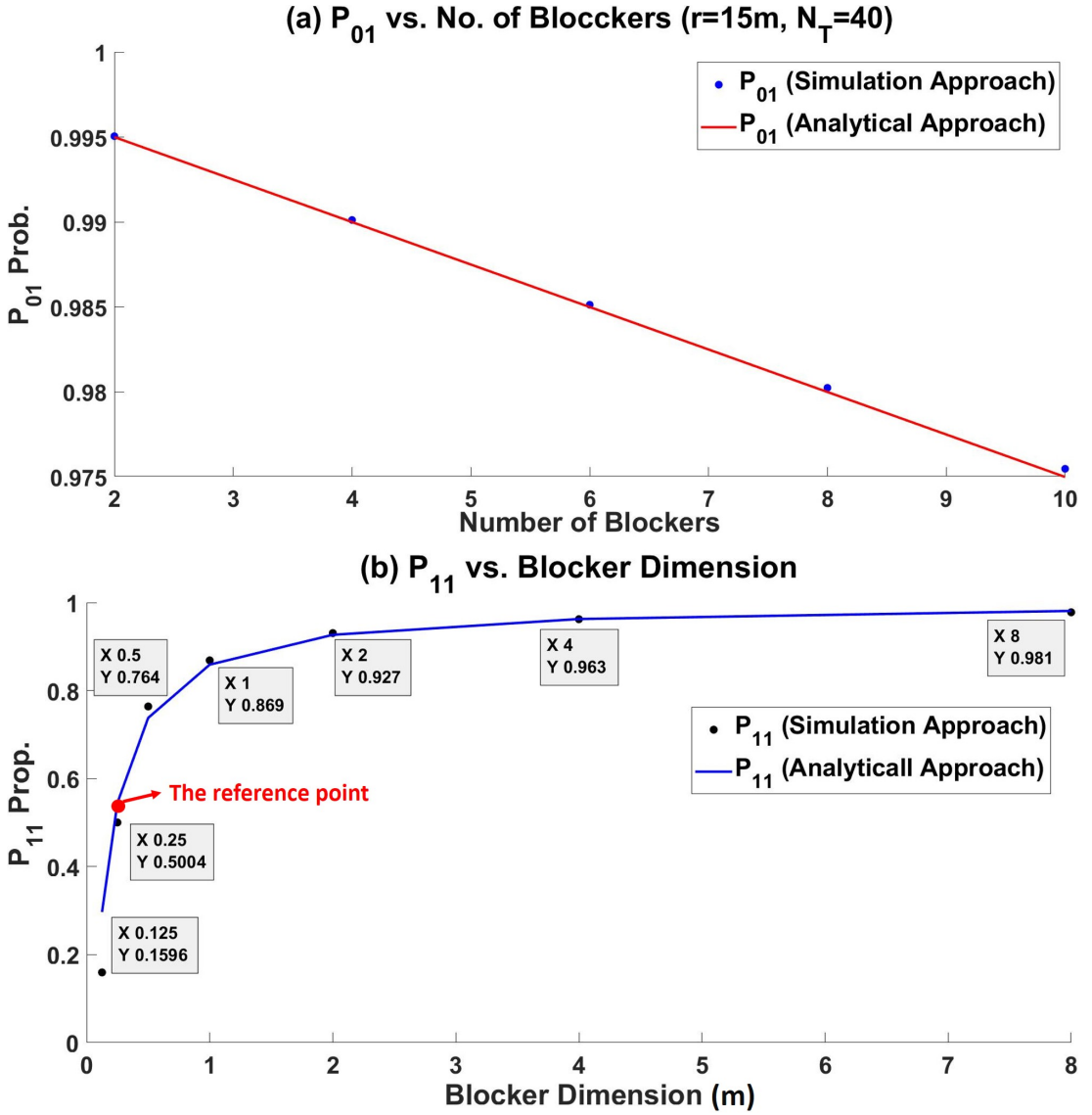


Figure 3.16: Analytical and simulation comparison. (a) P_{01} . (b) P_{11} .

3.5 Conclusion

A 3D geometric model was introduced to investigate the impact of blockage in mmWave V2I communications. Although the geometric model gives a reasonable approximation of reality, it is computationally intensive. Hence, the computationally efficient Markov chain model is presented in this chapter. The proposed Markov chain model successfully captures the dynamic attenuation surrounding a moving transceiver. It is found that analytically derived transition probabilities match well with those obtained from the geometric model, which means that the transition probability matrix could be generated without running the geometric model. The average capacity results of the Markov chain model also match those obtained from the geometric model. The patterns of the average ACF and the ECDF of the capacity also show that the proposed Markov chain model works very well with limited error. Although a Markov chain requires statistical stationarity, this chapter proposed a novel solution by dividing the receiver track into several sectors represented by several Markov chains. The resulting model is shown to fit the results from the geometric model well.

It is clear from the results of this chapter that the Markov chain model is a very good approach. However, in order to overcome the limitations of the Markov chain model presented in this chapter, we propose a more advanced sum of Markov chains model in the next chapter.

Chapter 4

Adaptive Sum of Markov Chains for Modelling 3D Blockage in mmWave V2I Communications

4.1 Introduction

As noted in the previous two chapters, at mmWave frequencies, the diffraction of electromagnetic waves around blockers is less likely to occur than at microwave frequencies due to the significant difference in the size of a typical blocker and the wavelength [138], so even small obstacles can influence the signal strength [139]. For instance, the human body attenuates the mmWave signal in the range of 20 to 25 dB [9]. The probability of LOS blockage increases exponentially as the receiver moves further away from BS [99]. Accurately and efficiently modelling the dynamic attenuations caused by blockers is essential for reliable mmWave communications. The simple Markov chain presented in Chapter 3 is very efficient and shows good performance in capturing the blockage attenuations.

The following subsection presents the limitations of the model presented in Chapter 3 that we overcome in the new model in this chapter. Section 4.1.2 provides a brief overview of the related work and discussion of how human blockage has been modelled in the literature. Section 4.1.4 states the main contributions, and then the structure of this chapter is presented in Section 4.1.5.

This chapter is published in IEEE Transactions on Vehicular Technology, 2020 [14].

4.1.1 Limitations of the Simple Markov chain model of Chapter 3

Although the existing Markov chain model exhibits very good performance, and it has very low complexity, it does have some limitations:

1. For non-stationary scenarios, dividing the receiver track into sectors is required, and this is not easily automated.
2. Obtaining closed-form results for the transition probability matrix is complex; especially for the high average number of blockers cases. For these cases, the only practical option is to feed in the transition probability matrix from simulations of the geometric model.
3. To use the Markov chain for any new scenario, the transition probability matrix is also needed beforehand; otherwise the simple Markov chain cannot compute the attenuations caused by blockers. Although it might be possible to have the transition probability matrix for some scenarios, this is not always feasible.
4. This model works very well for simple scenarios with simplified assumptions, such as assuming the attenuation caused by a blocker is a fixed value (e.g. 20 dB). Then, the total attenuation is simply the given fixed value (e.g. 20 dB) multiplied by the number of blockers. However, for this simplified Markov chain model, it is difficult to adapt if the attenuation value changes due to the blocker's location and orientation.

These limitations encourage us to develop a more flexible model that maintains the advantages of the Markov chain model and overcomes the limitations described above. Thus, in this chapter, we propose an adaptive Markov chain function that overcomes all the limitations described.

4.1.2 Related Work on Human Blockage

The literature review provided in Chapter 3 applies here as well. However, in this section, we describe more references that are relevant to this specific chapter. In the liter-

ature, human blockage has been extensively investigated for several frequency ranges of the mmWave band. In this section, we briefly present the related work.

The impact of human blockage on 60 GHz band has attracted many research endeavours in the early literature based on the IEEE 802.11ad standard. For instance, reference [103] studied outdoor scenarios, and [9, 13, 140] have investigated the indoor environment. Reference [141] has provided analysis and comparisons between different blockage models at 60 GHz. It states that even clothes have a significant impact on the resulting attenuation under some circumstances. Other studies investigate the influence of human blockage at other frequency ranges of 28 GHz [142] and the 73 GHz band was investigated by some studies in [87, 127]. Also, the human blockage effect at 28 GHz, 38 GHz, 60 GHz, and 73 GHz frequency bands were studied in [143], which concludes that 28 GHz showed a lower blockage loss compared with the other frequency bands. For two different frequency bands, 26 and 39.5 GHz, the authors of [144] measured the attenuation resulted from one to three human body blockages that are simultaneously crossing the direct LOS path. Reference [87] shows that using directional antennas, one human blocker could attenuate the signal by 30-40 dB. Also, the 11, 16, 28 and 32 GHz bands are studied in [145]. The paper states that increasing the frequency within this range would have no significant influence on the attenuation value.

Two-dimensional (2D) blockage models were proposed in [146, 147], where the elevation angle is ignored. However, by considering the difference in the height of the transmitter or the receiver and the blockage dimensions, the signal could travel over the blockage and not be affected at all. The 3GPP standards body [5] proposed two empirical-based blockage models for a mmWave system. Reference [101] analyses the effect of blockage on the relationship between the blockage rate and the data frame length. Reference [102] studied using their novel model the behaviour of correlation between the LOS path and the reflected paths that are affected by human blockage around receivers. However, they have avoided using the 3GPP blockage model to reduce complexity; instead, they assumed that each blocker introduces a fixed 20 dB loss.

4.1.3 How have human blockers been modelled in the literature?

Two main steps are required in blockage modelling. The first is determining the blocker location: distributing blockers uniformly over the area around the base station (BS) and the receiver (RX) is a well-known approach e.g. see [101–104]. The second step is to model the attenuation profile caused by a given blocker. For the mmWave band, several approaches have been undertaken by researchers to model the attenuation caused by a human blockage. Below, the main approaches are briefly outlined and listed in increasing order of complexity:

1. A simple approach [17, 103] is to have a fixed attenuation where each human blockage introduces a fixed attenuation of 20 dB, which is based on experimental results.
2. Modelling a blocker as a screen and then applying knife-edge diffraction theory to get the attenuation value is a common approach in the literature. In the METIS channel models [12], simple knife-edge diffraction is used to calculate the loss value geometrically. This is one of two empirical-based blockage models proposed by the 3GPP standards body [5]. Several other studies use double-sided knife-edges and examine it with some measurements, such as [87]. Their results show that using a directional antenna, one human blocker could attenuate the signal by 30-40 dB when the TX-RX distance is 5m. Reference [148] also introduces some basic rules to use the simplified double knife-edge to model human blocker effects in the mmWave band.
3. Other geometric approaches are used to model a blockage, such as the Kirchhoff KED model and the geometrical theory of diffraction in (GTD) [145]; and the circular cylinder and dielectric elliptic cylinder in [141]. However, these models are much more complex to evaluate.

4.1.4 The Main Contributions

To the best of our knowledge, capturing the dynamic of the blockers surrounding a moving transceiver, and at the same time computing the resulting attenuation has not

been studied in the literature. This chapter investigates blockage effects on the signal strength and captures the dynamics of blockers surrounding a moving transceiver.

1. A novel sum of Markov chains model is proposed that successfully captures the dynamics of the blockage surrounding a moving transceiver that moves around a base station. Moreover, the performance of the proposed model shows a very good match with the geometric model results, but with much less complexity. The simplicity of the proposed model is a very good feature; it is based on several two-state Markov chains combined in parallel. To estimate the right average number of blockers for any given environment, the only three inputs required for the model are the right choice of the transition probability, the length of a blocker, and how many chains are required.
2. One of the advantages of the proposed sum of Markov chains model is that it can work very well for both stationary and non-stationary scenarios; non-stationary means the average number of blockers can vary depending on the TX-RX distance and the blocker locations since the probability of LOS blockage increases exponentially with TX-RX distance [99]. This is due to the adaptive feature of the proposed model, which can adapt and predict the correct dynamics of the average number of blockers for any given environment.
3. To add more novelty to the work, any attenuation model could be integrated easily within the novel proposed sum of Markov chains model. One of the blockage models that could be used is the third-generation partnership project (3GPP) knife-edge diffraction (KED) blockage model; in this chapter, it is adopted and integrated within the proposed model. Thus, the resulting attenuation of the model is not only based on how many blockers there are but also on the relative locations of these blockers.

4.1.5 Chapter Organisation

The chapter is organised as follows: in Section 4.2 the system model of the chapter and propagation scenarios are presented. Then, Section 4.3 presents two approaches

considered in this chapter to compute the attenuation value caused by blockers. First is assigning a fixed attenuation value for each blocker, and the other approach is to represent each blocker by the 3GPP blockage model [5], which is a thin vertical screen. That is along with an attenuation profile of RF lab measurements. Then, in the following section, state of the art blockage models – geometric, and Markov chain (MC) – are introduced with a brief overview of the model of Chapter 3. Section 4.5 comprises the core of the chapter, where the novel sum of Markov chains (sum of MC) model is proposed. Section 4.6 provides results and discussion of all the models. Section 4.7 shows a summary of the work and highlights the main achievements, and suggests possible directions for future work. The last section provides a link to the MATLAB code used in this chapter.

4.2 The System Model

To investigate the blockage effect on the mmWave V2I communication system, in the proposed system model we assume that there is a mobile transceiver at the top of a vehicle that is moving around a base station in the presence of a sparse distribution of blockers located randomly in the area. Since in the mmWave band the line-of-sight (LOS) path is far stronger than other non-LOS paths [149], we only consider the LOS path in this chapter. Whenever the LOS path hits a blocker, attenuation is applied in the model. As in [103], we assume the angle of arrival does not change. In the following subsections, the geometric model parameters and the theoretical approach for computing the average number blockers are defined. Then, propagation scenarios are introduced to investigate how much a blocker could affect the received signal strength. Finally, since the channel capacity is simple to compute, we use it as a metric to compare the performance of different approaches to model blockage.

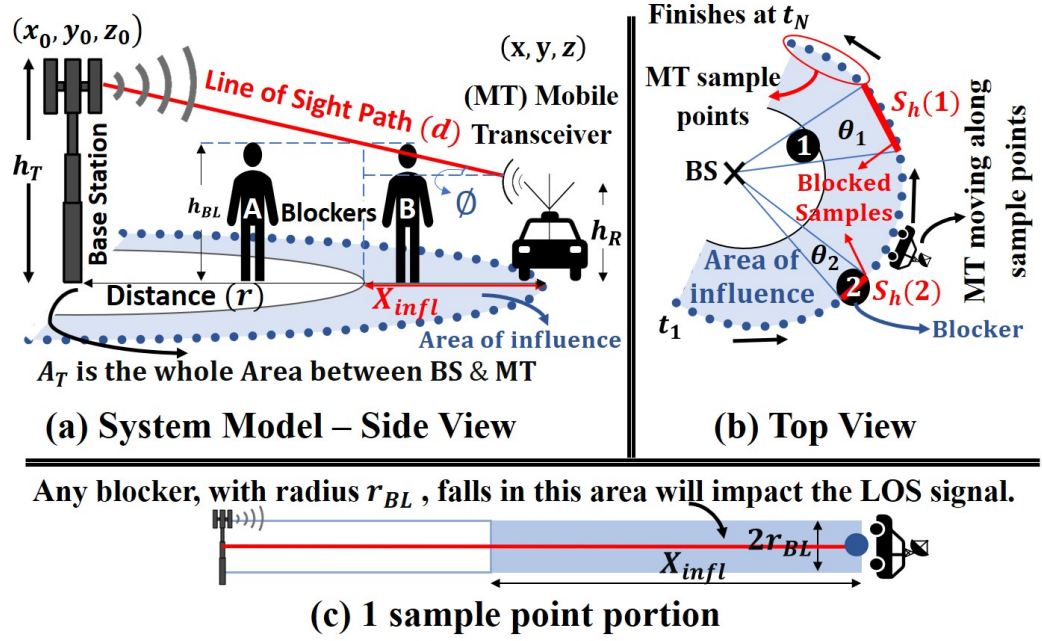


Figure 4.1: The System Model.

4.2.1 Introducing the system model parameters

The system model, as shown in Fig. 4.1 (a), consists of a base station (BS), with height h_T , and a mobile transceiver (MT), with height h_R , moving around the BS following a specified track. For simulation purposes, there are N sample points that are equally spaced and located on the track. The MT starts moving at sample point 1 and finishes at sample point N , with corresponding sample times t_1 to t_N . Within the area A_T , there are N_{BL} blockers that could block the LOS path between the BS and the MT. Any blocker shape could be used; the blocker radius is defined as r_{BL} and the height is h_{BL} . If a signal passes through any one of these blockers, its power will be significantly reduced. The more blockers, the greater the overall attenuation the signal experiences. Since the BS is assumed to be higher than the blockers, only the blockers that cross the LOS signal path are counted, such as blocker B in Fig. 4.1 (a), while blocker A would not have any effect. Therefore, this only refers to the blockers located within the area of influence, which is where the direct LOS path does not exceed the

height of a blocker h_{BL} . The scalar X_{infl} is the distance between the two edges of the influence-ring in Fig. 4.1 (a) and it is found from the elevation angle ϕ of the LOS path as follows:

$$\tan \phi = \frac{(h_T - h_R)}{r} = \frac{(h_{BL} - h_R)}{X_{infl}} \quad (4.1)$$

$$X_{infl} = r \frac{(h_{BL} - h_R)}{(h_T - h_R)} \quad (4.2)$$

The scalar r is the BS-MT distance in the xy-plane while d is the length of the LOS path from the BS at coordinates (x_0, y_0, z_0) to the MT sample point (x, y, z) . The average number of blockers at each sample point is obtained by multiplying the blocker density by the area of visibility of this sample point, as shown in Fig. 4.1 (c), which is a slight modification of what was shown in Chapter 3. It is calculated as follows:

$$N'_G = \varepsilon(2r_{BL}X_{infl}) \quad (4.3)$$

where $\varepsilon = \frac{N_{BL}}{A_T}$ is the average number of blockers per unit area, i.e. the blocker density, and N_{BL} is the total number of blockers that exist in area A_T . The scalar r_{BL} is the radius of one blocker assuming it is a sheet where the width of the sheet corresponds to the diameter of an equivalent cylinder representation of the blocker.

As in [101–104] blockers are uniformly distributed, and they can be located anywhere in area A_T . However, the shadow caused by a blocker projection on the MT track will vary based on the blocker location. Fig. 4.1 (b) shows that a blocker (No. 1) that is far from the MT track will create a longer shadow on the MT track with length $S_h(1)$. A shorter shadow area with length, $S_h(2)$, on the other hand, will be created by a blocker located very close to the MT track, (No. 2). These are the two extreme cases of the blocker location. The scalar $S_h(1)$ is found by applying the arc length formula as follows:

$$\theta_1 = \frac{(2r_{BL})}{r - X_{infl}} = \frac{S_h(1)}{r} \Rightarrow S_h(1) = \frac{(2r_{BL})r}{r - X_{infl}} \quad (4.4)$$

Similarly, for blocker No. 2 located on the MT track, the projected sector equals the diameter of the blocker, i.e. $S_h(2) = 2r_{BL}$. The average shadow-length, $\overline{S_h}$, caused by one blocker is obtained from integrating over all possible blocker locations, which

yields the average length as:

$$\begin{aligned}\overline{Sh} = \mathbb{E}(Sh) &= \int_{S_h(2)}^{S_h(1)} \frac{x}{S_h(1) - S_h(2)} dx = \frac{(S_h(1))^2 - (S_h(2))^2}{2(S_h(1) - S_h(2))} \\ &= \frac{S_h(1) + S_h(2)}{2} = r_{BL} \left(\frac{r}{r - X_{infl}} + 1 \right) \quad (\text{m})\end{aligned} \quad (4.5)$$

However, by dividing the number of sample points over the total length of the MT track, we get the number of samples per unit length, i.e. N/L . Thus, the average number of sample points that is affected by one blocker is obtained by multiplying (4.5) by N/L as follows:

$$l_B = \overline{Sh} \frac{N}{L} = \frac{Nr_{BL}}{L} \left(\frac{r}{r - X_{infl}} + 1 \right) \quad (\text{Samples}) \quad (4.6)$$

In this chapter, we assume a sparse distribution of the blockers, where the total blocker length or breadth is much less than the BS-MT distance. As stated in the METIS model [12], for sparsely populated environments, when the shadow of two different blockers overlap, the net overall attenuation is the sum of the attenuation values (in dB) for each blocker. The computation of blocker attenuation is explained in detail in Section 4.3.

4.2.2 Propagation scenarios

As noted at the start of this section, we only consider the LOS path in this chapter. Thus, similar to [150–152] one of two cases is possible; the LOS path is either non-blocked or blocked:

4.2.2.1 LOS Propagation

when no blocker crosses the LOS path between the BS and the MT, the Friis equation of the received power [131] can be written as a function of the antennas' directivity, D_T and D_R , and the free-space path-loss, $P_L = (4\pi d/\lambda)^2$. The wavelength, λ , is much smaller than the direct LOS path, d , i.e. the farfield assumption is made and assuming

100 % efficient antennas for theoretical analysis.

$$P_R(t) = \frac{P_T(t)D_TD_R}{P_L} \quad (\text{W}) \quad (4.7)$$

4.2.2.2 Blocked LOS Propagation

in the presence of blockers, since the attenuation that each blocker causes P_{BL} is known, this can be added to (4.7). The received LOS signal in (4.7) will be partially blocked and hence suffer from unit power Rayleigh fading due to the blocker effect, with power equal to $|R^2|$, where $|R|$ is the Rayleigh fading amplitude. Equation (4.8) is only considered when the signal passes through one or more blockers, i.e. $N'_G \geq 1$:

$$P_R(t) = \frac{P_T(t)D_TD_R|R^2|}{P_LN'_GP_{BL}} \quad (\text{W}) \quad (4.8)$$

4.2.3 Channel Capacity

Thanks to the well-known Shannon equation [132], the maximum spectral efficiency at each sample point can be obtained easily using the resulting received power as in (4.9). The channel capacity will be used later to compare the performance of different blockage models.

$$C(t) = \log_2\{1 + P_R(t)/N_o\} \quad (\text{bits/s/Hz}) \quad (4.9)$$

We used the channel capacity as a metric to evaluate the proposed model. We know that the Shannon capacity is an upper-bound, and actual system performance should be below that. However, reference [153] has shown that the Long Term Evolution (LTE) link capacity curve is close to the Shannon upper-bound with only a small difference. Hence, the Shannon equation provides a good way to approximate the performance of real systems using adaptive modulation and coding.

4.3 Blockage Attenuation Approaches

When a blocker crosses the direct path between a transmitter and a receiver, it attenuates the signal and makes it weaker. The resulting attenuation depends on the blocker's kind, size, location, and orientation. As mention in Section 4.1.2, several approaches have been undertaken by researchers to evaluate the attenuation caused by a human blockage. In this chapter, we consider two approaches listed in increasing order of complexity. Moreover, towards the end of this section, an attenuation profile of lab measurements is presented, which could be used as well.

4.3.1 Approach (1): Fixed-Attenuation Blockage Model

For the mmWave band, if a signal passes through one human blocker, its power will drop roughly by 20 dB [9]. This simple approach involves introducing a 20 dB fixed attenuation value whenever the LOS path is blocked.

4.3.2 Approach (2): 3GPP Blockage Model

In principle, not every human body that crosses the LOS path should attenuate the signal by a fixed value of 20 dB. The attenuation of a blocker will vary depending on the location and the orientation. However, 3GPP provides a simple model to capture the loss caused by the shadow of a blocker using the concept of knife-edge diffraction [5, 12]. Each blocker is represented by a rectangular screen, as in Fig. 4.2, and the loss due to four edges of the screen is:

$$P_{BL} = -20 \log_{10} (1 - (F_{h1} + F_{h2}) (F_{w1} + F_{w2})) \text{ (dB)} \quad (4.10)$$

where F_{h1} , F_{h2} , F_{w1} , and F_{w2} are the diffraction values associated with the four edges; h denotes the blocker height and w the width, as shown in Fig. 4.2. Every edge will cause shadowing equal to:

$$F = \frac{\text{atan} \left(\pm \frac{\pi}{2} \sqrt{\frac{\pi}{\lambda} (D_1 + D_2 - d)} \right)}{\pi} \quad (4.11)$$

where λ is the wavelength, D_1 and D_2 are the projected distance from the BS and MT nodes to the screen, and d is the projected distance between the BS and MT nodes.

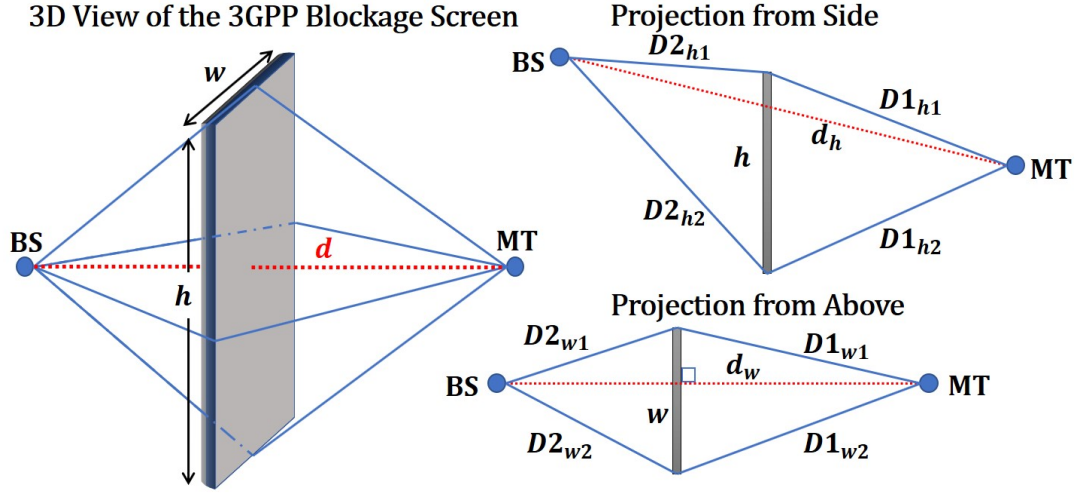


Figure 4.2: Shadowing screen model adopted from [5, 12].

According to [5, 12], when one of the BS or MT nodes moves, the orientation of the screen should be rotated around its centre to be perpendicular to the LOS path, and at the same time stay vertical on the ground. Thus, if we look at this from the top view, the cross-section of the rotation makes a circular shape that has a diameter equal to the 3GPP screen width. This is not a cylinder, just a screen that rotates around its centre to always be perpendicular to the LOS path, as shown in case 2 of Fig. 4.3.

Top view of :

- 1) Case 1 : MT sample point blocked by one 3GPP Blockage Screen.
- 2) Case 2 : MT sample point blocked by two overlapped the 3GPP Blockage Screens.

The Loss for Case 1 should be less than for case 2

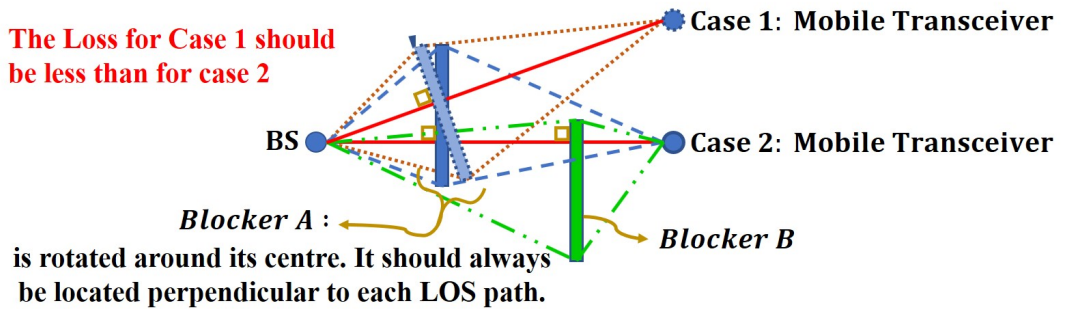


Figure 4.3: Shadow of two overlapped blockers.

According to the METIS project [12], and the 3GPP standard body [5], for a sparse distribution of blockers, when the shadow of two blockers overlapped, each one will attenuate the signal separately. The resulting attenuation for an MT-BS link that is shadowed by two different blockers is obtained as the sum of the two individual losses, as shown in case 2 of Fig. 4.3.

This 3GPP blockage model is adopted in this chapter. Whenever a blocker crosses the LOS path, the above loss equation is applied to obtain the attenuation caused by that blocker. The attenuation value will vary depending on the blockage location. This 3GPP blockage model can be used in the geometric model and the sum of Markov chains model, but not the Markov chain model; that is explained in detail in the next section, in Section 4.4.2.

4.3.3 RF Lab Measurements

Besides these two main approaches, the attenuation profile could be taking from real measurements and applied for all blockers. Experimental work was carried out in an anechoic chamber at Heriot-Watt University where a rectangular copper sheet was placed exactly between two horn antennas, one for the transmitter and one for the receiver, separated by a distance $r = 2$ m. A narrowband measurement was performed, where the frequency was 28 GHz, and the transmitted power was 1 W. The transmitter and the receiver locations were fixed, and the copper sheet was placed in the middle to block the direct path between the transmitter and the receiver. The blocker was moved over several steps from right to left crossing the direct LOS path between the transmitter and the receiver. At each blocker position, the measurement of the resulting attenuation was collected, as presented in Fig. 4.4. The red dash curve represents the measured attenuation of rectangular metal sheet, from Chapter 5, where the blocker is crossing the LOS path at equidistant between the TX and RX. We observed that the location of the blocker plays an important role in the resulting attenuation. The loss equation of the 3GPP blockage model for the same copper blocker is used, and this led to a similar finding. This RF lab measurements could be used as an attenuation profile and adopted as another blocker model.

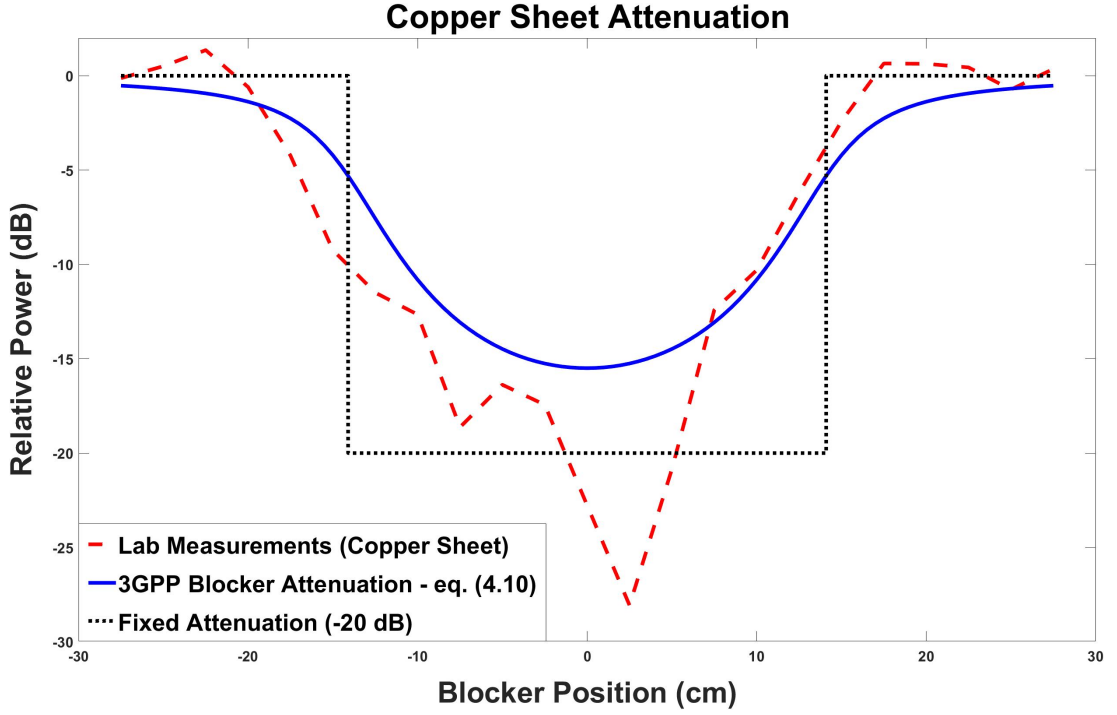


Figure 4.4: Lab-measurement - Attenuation caused by a rectangular copper sheet.

4.4 Methods to Model Blockages in Computer Simulation

For the mmWave band, modelling the blockage effect in open environments can be done in one of several ways listed in decreasing order of complexity: 1- full commercial ray tracing; 2- simplified geometric model; 3- Markov chain model of Chapter 3; or 4- the newly proposed sum of Markov chains model. Although the performance of the first option is most realistic, where all the possible rays between the BS-RX are considered, the high complexity and time-required do not make it the preferred option, so it is out of this chapter's scope. In this section, the simplified geometric and Markov chain models are introduced. They will be used for comparison later in this chapter with the novel sum of Markov chains model, which is presented in the next section, Section 4.5. Two tasks are required for each model, the first is to determine the average number of blockers of a given environment, and secondly to compute the resulting

attenuation. These results, finally, are considered in the received power calculations (4.8) to obtain the overall channel capacity results (4.9) for each model.

4.4.1 The Geometric Model

4.4.1.1 The Average Number of Blockers

Modelling blockage using a simplified geometric model comes with adequate performance and moderate complexity. The key factor that changes the average number of blockers is the number of blockers that cross the LOS path. However, this number increases with the BS-MT distance as in (4.3). As stated in [154], the longer the path, the more blockers would block it on average. The geometric model used in this chapter was created in MATLAB for three different scenarios to represent different environments, as shown in Fig. 4.5.

In each scenario, the mobile transceiver (MT) would move around the BS following a different receiver trajectory: circular, straight-line and sinusoidal shape. It is important to emphasize that the average number of blockers is not affected by the trajectory itself, but by the BS-MT distance. As explained in Section 4.5, N equally spaced sample points are laid along these tracks. Once the MT starts moving and comes across each sample point, the number of blockers that block the LOS path between the mobile transceiver and the BS are computed using ray optics and stored in a vector with dimension N which is completed once the MT reaches the last sample point along the track at sample time t_N . Running the simulation repeatedly with M Monte Carlo runs results in an $M \times N$ average number of blockers matrix, which contains the number of effective blockers at each sample points.

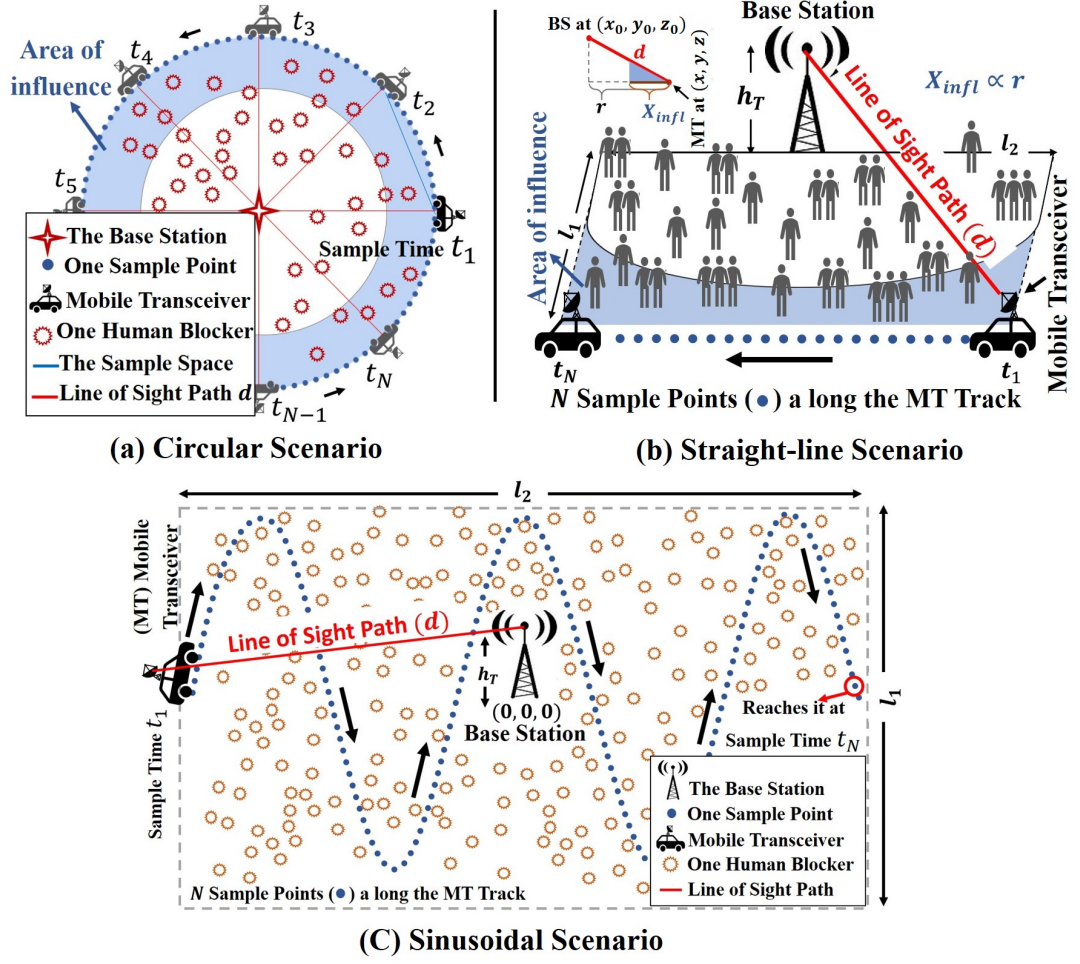


Figure 4.5: Scenarios of the Geometric Model.

The receiver's track scenarios as follows:

1. **Circular-shape Scenario:** In this scenario, the BS is in the centre of a circle and the receiver track follows the circle circumference as in Fig. 4.5 (a). The purpose of having a circular track, where the distance to the base station is the same, r , is to keep the same average number of blockers at all sample locations, i.e. the average number of blockers in (4.3) will be $N'_G = K_1$ where K_1 is a constant. This is a statistically stationary scenario.
2. **Straight-line shape Scenario:** In this scenario, there is a mobile transceiver that is moving along a straight track and passing by the base station, as shown in Fig.

4.5 (b). Unlike the previous scenario, the average number of blockers here varies as the MT moves along the track based on the BS-MT distance; i.e. the average number of blockers in (4.3) will be $N'_G = K_2 \times X_{infl}$ where K_2 is a constant and X_{infl} varies along the track and obtained using (4.2).

3. **Sinusoidal-shape Scenario:** The receiver track here has a sinusoidal shape as in Fig. 4.5 (c), which is more complicated than the previous two cases, and it causes the average number of blockers to change with the MT location. In real-world scenarios, the MT could move around the BS at any distance and in any direction, so the BS-MT distance will keep changing. A good way to capture such fluctuations in simulation is to use a sinusoidal-shape scenario where the BS-MT distance keeps changing.

4.4.1.2 Blockage Attenuation

As mentioned in the previous section; two approaches to compute blockage attenuations are considered. First, when each human blocker causes a 20 dB fixed attenuation value, the overall resulting attenuation along the MT track is computed by multiplying the number of blockers by 20 dB. However, for 3GPP blockage approach, each blocker in the geometric model will be treated separately. As explained in Section 4.3.2, at any sample point, whenever the LOS path intersects with a blocker, equation (4.10) is applied to calculate the attenuation value at this point.

4.4.1.3 Complexity Order of the Geometric Model

Assume that an MT moves around a BS within an area A_T . There are N_{BL} blockers within this area and N sample points. At each sample point, first, we need to check whether any one of the N_{BL} blockers crosses the LOS path. Then, if K blockers do cross the LOS path, we need to compute the 3GPP blockage attenuation equation for each blocker. For simplicity, we define the complexity of the 3GPP equation as requiring G operations. To carry out a Monte Carlo simulation, the model should be

run M times. Thus, the complexity order is as follows:

$$\mathcal{O}(NN_{BL}MKG) \quad (4.12)$$

4.4.2 Markov Chain Model

As proposed in Chapter 3, the average number of blockers surrounding a moving transceiver could be captured using a Markov chain model with sufficient states to represent all possible numbers of blockers that could be expected. Each state represents the case where a specified number of blockers intersect the LOS path. The transition probability, P_{jk} , from state j to state k is defined by:

$$P_{jk} = \frac{n_{jk}}{\sum_{l=1}^m n_{jl}} \quad (4.13)$$

where n_{jk} is the number of times the average number of blockers changes from state j to state k along the track and m is the number of possible states. These transition probabilities between these states are obtained from running the geometric model offline and these probabilities are the only input needed for the Markov chain model for a given environment.

The Markov chain model works very well in a stationary scenario where the average number of blockers remains at the same level as in a circular-track scenario. For non-stationary scenarios, a single Markov chain can not model the change in the average number of blockers. In Chapter 3, we proposed a solution by dividing the receiver track into several sectors and representing each sector with a different Markov chain based on a different transition probability matrix.

However, the limitations for this simplified Markov chain model, presented in Section 4.1.1, have led us to propose a more advanced Markov chain model that overcomes all the limitations and yet retains the efficiency and simplicity of the Markov chain model. This is presented in the following section.

4.5 Sum of Markov Chains Model

4.5.1 Introducing the model

The sum of Markov chains model can capture the average number of blockers surrounding a moving vehicle in a very efficient way using only basic knowledge about the surrounding environment. The fundamental idea of the model is as follows: having several Markov chains in parallel with a very limited number of states will successfully capture the average number of blockers for any given receiver track. The sum of Markov chains model is based on the Binomial distribution, and it is constructed from several n chains in parallel, where each chain has only two states: state S_0 , i.e. a clear LOS path, and state S_1 , i.e. blocked by one blocker. The LOS path status converts from S_0 to S_1 using the probability P_{01} . Then, it remains in this state for l_B sample points until the mobile transceiver passes this blocker. Once this condition is met, it switches back to S_0 , as shown in Fig. 4.6.

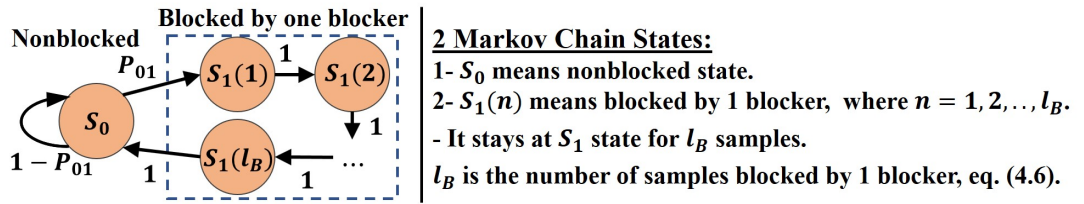


Figure 4.6: Two Markov Chain Model states for one chain of the sum of MC.

The diagram in Fig. 4.7 explains the sum of Markov chains model process. Each chain is treated as an independent event and has no impact on any other chain (i.e. independent probabilities). Moreover, the values of the probabilities, P_{01} is the same across all parallel chains. By making the right choice of P_{01} with enough number of chains, the sum of Markov chains model will be able to predict an accurate value for the average number of blockers N'_S for a given environment.

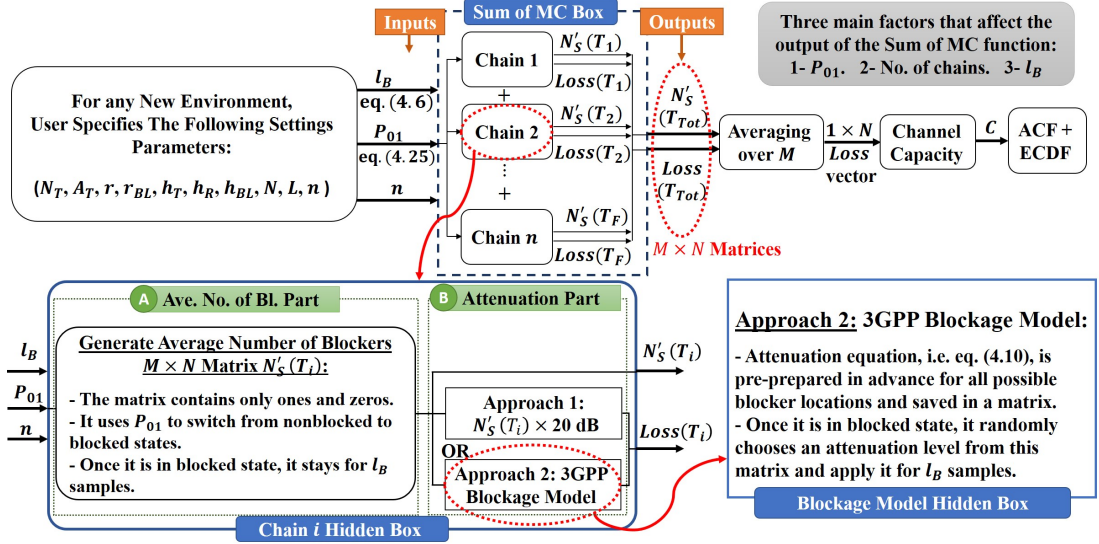


Figure 4.7: Diagram explains the process of the sum of Markov Chains Model.

The main advantage of the sum of Markov chains model is its ability to work successfully with any receiver track scenario, whether it is stationary or non-stationary. For each chain in non-stationary scenarios, such as straight-line and sinusoidal, the input probability P_{01} will vary along the track so it is able to produce the required average number of blockers. Before we provide a numerical example of updating the transition probability, we first need to define the transition probability P_{01} in the next section. The numerical example is provided in Section 4.6.2.

The average number of blockers of the sum of Markov chains for a given environment can be obtained using two different approaches: analytically and by simulation.

4.5.2 Analytical Calculation of Average Number of Blockers

This approach aims to obtain N'_S analytically from the input transition probability P_{01} . This can be done through several steps: first, the input transition probability needs to be modified. After that, we obtain the probability of a sample point along the chain being blocked by one blocker P_B . Then, the last step before computing the average number of blockers is to obtain the probabilities of having k blockers in a row.

4.5.2.1 The Transition Probability P_{01}

In the Markov chain model, presented in Chapter 3, the transition probability from state 0 (non-blocked state) to state 1 (blocked by one blocker) is:

$$P_{01} = \frac{\text{Number of Blockers}}{\text{Number of Sample Points}} \quad (4.14)$$

This definition is only applicable when the size of the blocker is small enough that it can block only one sample point at a time. However, in most practical cases, a blocker's shadow, as in Fig. 4.1 (b), will cover several sample points, l_B , especially when the sample space between these points is quite small compared to the size of the blocker. Therefore, we need to redefine the transition probability and make it applicable to any blocker size and any sample space.

To modify (4.14), we split the sample points into two categories: blocked samples and non-blocked samples. Assuming all blockers have the same size, the total number of blocked samples is the number of samples blocked by one blocker multiplied by the total number of blockers. The total number of non-blocked samples is computed similarly. Now, the modified transition probability, denoted as P_S , can be written as follows:

$$P_S = \frac{\text{No. of Blockers}}{\text{No. of Blockers} \times (l_{NB} + l_B)} \Rightarrow P_S = \frac{1}{(l_{NB} + l_B)} \quad (4.15)$$

where the scalar l_B is the number of sample points that are shadowed by one blocker, which can be computed using (4.6). The scalar l_{NB} is the number of non-blocked samples before each blocker, and it is obtained from the ratio between the two transition probabilities that comes out of non-blocked state, as in Fig. 4.6, which is written as follows:

$$l_{NB} = \frac{1 - P_{01}}{P_{01}} \quad (\text{Sample Points}) \quad (4.16)$$

Now, we need to rewrite the modified transition probability P_S as a function of the original transition probability P_{01} , since P_{01} is still the main input. This is obtained by

inserting (4.16) into (4.15) as follows:

$$P_S = \left(\frac{1 - P_{01}}{P_{01}} + l_B \right)^{-1} = \left(\frac{1}{P_{01}} - 1 + l_B \right)^{-1} \quad (4.17)$$

Having the modified transition probability in hand, now we can continue to calculate the average number of blockers N'_S .

4.5.2.2 The Probability of being Blocked P_B

In each chain in the sum of Markov chains model, the probability of a sample point being blocked by one blocker, P_B , is calculated as:

$$P_B = l_B P_S = l_B \left(\frac{1}{P_{01}} - 1 + l_B \right)^{-1} \quad (4.18)$$

4.5.2.3 The Probabilities of Having k Blockers in a Row

Adding n two-state chains in parallel will result in 2^n outcomes that produce $(n + 1)$ possible blockers in the range from $k = 0$ up to n blockers. The probability of having k blockers in a row is expressed as:

$$P_k = (P_B)^k (1 - P_B)^{n-k} {}^n C_k \quad (4.19)$$

where ${}^n C_k$ is the Binomial coefficient. Summing the probabilities for all k should equal one.

4.5.2.4 Average Number of Blockers N'_S

The average number of blockers of the sum of Markov chains model is simply the mean of the Binomial distribution, and it is defined as follows:

$$N'_S = \mathbb{E}(K) = \sum_{k=0}^{k=n} k P_k = \sum_{k=0}^{k=n} k \binom{n}{k} P_B^k (1 - P_B)^{n-k} \quad (4.20)$$

Using the well-known closed form of the Binomial distribution, the average number of blockers could be simplified further in the following few steps [155]; by first changing the summation limits to $y = k - 1 \Rightarrow k = y + 1$ and $m = n - 1 \Rightarrow n = m + 1$:

$$N'_S = \sum_{k=0}^{k=n} k \frac{n!}{k!(n-k)!} P_B^k (1 - P_B)^{n-k} \Rightarrow \sum_{y=0}^{y=m} \frac{(m+1)!}{y!(m-y)!} P_B^{y+1} (1 - P_B)^{m-y} \quad (4.21)$$

Then, substituting the new values would give the following:

$$N'_S = (m+1)P_B \sum_{y=0}^{y=m} \frac{m!}{y!(m-y)!} P_B^y (1 - P_B)^{m-y} \quad (4.22)$$

From Binomial theory, we know that the second part of the equation equals to one as follows:

$$\sum_{y=0}^{y=m} \frac{m!}{y!(m-y)!} (1 - P_B)^{m-y} = (P_B + (1 - P_B))^m = 1 \quad (4.23)$$

Then, finally, the average number of blockers of the sum of Markov chains model is:

$$N'_S = nP_B = nl_B \left(\frac{1}{P_{01}} - 1 + l_B \right)^{-1} \quad (4.24)$$

In principle, the average number of blockers in (4.24) and (4.3) should be equal, i.e. $N'_S \simeq N'_G$. The variable l_B is the average number of sample points that is affected by one blocker, which is obtained in (4.6). The transition probability P_{01} is the main input for the above function, which means each value of P_{01} will produce a corresponding average number of blockers, N'_S . To make the model adaptive to any scenario, we update the probability P_{01} at each sample point, based on how far the MT sample point is from the BS. We will have P_{01} vector of length N . Thus, from (4.24) we can define the optimal transition probability that leads to the desired average number of blockers as follows:

$$P_{01} = \left(\frac{nl_B}{N'_G} + 1 - l_B \right)^{-1} \quad (4.25)$$

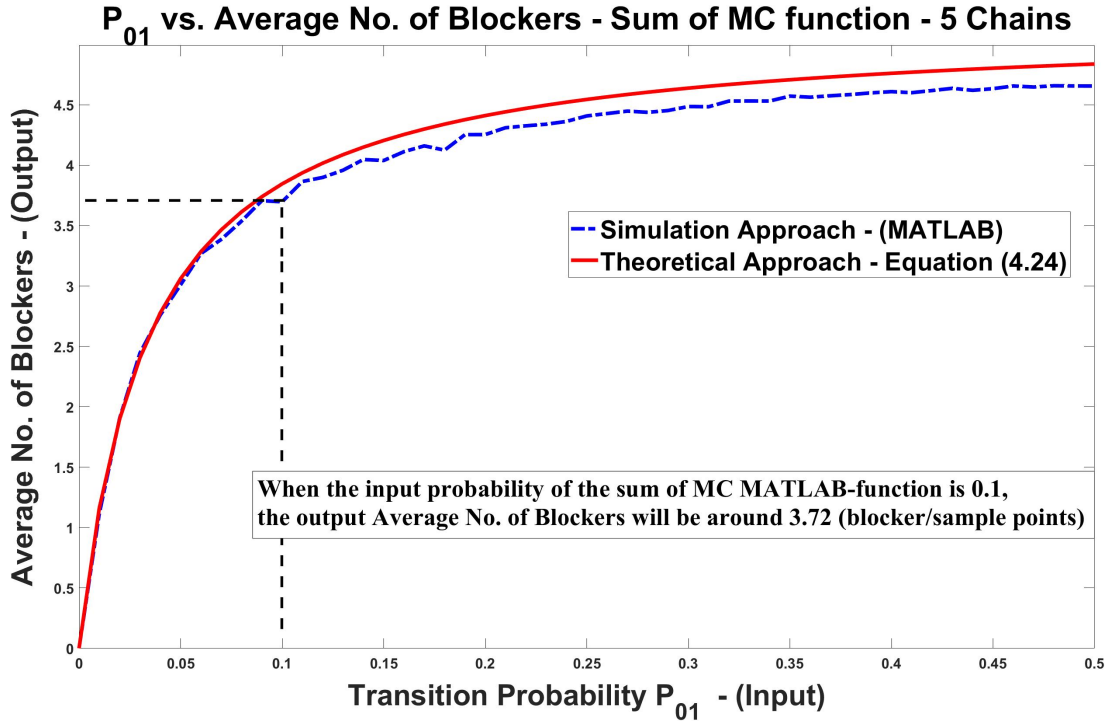


Figure 4.8: The relationship's curve between the input P_{01} and the output N'_S of the sum of Markov chains function, where $l_B = 30$ and $n = 5$.

4.5.3 Average Number of Blockers by Simulation

A MATLAB function was created that takes the transition probability P_{01} as an input and give the average number of blockers of the sum of Markov chains model as an output as shown in Fig. 4.7. To understand the relationship between the input P_{01} and the output N'_S of the sum of Markov chains function, we plotted the probability versus the output average number of blockers N'_S in Fig. 4.8. Note, due to the sparse distribution of blockers, there is no need for very high values of the transition probability. This curve is a result of combining five chains. Fig. 4.8 could be used as a lookup table and guidance for the sum of Markov chains function.

4.5.4 Blockage Attenuation

As explained in Section 4.3, two approaches are considered for blockage attenuation as presented in Fig.4.7. For the fixed-attenuation scenario, whenever there is a human blocker, a 20 dB loss is added. As noted in Section 4.2.1, the attenuation of the model is simply computed by multiplying the number of blockers by 20 dB, e.g. if the LOS path blocked by 2 blockers, the resulting attenuation is 20 dB + 20 dB = 40 dB. The second approach is the 3GPP blockage scenario. To avoid computation at each time we run the sum of Markov chains function, the attenuation equation (4.10) of the 3GPP blockage model is computed in advance for all possible locations along the direct line between BS and MT and saved as attenuation levels in a lookup table within a hidden MATLAB function. Thus, at any chain of the sum of Markov chains model, whenever the signal status changes to a blocked state, the hidden MATLAB function will choose randomly one of the attenuation levels and apply it; then, keep it running for l_B sample points until the status switches back to the non-blocked state. However, the sum of Markov chains model can equally be applied to any other blockage model, which can be easily used instead of the 3GPP blockage model.

The next step entails inserting these attenuation losses into the calculation of the received power. Then, the overall average channel capacity for this model is computed using (4.9).

4.5.5 Complexity Order of the Adaptive Sum of MC Model:

The 3GPP blockage model here is computed offline for all possible locations, as mentioned in the above subsection, so it will not introduce any further complexity to the sum of the MC model. Likewise, the transition probability P_{01} vector is computed offline as well. The complexity order of the sum of MC model is as follows:

$$\mathcal{O}(nNM) \tag{4.26}$$

where n is the number of chains which is usually a small number, e.g. for all our scenarios, $n \leq 5$. The variables N and M are the number of sample points, and the

number of Monte Carlo runs respectively. Thus, it is obvious that the proposed sum of Markov chains model is significantly less complex than the geometric model, i.e. (4.12).

4.6 Results and Discussions

All the three models – geometric, Markov chain and the sum of Markov chains- aim to capture the dynamic of the blockers and to investigate the effect of the resulting attenuation on the LOS link in mmWave communication systems. The proposed sum of MC model is computationally efficient. For instance, in the sinusoidal-shape track, which is a complicated non-stationary scenario, we observe that the run-time of the sum of MC model is 7000 times less than the run-time of the geometric model. In this section, the overall average channel capacity (4.9) along the receiver track is key to the comparison between the models. Moreover, the autocorrelation function (ACF) in (4.27) and the empirical cumulative distribution function (ECDF) in (4.28) of the average capacity $C(t)$ are used as comparison metrics.

$$\text{ACF}(\Delta t) = \mathbb{E}[C(t)C(t + \Delta t)] \quad (4.27)$$

$$\text{ECDF}(c(t)) = P(C \leq c(t)) \quad (4.28)$$

Table 4.1 specifies all the parameters used in the simulation scenarios. In the following subsections, the results of all the three models – geometric, Markov chain and the sum of Markov chains – are presented based on the receiver track scenarios; i.e. stationary scenario (circular-shape track), non-stationary scenarios (straight-line and sinusoidal-shape tracks). Moreover, to show how the sum of MC model can apply any attenuation function, the results of integrating the attenuation profile of the lab measurements, see Section 4.3.3, is presented in the last subsection of the discussion.

General Settings			
BS Power	$P_T(Total) = 1 \text{ W}$	BS height	$h_T = 2.5 \text{ m}$
Noise Power	$N_O = -123.91 \text{ dB}$	MT height	$h_R = 1.5 \text{ m}$
Bandwidth	100 MHz	Blocker dimension	$r_{BL} = 0.235$ [87] $h_{BL} = 1.8 \text{ (m)}$
Carrier Freq.	$f_c = 30 \text{ GHz}$	D_T, D_R in (4.7) & (4.8)	8 Dipole antennas
The Circular Scenario		The Straight-line Scenario	
Sample points	$N = 360$	No. of Sample (points & space)	$N = 34001, \lambda/2$
No. of runs	$M = 100$	No. of runs	$M = 100$
Total No. of BL	(10, 50, 100, 200, 500)	Total No. of BL	$N_{BL} = 130$
Circle radius r	(10, 15, 20, 25, 30)m	A_T dim. (m)	$l_1 = 15, l_2 = 170$
The Sinusoidal Scenario		RF Lab Settings	
Sample points	$N = 500$	BS Power	$P_T(Total) = 1 \text{ W}$
No. of runs	$M = 500$	Carrier Frequency	$f_c = 28 \text{ GHz}$
Total No. of BL	$N_{BL} = 200$	BS, MT (Height) and BS-MT Distance	$h_T = 1, h_R = 1 \text{ (m)}$ $r = 2 \text{ (m)}$
A_T dim. (m)	$l_1 = 16, l_2 = 24$	Blocker dimension	$l_{B1} = 0.36 \text{ (m)}$ $l_{B2} = 0.282 \text{ (m)}$

Table 4.1: System and Antenna Parameters

4.6.1 Stationary Scenario: Circular-track Comparisons

The results of the stationary circular-track scenario, see in Fig. 4.5 (a) in subsection 4.4.1.1-(a), are presented based on the type of the blocker; i.e. fixed attenuation blocker or 3GPP blocker.

4.6.1.1 Fixed Attenuation Blocker Results

In the case of the fixed attenuation blocker, see Section 4.3.1, there is no need to compute the attenuation value caused by each blocker separately, so the MC model works here with no problem. Thus, both the Markov chain and the sum of Markov chains models work very well, and they match well with the geometric model.

Table 4.2 shows the overall channel capacity comparison of two circular shape sce-

narios, both with the fixed attenuation blockage model. The first scenario shows that by fixing the whole area and increasing the number of blockers within this area, the overall channel capacity drop. Both Markov chain and the sum of MC models work very well when compared with the geometric model. For instance, the difference in the capacity results of the two models compared with the geometric one is only 0.01 (bits/s/Hz) when the number of existing blockers is 10. The models yield equally close results for 100 blockers.

The Overall Average Capacity Along all the Circle Track (bits/s/Hz) & Average Number of Blockers (BL) N'									
Circle Scenario 1 (Vary No. of Blockers & Fixed Circle Radius) - Circle Radius is $r=10$ (m), 360 Sample Points									
N_{BL} Total No. of BL in the Area	1) Geometric Model		2) MC Model		3) Sum of MC Model				
	Channel Capacity	Average No. of BL N'	Channel Capacity	Average No. of BL N'	Channel Capacity	Average No. of BL N'	No. of MC Chains	P_{01}	l_B No. of blocked samples by one BL
10	13.67	0.037	13.68	0.036	13.66	0.038	1	0.01	4
50	12.7	0.188	12.69	0.189	12.72	0.184	2	0.025	4
100	11.51	0.37	11.52	0.369	11.53	0.367	4	0.025	4
200	9.1	0.738	8.99	0.755	9.24	0.717	5	0.042	4
500	2.17	1.848	2.13	1.855	2.26	1.832	5	0.144	4
Circle Scenario 2 (Fixed No. of BL & Vary Radius) - No. of BL in the Area is $N_{BL} = 200$, 360 Sample Points									
Radius r (m)	1) Geometric Model		2) MC Model		3) Sum of MC Model				
	Channel Capacity	Average No. of BL N'	Channel Capacity	Average No. of BL N'	Channel Capacity	Average No. of BL N'	No. of MC Chains	P_{01}	l_B No. of blocked samples by one BL
10	9.1	0.738	8.99	0.755	9.24	0.717	5	0.042	4
15	9.54	0.492	9.58	0.487	9.46	0.504	4	0.048	3
20	9.58	0.361	9.62	0.355	9.57	0.363	3	0.068	2
25	9.4	0.287	9.41	0.288	9.42	0.287	2	0.085	2
30	9.21	0.237	9.24	0.233	9.20	0.238	1	0.155	2

Table 4.2: Overall Channel Capacity C & Average Number of Blockers N' comparison between the three models: 1) Geometric, 2) Markov chain (MC) model, and 3) sum of Markov chains (sum of MC) - Two Circular Shape Scenarios both with Fixed Attenuation Blockage Model

The second part of Table 4.2 shows the capacity comparison as well, but here the total number of blockers is fixed, i.e. 200, and the BS-MT distance r , varies. The capacity

results of both MC and sum of MC models match the geometric results very well with very small errors. For example, when $r = 30$ m, the capacity result of the sum of MC is only 0.01 (bits/s/Hz) higher than the geometric while the capacity result of the MC is only 0.03 (bits/s/Hz) higher.

The three models; geometric, Markov chain, and the sum of Markov chains; can be compared by the average number of blockers they produce. Table 4.3 shows the histogram by a percentage of the number of blockers (BL) that intersect with the LOS path of each model. All models show a good match with each other in the overall average number of blockers with only slight variations. The small MSE value of 0.19 between the histogram of geometric and sum of MC models reflects the accuracy of the sum of MC model in capturing the average number of blockers. One of the advantages of the sum of Markov chains over the Markov chain is that the average number of blockers can be mathematically found easily using (4.24), which has a very good match with the simulation results, as shown in Table 4.3.

Percentage of the Histogram of Average Number of Blockers %								Average	Reference	
Blockage Model Name & Approach		No. of BL intersecting with LOS path						MSE vs. Geom.	No. of BL N'	Section of The Chapter
		0	1	2	3	4	5			
(1) Geom.	Theoretical	43.68	39.35	14.18	2.55	0.23	0.00008	0.26	0.732	Sec.4.2 (4.3) & Sec.4.5.2 (4.19)
	Simulation	44.35	39.92	13.4	2.14	0.16	0.028	0	0.738	Sec. 4.4.1
(2) MC	Simulation	43.18	40.31	14.39	1.97	0.14	0.0056	0.42	0.755	Sec. 4.4.2
(3) Sum of MC	Theoretical	44.85	39	13.57	2.36	0.2	0.0071	0.19	0.74	Sec. 4.5.2 (4.19) & (4.24)
	Simulation	46.36	38.18	13.03	2.18	0.24	0.0056	1.2	0.71	4.5.3

Table 4.3: The average number of blockers N' comparison between all three models: 1) Geometric (simulation and theoretically), 2) Markov chain model, and 3) the sum of Markov chains (simulation and theoretically) - Fixed attenuation blockage model

Fig. 4.9 and Fig. 4.10 respectively show the average ACF and the ECDF of the channel capacity. Both Markov chain and the sum of Markov chains models work very well, and they match well with the geometric curve. Regarding the sum of Markov chains model, the sum of 5 chains was used to produce the required average number of blockers. The input value of P_{01} for the MATLAB function is 0.042, and it is fixed all over

the track. However, the desired average number of blockers can also be achieved, by a different number of summed chains, but that should be with the right choice of P_{01} . In Fig. 4.9, the average ACF of the capacity shows a better match with the geometric for the sum of Markov chains than the Markov chain model. However, Fig. 4.10 shows that both models match the geometric curve very well.

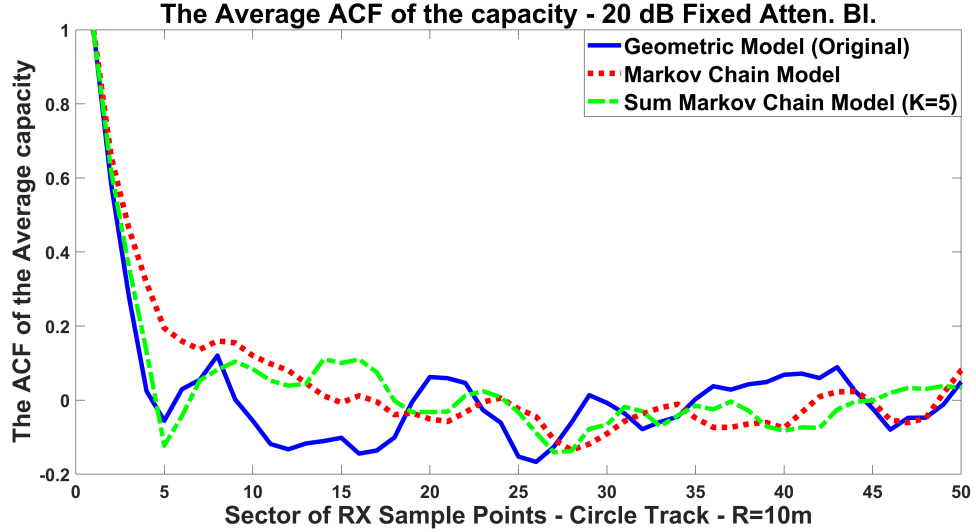


Figure 4.9: Average ACF of the Capacity of the circular track, $r=10$ m, with No. of BL=200, 360 sample points, and $M=100$ runs - Fixed Attenuation.

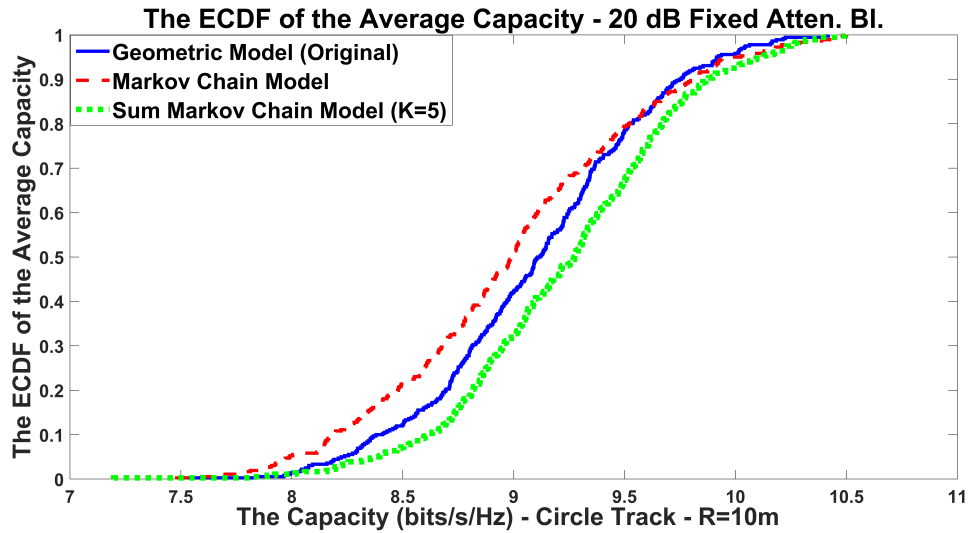


Figure 4.10: The ECDF of the Capacity of the circular track, $r=10$ m, with No. of BL=200, 360 sample points, and $M=100$ runs - Fixed Attenuation.

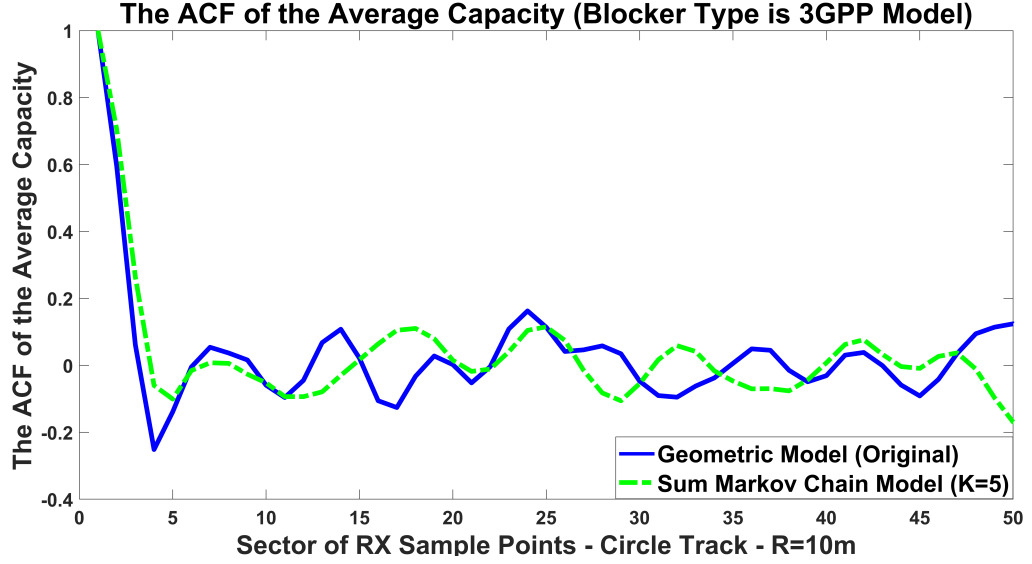


Figure 4.11: Average ACF of the Capacity of the circular track, $r=10$ m, with No. of BL=300, 360 sample points, and $M=500$ runs - 3GPP Blocker.

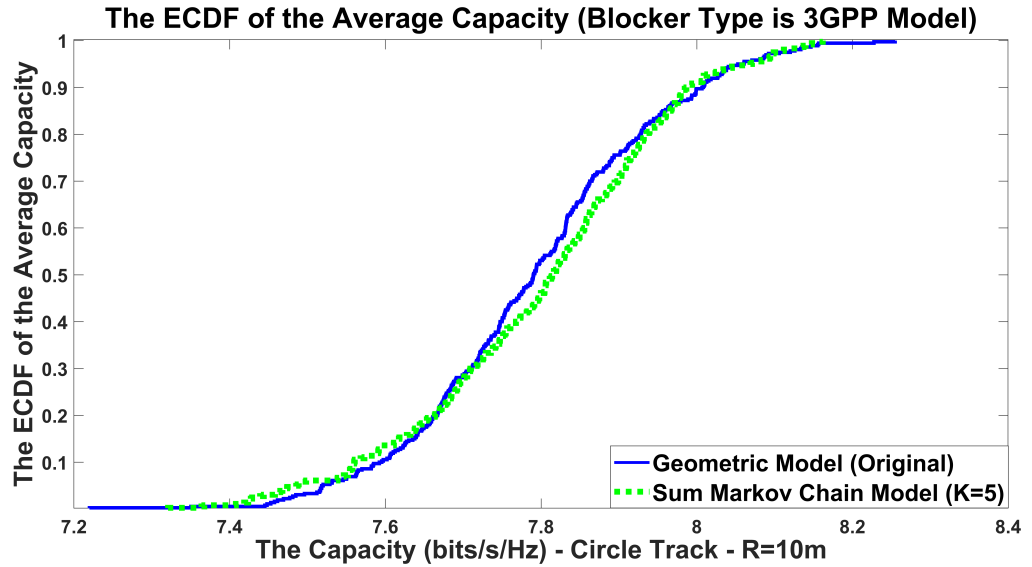


Figure 4.12: The ECDF of the Capacity of the circular track, $r=10$ m, with No. of BL=300, 360 sample points, and $M=500$ runs - 3GPP Blocker.

4.6.1.2 3GPP Blocker Results

It is more practical to use an attenuation value caused by a blocker model that varies based on the location and orientation of the blocker; such as the 3GPP blocker model in Section 4.3.2. The Markov chain model can not be easily modified to predict how

much attenuation is caused by each blocker. Here, one of the advantages of the sum of Markov chains emerges: it is flexible, and it can adopt any attenuation profile. As shown in Fig. 4.11 and Fig. 4.12, both the average ACF and ECDF of average capacity curves show that the performance of the sum of Markov chains model is as good as that of the geometric model.

4.6.2 Non-stationary Scenario Comparisons

The sum of Markov chains model has an adaptation feature that makes it applicable even to non-stationary scenarios such as straight-line and sinusoidal-shape tracks, where the average number of blockers is not constant. This advantage is obtained by updating the input value P_{01} over time based on how far the MT sample point is from the BS. The optimal P_{01} values across all positions along the MT track are obtained from (4.25) and used as an input of the sum of Markov's MATLAB function.

The following numerical example is to explain how we update P_{01} along the MT track. The idea is to get the advantage of knowing the theoretical value of N' , which is based on statistical knowledge of the surrounding environment as clear in (4.24). The two following scenarios are for the same environment, but we only change how BS-MT distance. First, let's assume that we have all the following information about the environment, which are the blockage density, the blocker size, and the height of BS, MT, and the blocker as follow: ($N_T = 130, A_T = 255, r_{BL} = 0.55, h_T = 2.5, h_R = 1.5, h_{BL} = 1.8, N = 34001, L = 170, n = 5$):

- First scenario: if the BS-MT distance is $r = 15$ m, then from (4.24), the theoretical value $N' = 0.25$. Based on this value and using (4.25), the optimal value of the transition probability $P_{01} = 1.9 \times 10^{-4}$.
- Second scenario: now let us assume that the MT moves far from the BS, i.e. $r = 26$ m. Then $N' = 1.45$. Based on this value and using (4.25), the optimal value of the transition probability $P_{01} = 0.0015$.

These optimal values are then used as an input to the Sum of MC function.

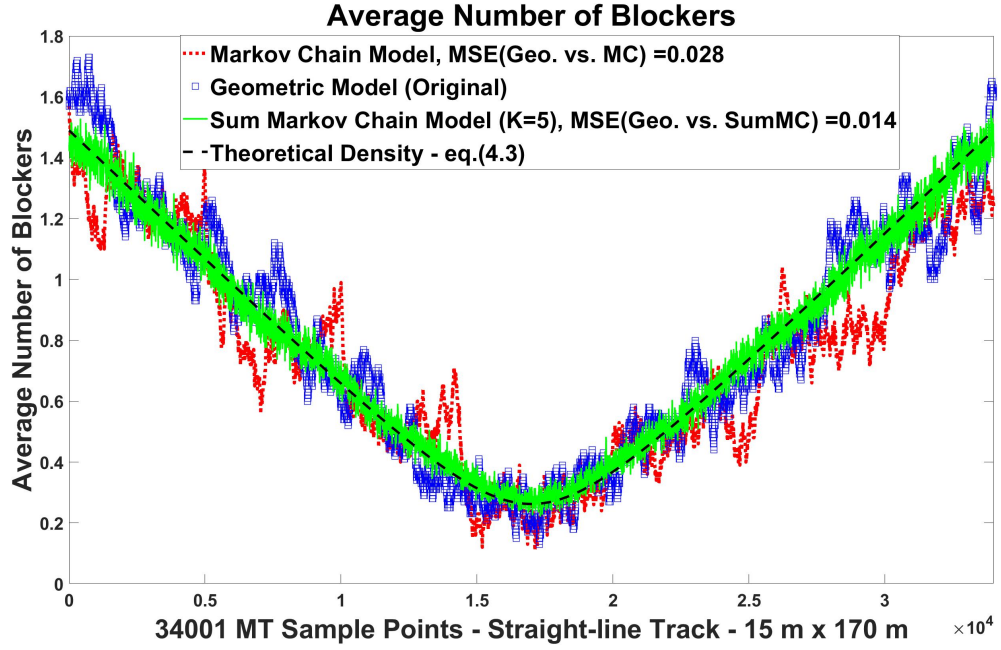


Figure 4.13: Average number of blockers along the MT straight-line track with No. of BL=130, $r_{BL} = 0.55$ m, 34001 MT sample points, sample space $\lambda/2$, and $M=100$ runs - Fixed Attenuation.

In this chapter, we have introduced two non-stationary scenarios:

4.6.2.1 Straight-line Scenario

As mentioned in Section 4.4.1.1-(b), in this scenario, the mobile transceiver is approaching and passing the BS. The track length, 170 m, is chosen to investigate the difference in the average number of blockers with distance. When it is far from the BS, it is more likely to suffer from more blockers blocking the LOS path, so N'_G in Fig. 4.13 starts high, then, it decreases until it reaches the minimum when the MT is very close to the BS. Then, it starts to rise again. The theoretical approach for computing the average number of blockers N'_G in (4.3) is matching the geometric-based simulation curve very well. Although the scenario is not stationary, the resulting N'_S curve of the sum of MC model in Fig. 4.13 matches the geometric curve very well. We used (4.25) to find the optimal transition probability vector P_{01} as input the sum of MC function. However, regarding the Markov chain model, i.e. the red curve, since the scenario is not stationary, it is required to have several chains based on multiple

probability transition matrices to obtain the MC results, as described in Chapter 3.

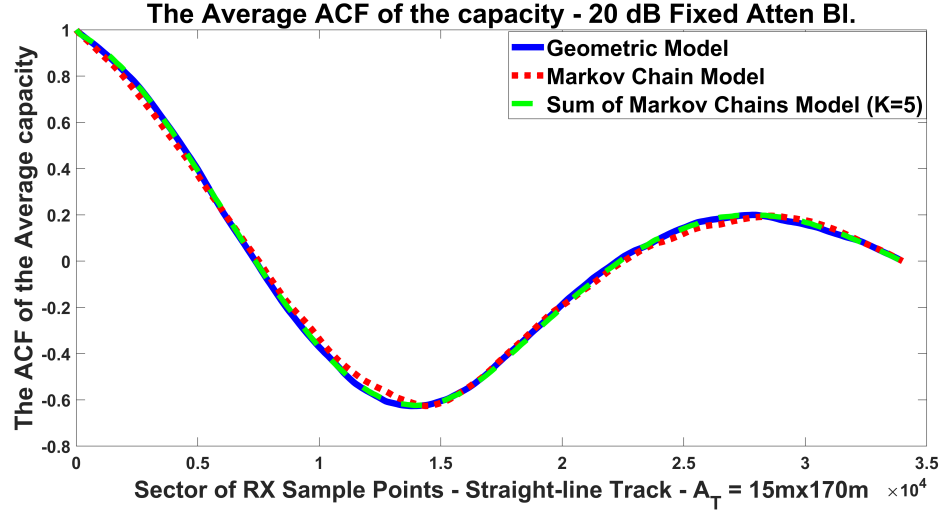


Figure 4.14: The Average ACF of the Capacity of the straight-line track with No. of BL=130, $r_{BL} = 0.55$ m, 34001 MT sample points, sample space $\lambda/2$, and $M=100$ runs - Fixed Attenuation.

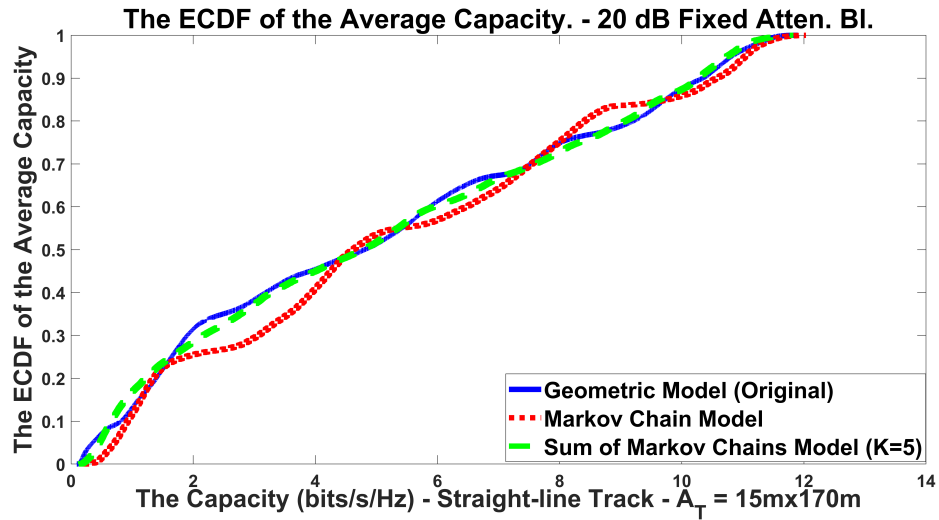


Figure 4.15: The ECDF of the Capacity of the straight-line track with No. of BL=130, $r_{BL} = 0.55$ m, 34001 MT sample points, sample space $\lambda/2$, and $M=100$ runs - Fixed Attenuation.

The average ACF curve of the sum of MC in Fig. 4.14 has a perfect match with the geometric curve. Both the sum of MC and the Markov chains curves match very well, but the sum of the MC curve has a slightly better performance. The ECDF of the

average channel capacity in Fig. 4.15 shows that although all models perform closely, the sum of MC curve fits better to the geometric curve than the Markov chain curve.

4.6.2.2 Sinusoidal Scenario

This sinusoidal-shape track is even more complicated than the straight-line scenario. As mentioned in subsection 4.4.1.1-(c), and as shown in Fig. 4.5 (c), the mobile transceiver is moving along a cosine track, while the BS is at the origin point. In this scenario, the distance between the BS and MT increases and decreases repeatedly, hence the average number of blockers fluctuates as well. This is a severe and quite complicated non-stationary case. By following the simulation approach mentioned in Section 4.5.3, the output N'_S of the sum of Markov chains function show a perfect fit with the geometric average number of blockers in Fig. 4.16. However, due to the complexity of the scenario, the Markov chain model fails to adapt even with the use of multiple sectors idea [17]. We have divided the track into 9 sectors which are based on only two Markov chains: one for the peaks and bottoms of the curve, and one for the straight lines.

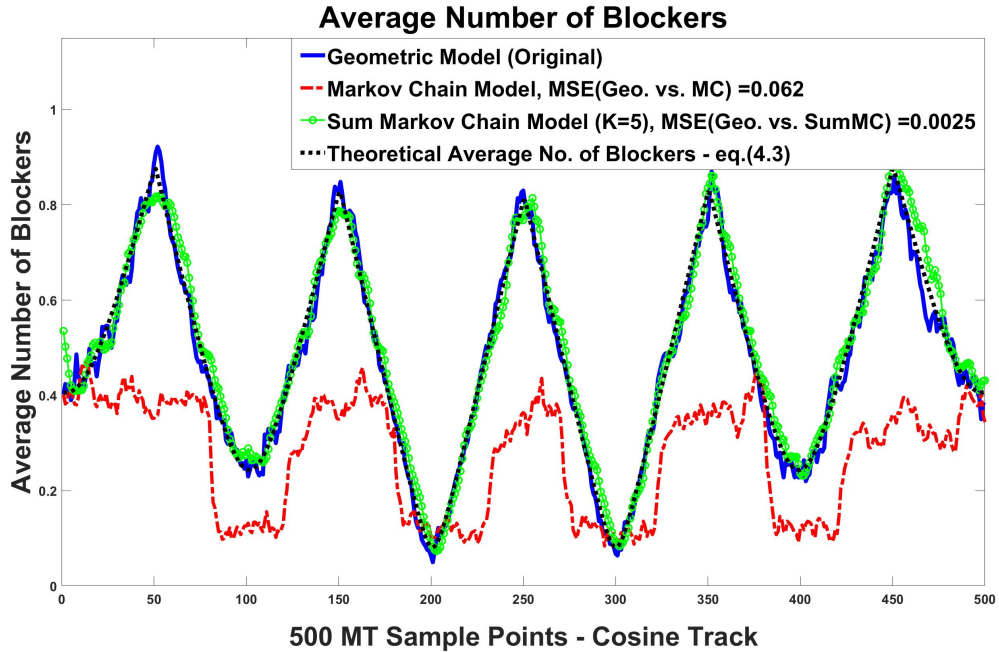


Figure 4.16: Average number of blockers along the MT Cosine-shape track with No. of BL=200, $r_{BL} = 0.2821$ m, 500 sample points, and $M=500$ runs - Fixed Attenuation.

Both ACF and ECDF channel capacity curves of the sum of Markov chains model, in Fig. 4.17 and Fig. 4.18 sequentially, are showing an identical match with the geometric curve. Although we use several chains for different segments, the Markov chain model fails to adapt to this severe case of non-stationary scenario, as is obvious from the results Fig. 4.18. These figures show the benefit of the proposed sum of Markov chains model.

Discussion: In a more general trajectory, three main factors that affect the average number of blockers: 1) The BS-MT distance. 2) The blocker width. 3) The heights of the BS, MT, and the blocker. The results show that the adaptive sum of MC model can successfully update the average number of blockers by adjusting the number of blockers based on the BS-MT distance through increasing or decreasing the number of chains n and the transition probabilities P_{01} .

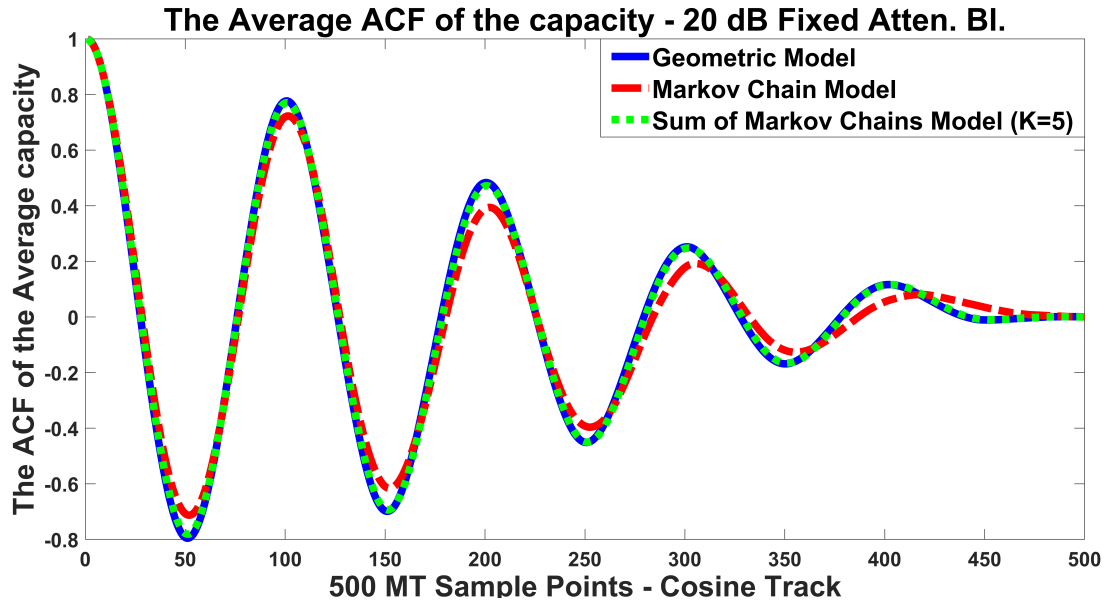


Figure 4.17: The Average ACF of the Capacity of the Cosine track with No. of BL=200, $r_{BL} = 0.2821$ m, 500 sample points, and $M=500$ runs - Fixed Attenuation.

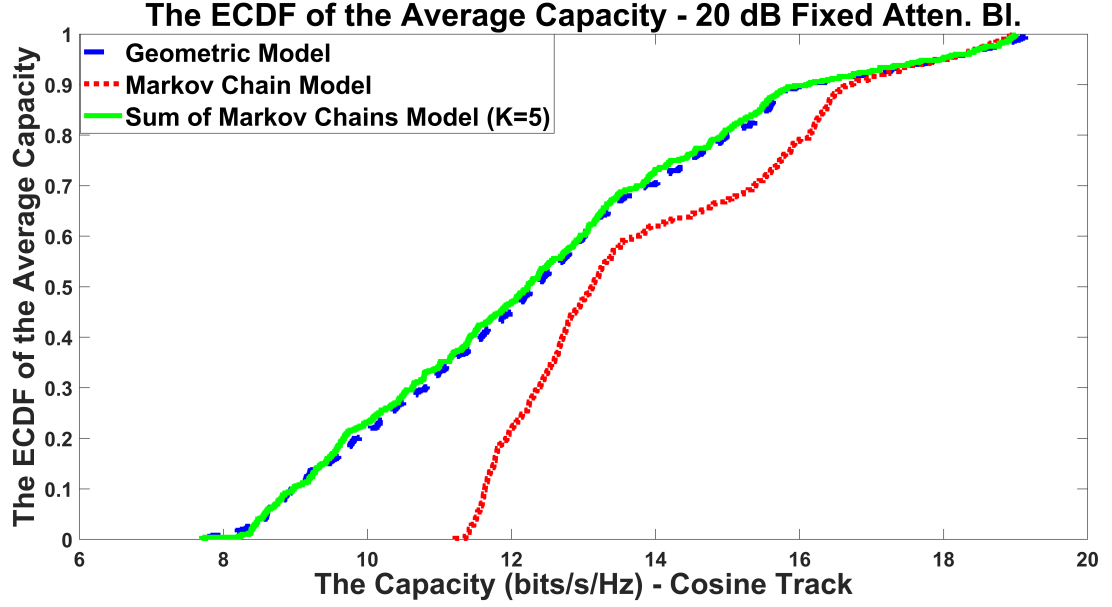


Figure 4.18: The ECDF of the Capacity of the Cosine track with No. of BL=200, $r_{BL} = 0.2821$ m, 500 sample points, and $M=500$ runs - Fixed Attenuation.

4.6.3 Results of Integrating Lab measurements into the Sum of MC Model

The novel sum of MC model can integrate any attenuation profile. Clearly, from the previous results in Section 4.6.1.2, it has adopted the 3GPP blockage model successfully. To test this feature furthermore, the attenuation profile of the copper sheet taken from the lab measurements, see Section 4.3.3, is integrated with the sum of MC function. To compare the results we have created a circular geometric model with the following parameters: ($r = 2$ m, blockers are placed 1 m from the BS i.e. in the middle, $r_{BL} = 0.14$, 4 copper-sheet blockers, $N = 360$ sample points, and $h_{BL} = h_R = h_T = 1$ m), which are similar to the lab settings in Table 4.1. Due to the blocker size and location, the number of blocked samples for one blocker is $l_B = 17$ samples. The resulting overall average of the channel capacity (4.9) of the sum of MC is $C = 17.67$ (bits/s/Hz), which is very close to the average channel capacity obtained from the geometric model $C = 17.85$ (bits/s/Hz). This accuracy and adaptation of any attenuation profile reflect the novelty of the proposed sum of MC model.

4.7 Conclusion

A novel sum of Markov chains model that successfully captures the dynamics of blockers surrounding a moving transceiver in both stationary and non-stationary scenarios is described. Compared with a baseline geometric model, both the sum of MC and Markov chains models are computationally efficient. We found that the run-time of the sum of MC is three orders of magnitude less than the geometric model for a severe non-stationary scenario. The proposed sum of MC model has further advantages, which overcome the drawbacks of the MC method. These are: 1) It is adaptive for any complex non-stationary scenario. 2) The ability to integrate any attenuation function; including the 3GPP blockage model, and any lab-measurement attenuation profile. 3) Unlike the MC model, the mathematical derivation of the average number of blockers can be found in closed form. All the average channel capacity results and the curves of both ECDF and ACF show good performance for the sum of MC compared with the geometric model. We believe that this computationally efficient sum of MC is valuable for evaluating high gain beam pattern techniques for directional mmWave communication systems. For future work, evaluating beam training algorithms with the proposed blockage model will be investigated. Moreover, instead of operating only on the direct LOS path, the sum of MC blockage model can easily be extended to apply to multi-path scenarios. Each path would be treated independently; unless there is a correlation between the paths. Although the proposed sum of MC model serves the V2I system, the model can also be modified to apply for more general models, such as vehicle-to-everything (V2X) systems.

From this chapter and the one before, we can see that human blockage has attracted the attention of various researchers, where intensive measurements and modelling have been undertaken. This raises a question about objects that are smaller than human bodies: will they have the same effect as human blockage? In Chapter 5, we investigate the effect of small-sized blockages. Chapter 3 and 4 considered only the LOS path for both cases (blocked and non-blocked); however, it is more practical to study the effect of multi-path scenarios in the presence of blockers as well, which is also investigated in Chapter 5.

4.8 Software

The MATLAB code used for the proposed sum of Markov chains model is available from the below link:

<https://datashare.is.ed.ac.uk/handle/10283/3657>

Chapter 5

Small-Size Blockage Propagation Modelling for mmWave Communications Systems

5.1 Introduction

Human and car blockages were considered in Chapter 3, while Chapter 4 focused on human blockage only. The short wavelength of the mmWave suggests that even small blockages could affect the mmWave signal strength. There is a lack of literature investigating the effect of small-sized blockages. Thus, the scope of this chapter is related to measurements and modelling for small-sized blockages. Unlike Chapter 3 and Chapter 4, where we consider only the LOS path (either blocked or non-blocked), this chapter also undertakes a comprehensive analysis of mmWave signal strength for a multi-path environment in the presence of blockers.

Sensitivity to blockage due to the very small wavelength of the mmWave frequency band is a critical drawback that has attracted researchers' attention [156]. Understanding the behaviour of the blockage effect, sometimes referred to as penetration loss, is important for the design of beamforming techniques for future mmWave systems [157–159]. The effect of a human blockage on the signal strength of mmWave communication systems has been thoroughly investigated by researchers in the past few years. Besides human blockages, some studies have investigated the loss caused by some indoor and outdoor objects. For instance, the authors of [160] measured the

Some work of this chapter is published in IEEE PIMRC, 2020 [18], and the whole work is submitted for publication in IEEE Transactions on Antennas and Propagation [19].

loss of a tree trunk and a cylindrical building pillar with diameters: 0.42 m and 0.36m, respectively; where the authors proposed a model named a shield edge diffraction to capture the measured loss. However, smaller blockage types, in the range of a few wavelengths, also play an important role, but their impacts on the signal in terms of power loss and distortion are less studied in the literature. The use of "*small object or blockage*" terminology, through this chapter, means much smaller than human bodies. Examples of outdoor blockage types include road signs, lampposts and traffic lights, while indoor blockage types include small pieces of furniture such as chairs, small tables, or a personal computer screen. Although several studies investigated the material penetration (blockage) losses of indoor and outdoor environments such as [161], the impact of small blockers still requires more investigation.

Most papers modelling blockages are based on one of three analytical approaches: the geometrical theory of diffraction (GTD) [145, 162]; the uniform theory of diffraction (UTD) [141, 163]; or knife-edge diffraction (KED) [5, 12, 13, 87, 88, 140, 164–166]. Based on a comparison made by different studies as [141, 145], all theories give similar results, but each approach has a different level of complexity, with KED being the simplest to implement [141], and is the focus of this chapter.

Four different approaches have been adopted by researchers to model blockage using the KED theory:

1. The first models were proposed by [164, 165]; these use one screen vertically oriented to the line of sight (LOS) path with a double knife-edge to model human blockage. Inspired by these studies, a few years later, the METIS channel models [12] proposed a model that used the same concept to capture the loss caused by the shadow of a blocker. Later, this model was adopted by the 3GPP standards body [5] as one of two simulation blockage models that can be applied to any blocker type.
2. Providing further improvements to the 3GPP model, NYU researchers in [87, 166] stated that the 3GPP blockage model underestimates the blockage attenuation when the transmit and receive antennas are directive. This is because the 3GPP blockage model is based on omnidirectional antennas. They found that

including directional antenna patterns of the antennas into the 3GPP loss equation improves the performance of the 3GPP model in capturing the measured attenuation.

3. The third approach is an extension of the same concept using the multiple knife-edge (MKE) model to simulate the human blockage by multiple screens accounting for the three-dimensional structure [13, 140].
4. The European Union H2020-5GPPP project mmMAGIC [88] proposed a blockage model that builds on the METIS model. They stated that the 3GPP KED model [5] underestimates the blockage loss since it does not consider the phase differences between the four diffracted paths around the blockage screen. Thus, they proposed a modified model that is claimed to be more accurate. It takes into account the fading effect resulting from the summation of the four diffracted paths.

Regarding the limitations of the 3GPP blockage model, the 3GPP standards body [5] stated that their KED simulation model could be used to model vehicle and human blockage effects. Reference [148] defined several conditions under which the double knife-edge model proposed by [167], which is similar to the 3GPP model, could be used to model human blockage. These rules included:

1. The electrical dimension of the blocker should be $w, h \geq 10\lambda$, where w and h are the width and the length of the rectangular screen respectively.
2. In the diffracted field, when $w, h \geq 10\lambda$, the polarization is not relevant.
3. The study shows that based on the electrical size of the antenna they used, the minimum distance between the blocker KED screen and the source is 15λ ; this could change with a different type of antenna.

A few studies have investigated the loss caused by some parts of the human body, such as the leg [162] and the arm [141]. References [168, 169] carried out measurements campaigns for hand blockage for user equipment at 28 GHz. Moreover, several studies,

such as [170, 171], have added another small KED blockage screen on the top of the main body screen to consider the head effect for more accurate modelling. This implies that blockage effects from even a relatively small object should not be ignored. The diameter of a human leg or arm is close to the diameter of the objects studied in this chapter, i.e. road signs, lampposts, and small metal furniture.

To the best of our knowledge, the loss caused by small blockers, i.e. relative to the size of a human, is not completely understood and requires more investigation. This chapter focuses on investigating the impact of small blockers in indoor and outdoor environments. We focus on different sizes of metal sheets and cylinders that are small relative to the human body. These small blockers introduce signal attenuation that cannot be neglected. As mentioned above, in the literature, there are four existing KED blockage models, which are: the 3GPP model [5], the version including directional antenna patterns [87], the MKE model [13], and the mmMAGIC model [88]. The first research question; would these models succeed in capturing the attenuation of small blockers? Second, how much small blockers could affect the mmWave signal? These will be investigated in this chapter.

The main contributions of this study are as follows:

- Providing mmWave measurements for different sizes of metal sheets and cylinders that are similar to those used for road signs, lampposts and small metal furniture.
- Investigating the applicability and the limitations of four state-of-the-art KED blockage models to assess which of these is most suitable for small blockers.
- To evaluate small-blockage effects on the received signal, we have inserted the measured attenuation profiles of small blockers into a designed outdoor environment using a ray-tracing tool. Also, we have evaluated the performance impact of a beam-switching technique to select the best available path.

These contributions shed light on how severely the small blockages can affect the mmWave received signal. This study provides a comprehensive understanding of the

behaviour of the channel attenuation resulting from blockers that are smaller than human bodies, which is necessary for forming reliable mmWave systems [107]. Also, it assesses the performance of the switching-beam technique for resolving blocked paths, which is an approach recognized by IEEE 802.15.3c [85, 86]

The remainder of the chapter is organized as follows: Section 5.2 presents the four blockage modelling approaches while Section 5.3 describes mmWave channel models using a ray-tracing tool. Section 5.4 introduces the measurement settings, and this is followed by the results and discussions in Section 5.5. Finally, the conclusions are presented in the last section, i.e. Section 5.6.

5.2 Blockage Modelling Approaches

In the presence of blockers, i.e. when the LOS is blocked, another term is included in Friis's free-space path loss equation [131] to become:

$$P_R = P_T P_L P_{BL} \quad (\text{W}) \quad (5.1)$$

where P_R and P_T are the received and the transmit power, while P_L and P_{BL} are negative gains in dB that represent the free space path loss, and the observed blockage shadowing loss.

In this study, we compare the measured attenuation resulting from relatively small blockers with these blockage models:

1. The 3GPP model (four-sided and two-sided) approaches.
2. the 3GPP version including directional antenna patterns.
3. The MKE model based on two 3GPP screens.
4. The mmMAGIC blockage model.

5.2.1 Model (1): 3GPP Blockage:

1. **Four Sided 3GPP Model:** each blocker is a rectangular screen with double knife-edge diffraction, as shown in Fig. 5.1 (a). The loss is computed using the four rays diffracted around the edges of the screen as follows [5]:

$$P_{BL} = -20 \log_{10} (1 - (F_{h1} + F_{h2})(F_{w1} + F_{w2})) \text{ (dB)} \quad (5.2)$$

where F_{h1} , F_{h2} , F_{w1} , and F_{w2} are the diffraction values associated with the four edges; h denotes the screen blocker height and w is the width, as shown in Fig. 5.1 (a). Every edge will cause shadowing equal to:

$$F = \frac{\text{atan} \left(\pm \frac{\pi}{2} \sqrt{\frac{\pi}{\lambda} (D_1 + D_2 - d)} \right)}{\pi} \quad (5.3)$$

where λ is the wavelength, D_1 and D_2 are the projected distance from the TX and RX nodes to the screen, and d is the projected distance between TX and RX nodes, as shown in Fig. 5.1 (a).

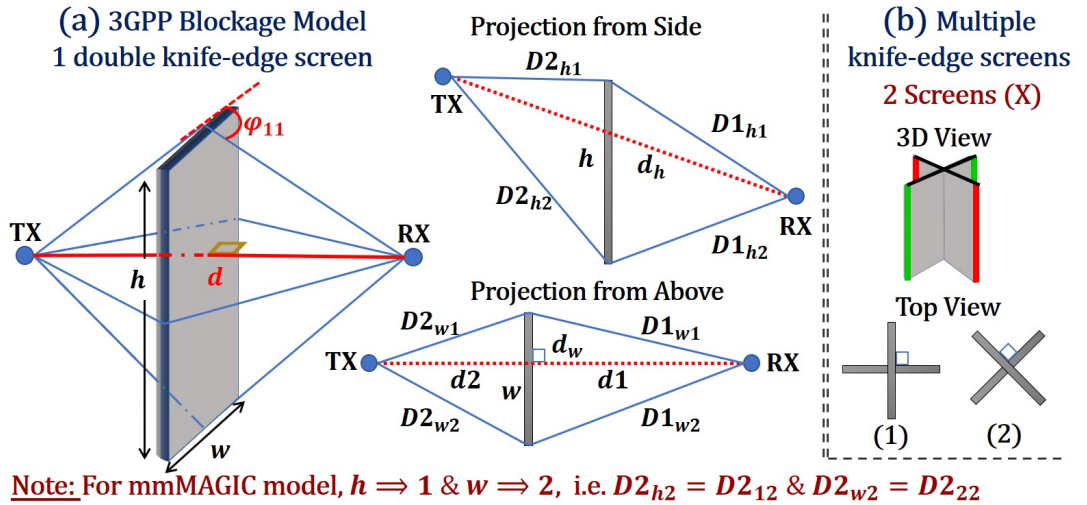


Figure 5.1: KED Shadowing screen model: (a) One screen blockage model [5] that represents the following models: 3GPP, 3GPP+antenna gain, and mmMAGIC. (b) Multiple KED screens [13] that represents the MKE model.

2. **Two Sided 3GPP Model:** several studies in the literature have neglected the top and bottom effect, assuming the screen height goes to infinity, i.e. $h \rightarrow \infty$. That is particularly relevant when the blocker-base touches the ground, as is the case for a human body [87]. Thus, (5.2) is modified as follows:

$$P_{BL} = -20 \log_{10} (1 - (F_{w1} + F_{w2})) \text{ (dB)} \quad (5.4)$$

In this study, the blockers are quite small in size. Therefore, the diffracted rays can easily travel above and under the blocker, we have studied both equations (5.2) and (5.4). We find that including all four values of the diffracted rays around all sides of the screen, i.e. the term $(F_{h1} + F_{h2})(F_{w1} + F_{w2})$ in (5.2), results in a reduced overall attenuation value than considering only the vertical edges, $(F_{w1} + F_{w2})$, i.e. (5.4). This can be justified by remembering that the value of $(F_{h1} + F_{h2})$ is less than one. Thus, when we multiply it by $(F_{w1} + F_{w2})$ in (5.2), this will result in a lower attenuation value from that equation.

5.2.2 Model (2): Including the Antenna Gain:

The 3GPP blockage model captures the blockage attenuation better when both antennas are omnidirectional [12]. When the directional antennas are used, the 3GPP blockage model underestimates the measured attenuation by more than 20 dB in the severe case when the blocker is close to one of the antennas, and with around a 10 dB difference in moderate cases [87]. The radiation pattern of the antenna would affect the measured blockage attenuation [172]. Thus, when directional antennas are used, the KED fields should be weighted by the corresponding linear antenna gain. The projected paths around the screen, i.e. $(D1_{W1}, D1_{W2}, D2_{W1}, D2_{W2})$ in Fig. 5.1 (a), should be weighted by the angle-dependent antenna gain [87]. Equation (5.2) is modified as follows:

$$P_{BL} = -20 \log_{10} \left| \left(\frac{1}{2} - F_{w1} \right) \cdot \sqrt{G_{D2_{w1}}} \cdot \sqrt{G_{D1_{w1}}} + \left(\frac{1}{2} - F_{w2} \right) \cdot \sqrt{G_{D2_{w2}}} \cdot \sqrt{G_{D1_{w2}}} \right| \text{ (dB)} \quad (5.5)$$

where G_x , ($x = D2_{w1}, D1_{w1}, D2_{w2}, D1_{w2}$), are the normalized linear gains of the directional antennas relative to the normalized boresight gain defined as $G(0) = 1$.

For the directional antenna, two cases are possible: 1- either the blocker completely blocks the main beam of the antenna, 2- the blocker partially blocks it. Let us define the variable W_{HPBW} in the following equation, which is the length of the intersection line between the main beam and the blocker screen, across from the angle of the half-power beamwidth (HPBW), as shown in Fig. 5.2.

$$W_{HPBW} = 2d_{1|2}\tan\left(\frac{\theta_{HPBW}}{2}\right) \quad (\text{m}) \quad (5.6)$$

The first case is when the blocker is in the farfield zone but still close enough that it can completely block the main beam, i.e. $W_{HPBW} \leq w$. Including the antenna gain would successfully improve the 3GPP model to fit the measured attenuation, as shown in Fig. 5 (subplot 1 and 9) in [87]. The second case is when the blocker partially blocks the antenna's main beam, i.e. $W_{HPBW} > w$ of the blocker. Including the antenna gain would only slightly improve the performance of the 3GPP model by around 2 or 3 dB, which is still far from the measured loss curve.

Our measurements described in Section III, below, fits better with case 2. Since 2 or 3 dB improvement is not enough, there is a need for an improved version of the 3GPP blockage model. That leads us to the MKE blockage model.

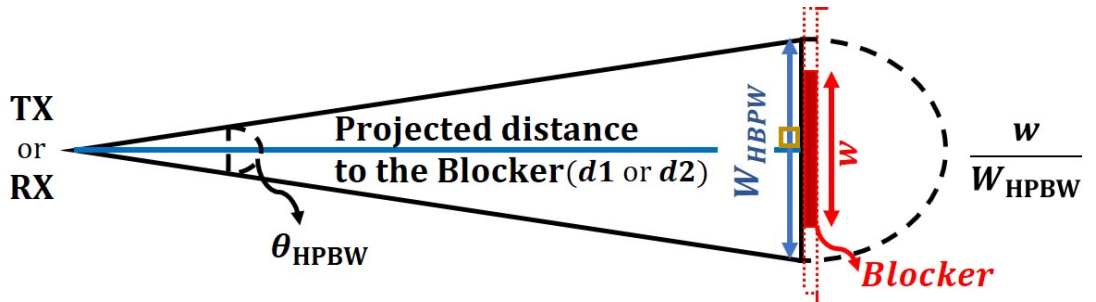


Figure 5.2: Cross-sectional view of the main antenna pattern and blocker.

5.2.3 Model (3): Multiple Knife-edge Diffraction (MKE):

Although some of the blockers in this chapter are metal sheets, they are not knife-edge sharp given the wavelength, $\lambda \approx 1 \text{ cm}|_{f_c=28 \text{ GHz}}$. That makes the blocker structure three dimensional. As stated on page 528 of [173], the actual attenuation with a rounded edge may be higher than the case of a very sharp knife-edge. That could justify the need for using the multiple knife-edge model for these blockers to resolve the gap between the actual measurements and the 3GPP blockage model. This approach uses the multiple knife-edge (MKE) diffraction model [13], where the blocker is represented by two perpendicular screens, as shown in Fig. 5.1 (b). Reference [13] considers only the screen with the highest attenuation, then, they add an extra attenuation to account for the human head. However, here the loss equation is as follows:

$$P_{BL} = \sum_{i=1}^K -20 \log_{10}(1 - (F_{w1}(i) + F_{w2}(i))) \quad (\text{dB}) \quad (5.7)$$

where K is the number of screens, i.e. $K = 2$ for the X-shape model, as shown in Fig. 5.1 (b).

Several factors play a major role in the resulting attenuation from the 3GPP blockage model. From (5.3), it is clear that the TX-RX distance, distance to the blockage screen, and the carrier frequency are the main factors in the equation. However, other hidden factors play important roles as well: the screen width and the screen orientation to the LOS path. Regarding the latter, several methodologies have been adopted by researchers. These factors are investigated in Section 5.5.

5.2.4 Model (4): The mmMAGIC Blockage Model:

As stated in [88], the 3GPP model [5] does not consider the phase variations between the diffracted paths. Thus, they still assume the blocker to be a rectangular thin screen, as in Fig. 5.1, but they have introduced and added some new parameters to the loss calculation equation to account for the phase variation. The calculation steps of the mmMAGIC model are the same as the 3GPP model, but they have added some new

parameters. These new parameters are: ph_{ij} , Ph and $\cos \varphi_{ij}$. For the mmMAGIC model, the loss is computed as follows:

$$P_{BL} = -20 \log_{10} \left(1 - \prod_{i=1}^2 \sum_{j=1}^2 s_{ij} \left[\frac{1}{2} - \frac{ph_{ij}}{Ph} F_{ij} \right] \right) \text{ (dB)} \quad (5.8)$$

where s_{ij} is the sign term, which is $s_{ij} = \text{sgn}(D1_{ij} + D2_{ij} - D1_{ik} - D2_{ik})$ if LOS, where $\text{sgn}(\cdot)$ is a function that specifies the sign of the argument. If NLOS, $s_{ij} = 1$. The scalar $k = \text{mod}(j, 2) + 1$. The remaining variables are defined as follows:

$$F_{ij} = \cos \varphi_{ij} \left[\frac{1}{2} - \frac{1}{\pi} \tan^{-1} \left(\frac{V_{ij}\pi}{2} \right) \right] \quad (5.9)$$

$$ph_{ij} = \exp \left[\frac{-j2\pi}{\lambda} (D1_{ij} + D2_{ij}) \right] \quad (5.10)$$

$$Ph = \exp \left[\frac{-j2\pi d}{\lambda} \right] \quad (5.11)$$

$$V_{ij} = \sqrt{\frac{\pi}{\lambda} (D1_{ij}^{\text{proj}} + D2_{ij}^{\text{proj}} - d_i^{\text{proj}})} \quad (5.12)$$

The variable $\cos \varphi_{ij}$ in (5.9) considers the increase of diffraction loss in the shadow zone behind the blockage screen. By assuming the values of the new parameters: ph_{ij} , Ph and $\cos \varphi_{ij}$ are one, we simplify to the 3GPP blockage loss equation, i.e. (5.2).

5.3 Modelling mmWave Channel with Ray-tracing

The ray-tracing tool has been proven to be effective in investigating the mmWave signal propagation at any designated field based on a comparison performed in [174]. We have created an outdoor scenario for a moving transceiver using the EM Terrano ray-tracing software [175]. As shown in Fig. 5.3, the EM Terrano tool simulates how the radio signal propagates in a chosen area, and it can compute the possible paths between the transmitter and the receiver nodes. It provides useful information about each propagated path, such as the total received power, angles of arrival and departure for every path propagating from the transmitter to the receiver, path power, delay, electric field, the number of hit points and their locations. These parameters are imported into

MATLAB to build a temporal 3D non-stationary multiple-input and multiple-output (MIMO) channel. Using MATLAB, we then integrate other factors, such as blockage effects. The separation distance between the antenna elements is a half-wavelength, i.e. $\lambda/2$.

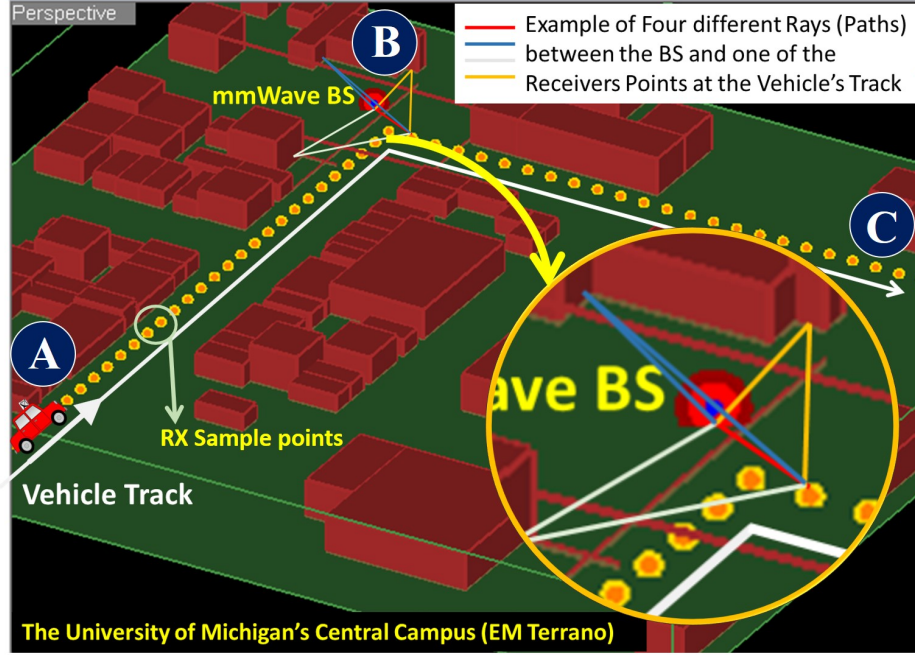


Figure 5.3: 3D View of the ray-tracing scenario.

5.3.1 Channel Modelling

We have created $\mathbf{H} \in \mathbb{C}^{N_T \times N_R}$ MIMO channel matrix for each possible propagation path between the transmitter and the receiver, where N_T and N_R are the number of transmitted and received antennas respectively. Since a narrowband channel is most suitable for simulating one subcarrier of orthogonal frequency-division multiplexing (OFDM) data transmission, we add all N_P paths together as follows:

$$\mathbf{H} = \sum_{i=1}^{N_P} \sqrt{\frac{\rho_i}{N_T}} \mathbf{a}_R(\phi_R^i, \theta_R^i) \mathbf{a}_T(\phi_T^i, \theta_T^i)^H \quad (5.13)$$

where ρ_i is the received power of each path, while \mathbf{a}_T and \mathbf{a}_R are the steering vectors of the TX and the RX respectively. They are functions of both azimuth $\theta_{T|R}^i$ and elevation $\phi_{T|R}^i$ angles of departure and arrival of path i .

5.3.2 Simple Directional Beamforming Technique

Simple directional beamforming is used on both the transmitter and receiver sides to increase energy efficiency. At each sample point, we assume the channel paths are measured through a beam training process, so we use beamforming to form multiple narrow beams that match each possible propagation path when one is blocked; we can therefore pick the best among the remaining beams. The received signal for the i th multipath is as follows:

$$y_i = \mathbf{a}_R(\phi_R^i, \theta_R^i)^H \mathbf{H} \mathbf{a}_T(\phi_T^i, \theta_T^i) \quad (5.14)$$

The received signal and the noise power of each path are computed respectively as $P_{Ri} = \mathbb{E}(y_i y_i^H)$, $\sigma^2 = \mathbb{E}(n_i n_i^H)$, where the noise part is $n_i = \mathbf{a}_R(\phi_R^i, \theta_R^i)^H \mathbf{n}_g$. The additive white Gaussian noise vector $\mathbf{n}_g \in \mathbb{C}^{N_R \times 1}$ has complex Gaussian distribution, i.e. each entry is distributed as $\mathcal{CN}(0, \sigma_n^2 \mathbf{I}_{N_R})$.

5.3.3 The Spectral Efficiency of each path

From the well-known Shannon equation [132], the spectral efficiency is computed as follows:

$$\text{SE}_i = \log_2(1 + \text{SNR}_i) \quad (5.15)$$

where $\text{SNR}_i = (P'_{Ri}/\sigma^2)$ is the signal to noise ratio.

5.3.4 Integrating Blockage with Channel Modelling

Since one of the main goals of this chapter is to investigate the small blockage effect on the overall mmWave system for a moving transceiver, we will study how to integrate the measured attenuation profiles into the ray-tracing model. Instead of increasing the complexity of the model by creating blockers within the environment built using the ray-tracing tool, similar to [176], we used one two-states Markov chain function that was proposed in Chapter 4; the function is published in [14]. The two states are: 1- non-blocked or blocked by one blocker, and the transition probability between them

determines the density of blockage. The advantage of this function is its ability to adopt any available blockage attenuation profile, such as the lab measurements presented in this chapter.

Thus, as the mobile transceiver moves, one of following two scenarios could happen for any propagated path i at each n sample point, and it is summarized in a flowchart of Fig. 5.4:

1. **Blocked Path:** when the Markov chain blocking function decides that there is a blocker affecting this sample point, the received power would be affected as follows:

$$P'_{Ri}(m) = P_{Ri}(m) - F(P_{BL}(l_B)) \quad (\text{dB}) \quad (5.16)$$

where $m = n : (n + l_B - 1)$ and we define $F(P_{BL})$ as an arbitrary blocker attenuation function that could be any attenuation profile P_{BL} presented in this chapter. The blockage effect lasts for l_B sample points, where l_B is a function determined by the blocker location and width.

2. **Non-blocked Path:** when there is no blocker affecting this sample point, the path received power remains the same as follows: $P'_{Ri}(m) = P_{Ri}(m)$ where $m = n$.

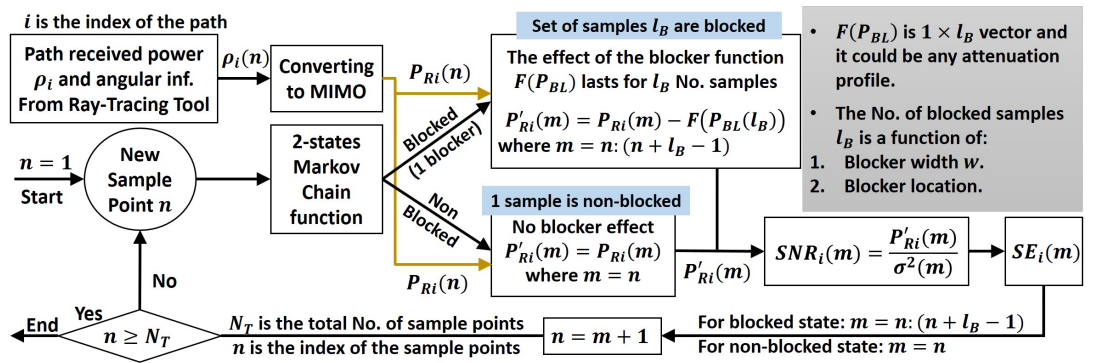


Figure 5.4: A flowchart that shows how the measured blockage attenuation profiles, provided in this chapter, are integrated into the ray-tracing model of an outdoor scenario. The integration is done by a single Markov chain function based on Chapter 4 (published in [14]). This flowchart applies for each path independently.

5.3.5 Simple Switching-beams Technique

In the presence of blockers, we can benefit from multi-paths by always selecting the largest amplitude path at any time. Once the strongest path is blocked, we switch to the second strongest path, as expressed in (5.17). This simple technique could improve the overall received power, which is explained in detail in Section 5.5.3.

$$P'_{R|Best}(m) = \max (P_{Ri}(m) : i = 1, \dots, N_P) \quad (5.17)$$

where $P'_{R|Best}$ is the received power of the strongest path in the presence of blockers, i is the path's index, and N_P is the maximum number of paths.

5.4 Measurement Settings

Measurement campaigns were carried out in an anechoic chamber at Heriot-Watt University to study small blocking objects. The blocker was placed exactly in the middle between two directional horn transmit and receive antennas, as shown in Fig. 5.5. The antenna locations are fixed in their positions while the blocker moves from left to right so that it crosses the LOS path in the middle between the transmitter and the receiver. Each blocker is vertically aligned to the LOS path. The blocker and both antennas are the same height. The centre carrier frequency is 28 GHz, but for some of the measurements, we sweep it over the range of (27 up to 29) GHz. The transmit power is -10 dBm. The remaining settings are shown in Table 5.1. For the given centre carrier frequency and the antenna dimensions D , the farfield zone starts from around $\geq \frac{2D^2}{\lambda} = 0.35 \text{ m} \approx 35\lambda$ [177]. The blockers are 1 m distant from each antenna. Thus, it is in the farfield zone. The TX-RX distance in all results is 2 m unless specified otherwise, and the blocker crosses the LOS path in the middle of the TX-RX distance.

Transmit Power	-10 (dBm)
TX-RX Distance	2 (m)
Antenna Type	20 (dB) Horn Antenna
Antenna Dimensions	3.5 x 2.5 (cm)
Chamber Dimensions	2.67 x 5 x 2.34 (m)
Height of TX, RX, and Blocker	1 (m)
Carrier Frequency	27, 28, 29 (GHz)
Sample Space	1 (cm) $\approx \lambda$
TX/RX Azimuth and Elev. (HPBW)	20.46°
Blocker's Dimensions (Width x Height)	
1- Small Square $BL(1)$	16.5 x 16.5 (cm)
2- Rectangular $BL(2)$	28.2 x 36 (cm)
3- Large Square $BL(3)$	33 x 33 (cm)
4- Cylinder $BL(4)$ and $BL(5)$	$r_{BL}=5.7$, $h=141$, thick. of 0.45 (cm)

Table 5.1: Lab Measurement Settings

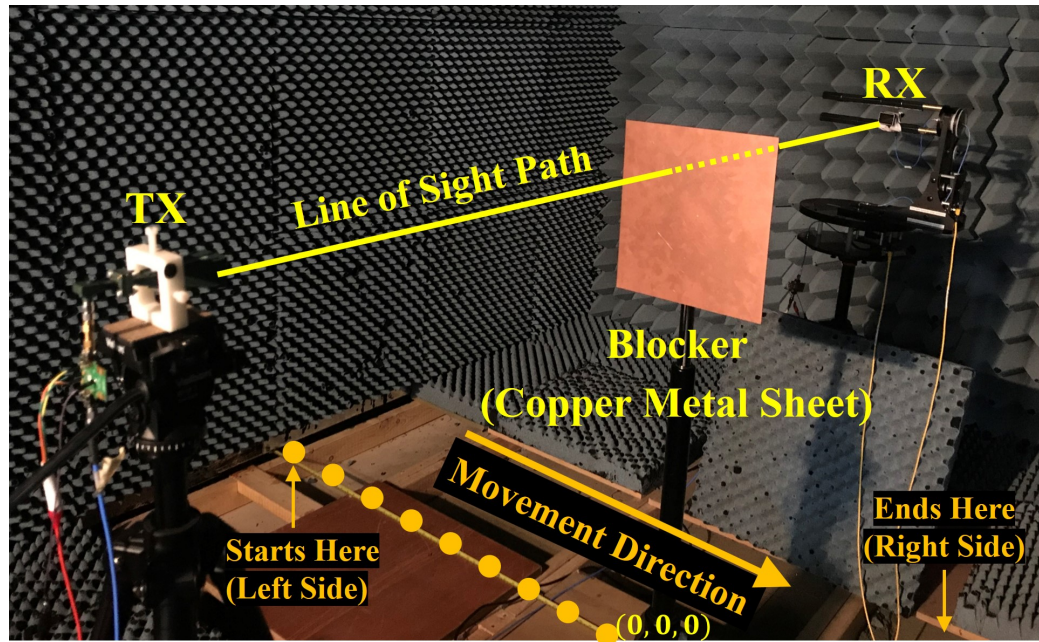


Figure 5.5: The rectangular metal sheet blocking the LOS in the anechoic chamber.

5.4.1 Blockers Types and Sizes

The size of Fresnel-zones is determined by the carrier frequency and scales with it. That means the Fresnel zones are quite small for the mmWave band. Thus, even a small object in an urban environment, such as street furniture, can severely affect the transmitted signal by blocking the main Fresnel zones. To investigate the attenuation effect of small objects, we have measured the attenuation of several relatively small blockers. Most road signs are metal sheets of different sizes, and their holding posts usually are either metal or strong plastic cylinders. In this chapter, we have carried out a measurement campaign for three types of blockers as follows:

1. Metal sheet blocker:
 - (a) **BL(1)**: Small square sheet - size: (16.5×16.5) cm.
 - (b) **BL(2)**: Rectangular sheet - size: (36×28.2) cm.
 - (c) **BL(3)**: Large square sheet - size: (33×33) cm.
2. Cylinder Blocker: the dimensions are: radius 5.7 cm, height 141 cm and thickness 4.5 mm.
 - (a) **BL(4)**: Plastic cylinder.
 - (b) **BL(5)**: Metallic cylinder: plastic wrapped with thick aluminium foil.

5.5 Results and Discussions

The results in this section are divided into three main parts. First, we investigate the impact of varying two terms of the 3GPP blockage model on the resulting attenuation, which are the screen width and the screen vertical orientation. Second, we apply all four KED simulation blockage models to each scenario of the five measured blockers. Here we consider only the vertical sides of the screen. In the third part of the results, we show how the measured blocker profiles can be incorporated in mmWave received spectral efficiency results for an outdoor scenario created using a ray-tracing tool.

5.5.1 Part 1 Results: Factors Affect the Attenuations of 3GPP

5.5.1.1 The Impact of Blocker Width

As shown in Section 5.2.1, considering all four sides of the blockage screen would result in lower attenuation than the only two sides case. Thus, we assume that the 3GPP screen has an infinite height. Having made this assumption, the blocker width is the only remaining difference between using the 3GPP model (5.4) to model two completely different blockers, e.g. a human body and a very small metal sheet of a road sign. It is clear from Fig. 5.1 (a) that when we increase the screen's width, the length of D_1 and D_2 in (5.3) will increase, which will result in a higher attenuation in (5.4). Fig. 5.6 shows the resulting attenuation of the 3GPP blockage model, i.e. (5.4), after fixing all other parameters and only varying the screen width within a range from 1λ to 35λ , where the wavelength is $\lambda \approx 1$ cm and the centre carrier frequency is 28 GHz.

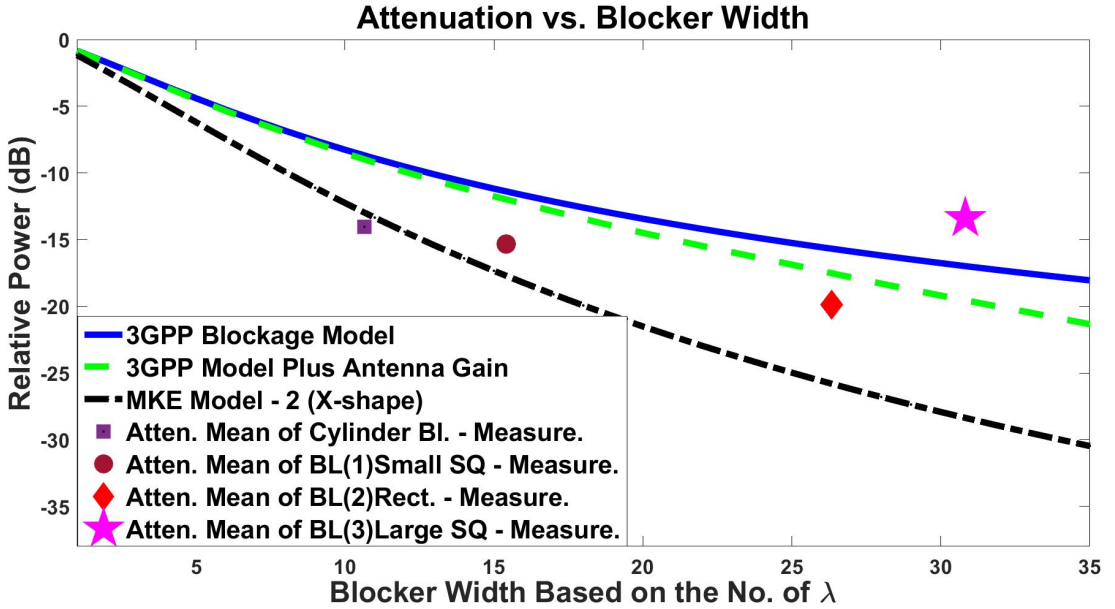


Figure 5.6: Blockage attenuation versus blocker width in terms of λ . Comparison between measurements, 3GPP model (5.4), 3GPP (including the antenna gain) (5.5), and MKE model (X-shape) (5.7). The centre carrier frequency is 28 GHz.

To evaluate the performance of the 3GPP blockage model on capturing the attenuation

caused by small blockers, we compare the curve with some lab measurements. Fig. 5.6 shows four measured attenuation marks that are obtained by taking the mean value of the main body of the measured attenuation of each one of the following different-size blockers: a plastic cylinder and the three metal sheets with different sizes, i.e. $BL(1) \rightarrow BL(4)$. These are represented by a square, circle, diamond, and star marks respectively.

It is clear from Fig. 5.6 that all the four marks of the measured attenuations, which belong to blockers of different sizes, have roughly the same attenuation level. The narrow beamwidth of the directive antennas plays an important role here; even small-size blocker blocks a large portion of the antenna's main beam which results in weak wavelets that occur beyond a certain width of blocker.

We find that the smaller the width of the blockage body is, the worse the 3GPP simulation model becomes at capturing the measured attenuation. Moreover, as discussed in Section 5.2.2, adding the antenna gain would only slightly increase the attenuation of the 3GPP model by 2 or 3 dB, which is still far from the measured value of the small square blocker $BL(1)$, i.e. the brown circle in Fig. 5.6. Thus, we apply the two knife-edge screens (MKE) model, and we find that its attenuation curve is closer to the measurements of blockers with a very narrow width such as the case of the narrow cylinder blocker $BL(4)$, i.e. the purple square point, and the small square blocker $BL(1)$, i.e. the brown circle in Fig. 5.6. The wider the blocker, e.g. the red diamond point of $BL(2)$ in Fig. 5.6, the more the including-gain model becomes effective. The attenuation of each one of the blockers will be analysed in detail in the following.

5.5.1.2 The Impact of Blockage Screen Orientation

The orientation of the blockage screen shown in Fig. 5.1 plays an important role in the resulting attenuation. References [5, 12] state that the blockage screen should always be perpendicular to the direct line connecting TX and RX, while reference [164] has aligned the screen to the movement axis of the blocker. Moreover, the authors of [87] suggested that a further investigation of the impact of changing the orientation of the blockage screen could be useful. Based on the previous discussion, we have

investigated the orientation issue further. To study the impact of the screen on the resulting attenuation, the blockage screen in Fig. 5.1 is rotated to scan all the possible angles from 0° up to 90° corresponding to the LOS path, where zero degrees means that the screen is aligned to the LOS path and 90° is perpendicular to the LOS path. It is clear from Fig. 5.7 that the screen orientation plays a significant role in the resulting attenuation, with the maximum occurring when it is perpendicular to the LOS path. The difference in the resulting attenuation values between the two angles, i.e. 0° and 90° , could be as high as 17 dB for a screen with a width of 33 cm. This finding highlights that the maximum attenuation is obtained by having the blockage screen perpendicular to the LOS path as in the 3GPP [5] model. Moreover, from the figure, we can deduce that the TX-RX distance and the screen width values also change the resulting attenuation.

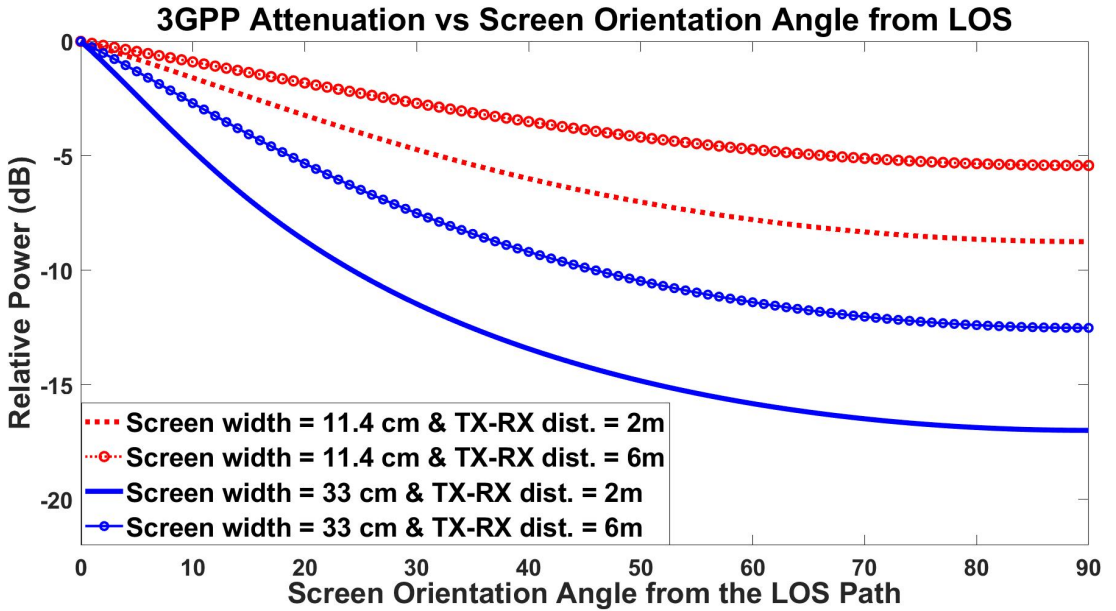


Figure 5.7: Blockage attenuation versus blocker screen orientation, in degrees, referred to the LOS path. Four scenarios of the 3GPP model (5.4); two screens size at two different TX-RX dis The centre carrier frequency is 28 GHz.

5.5.2 Part 2 Results: Attenuation of the 5 Small Blockers (Lab-Measurements versus the 4 KED Simulation Models)

In the following subsections, we present the measured attenuation caused by each one of the five blockers, i.e. $BL(1) \rightarrow BL(5)$. For each blocker, we apply all the four KED blockage simulation models: a) 3GPP eq. (5.4), b) 3GPP + including the gain eq. (5.5), c) MKE eq. (5.7), and d) mmMAGIC eq. (5.8). It should be mentioned that the measurement settings were the same for all blockers. Each blocker is moved from the left side of the anechoic chamber to right side perpendicularly crossing the LOS in the middle between the two antennas, i.e. 1 m from each antenna, as shown in Fig. 5.5. The distance between each measurement is $1 \text{ cm} \approx \lambda|_{f_c=28 \text{ GHz}}$. All figures show the blockage attenuation values on their own, i.e. removing the path loss effect, as in [12, 13].

5.5.2.1 Attenuation of BL(1): (16.5×16.5) cm metal sheet:

Fig. 5.8 shows the measured attenuation caused by a small square metal sheet sized $16.5 \text{ cm} \times 16.5 \text{ cm}$. The measured curve has a W-shape with two troughs. When the blocker is exactly in the middle between the two antennas, the attenuation value is $\approx -10 \text{ dB}$. When we slightly move the blocker by 5 cm to the right side or the left side but still blocks the LOS path, the attenuation value increases to 25 dB, which could be due in part to detailed diffraction effects not captured by the 3GPP model. As stated in [165], the Huygens-Fresnel integral method provides a perfectly absorbing screen that could capture the fluctuations. That comes with a higher complexity compared with the 3GPP blockage model.

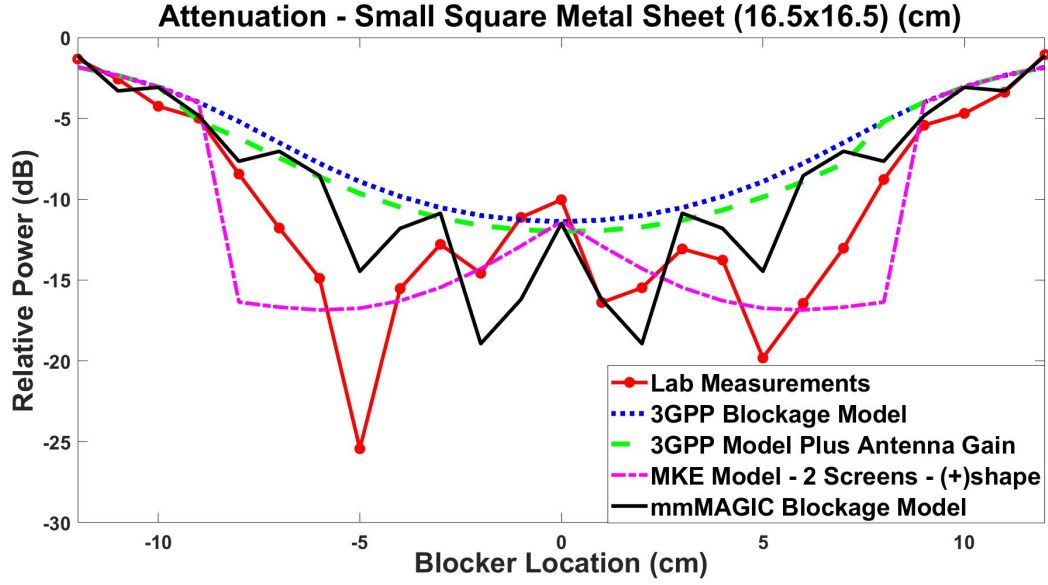


Figure 5.8: The attenuation of BL(1): (16.5 cm by 16.5 cm) metal sheet. Comparison between measurements and the following models: a) 3GPP eq. (5.4), b) 3GPP (including the antenna gain) eq. (5.5), c) MKE (+)-shape eq. (5.7), and d) mmMAGIC eq. (5.8). The centre carrier frequency is 28 GHz.

Although the curve of the 3GPP model, in Fig. 5.8, matches the measured attenuation curve when the blocker is exactly in the middle, it fails to estimate the two troughs with around 20 dB difference. As discussed earlier, including the antenna gain into the calculations does not help. Simulating the attenuation using one 3GPP screen is insufficient. However, the mmMAGIC blockage model has an advantage over the 3GPP model since it accounts for the fast-fading resulting from summing the diffracted paths in the deep shadow behind the blocker. It indirectly models the new wavelets of the Huygens-Fresnel principle, and it accounts for the fluctuations resulting from summing the diffracted paths, which is mimicking what happens in the actual diffraction effect. The mmMAGIC curve performs closer to the measured attenuation, but it is not able to replicate the two main attenuation peaks at (+/- 5) cm locations. Thus, to maintain the simplicity of the KED theory, we apply two screens with a (+) shape that are perpendicular to each other, as shown in Fig. 5.1 (b). The two screens MKE model has very good performance; it follows the trend of the measurements curve very well. Since the blocker has a narrow width, the two screens MKE model provides the best fit to the actual results.

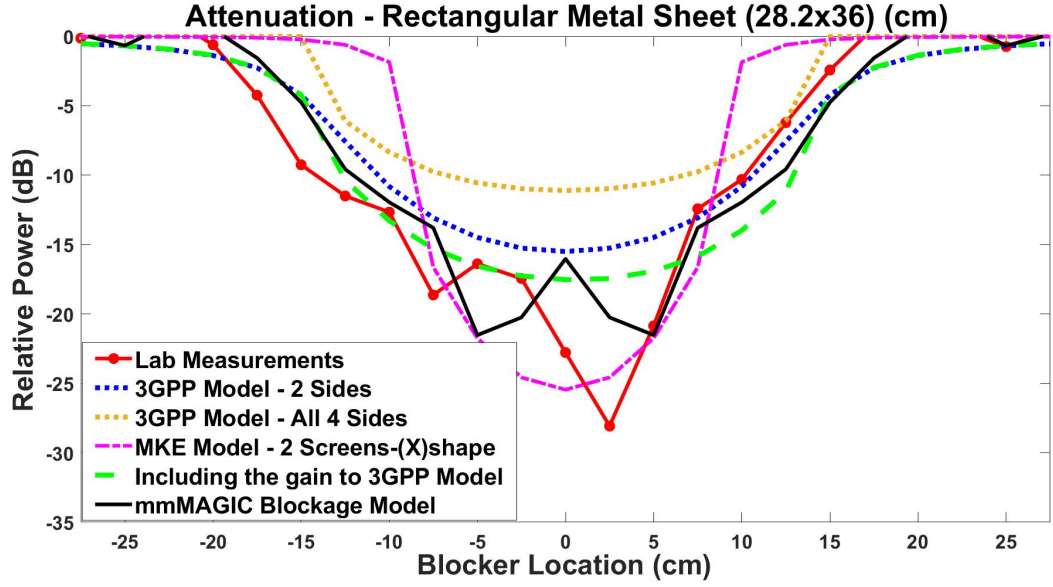


Figure 5.9: The attenuation of BL(2)- Scenario (1): (36 cm by 28.2 cm) metal sheet. TX-RX distance is 2 m. Comparison between measurements and these models: a) 3GPP (4-sided eq. (5.2) & 2-sided eq. (5.4)), b) 3GPP (including the antenna gain) eq. (5.5), c) MKE (X)-shape eq. (5.7), d) mmMAGIC eq. (5.8). The carrier frequency is 28 GHz.

5.5.2.2 Attenuation of BL(2): (36 × 28.2) cm metal sheet:

Scenario (1): blocker is not close to the antenna (It does not completely block the entire main antenna beam, i.e. $W_{HPBW} > w$ in Fig. 5.2): As shown in Fig. 5.9, the measured attenuation caused by a rectangular metal sheet, which is wider than the previous one, has a V-shape curve has a maximum attenuation of 28 dB. The 3GPP simulation curve is closer to the measurement curve, but still, there is a gap of ≈ 13 dB in the middle. However, including the antenna gain enhances the 3GPP performance further, by around 2 or 3 dB. Apart from the 10-dB difference at zero distance, the 3GPP model with the antenna gain included shows a good fit to the data. The mmMAGIC model follows the measured curve, but it underestimates the highest attenuation peak around the middle at 2.5 cm location. However, the X-shape MKE model has a better fit to the main body of the attenuation, where the difference between the two curves is only ≈ 3 dB. However, when the blocker is not exactly in the middle, the 3GPP model with the antenna gain provides a better fit. Regarding the 3GPP blockage model, as mentioned

above, considering only the vertical edges, i.e. (5.4), results in a higher attenuation than considering all the four sides, i.e. (5.2).

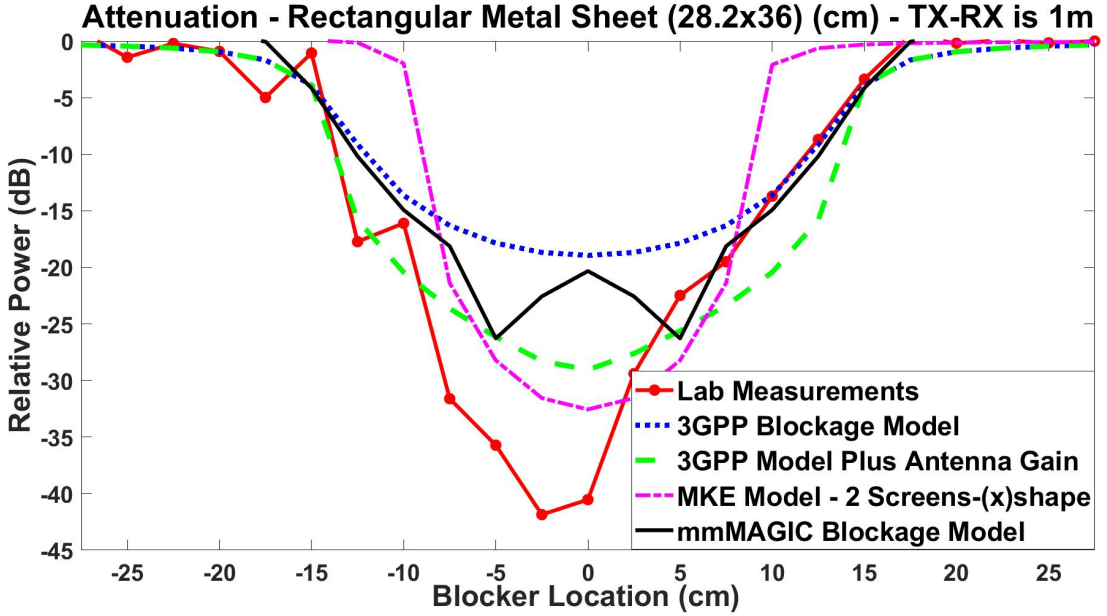


Figure 5.10: The attenuation of BL(2) - Scenario (2): (36 cm by 28.2 cm) metal sheet. Comparison between measurements and the following models: a) 3GPP eq. (5.4), b) 3GPP (including the antenna gain) eq. (5.5), c) MKE (X)-shape eq. (5.7), d) mm-MAGIC eq. (5.8). The carrier frequency is 28 GHz.

Scenario (2): blocker in the farfield but it is still close to the antenna (It completely blocks the entire main antenna beam, i.e. $W_{HPBW} \leq w$ in Fig. 5.2): As discussed in case one of Section 5.2.2, including the antenna gain into the 3GPP blockage calculation would improve the performance of the blockage simulation on one condition: if the main beam is completely blocked. This happens in one of two scenarios: either the blocker is very large, or the blocker is located close to the antenna, so it blocks the main lobe of the beam pattern. Fig. 5.10 shows that after bringing the rectangular-sheet blocker closer to the transmitter antenna, the 3GPP with the antenna gain model shows an improvement of around 10 dB over the original 3GPP blockage model. However, it still underestimates the measurements, and the MKE model is closer to the peak of the measured loss at 2.5 cm.

5.5.2.3 Attenuation of BL(3): (33 × 33) cm metal sheet:

The blocker sheet is now about 30λ wide, Fig. 5.11 shows that the two-sided 3GPP model (5.2) successfully fits the measurements curve for three different centre carrier frequency. However, the 3GPP simulation results do not show a significant change after increasing the centre carrier frequency by 2 GHz (i.e. from 27 GHz to 29 GHz). The measurement results show again some fluctuations, which are again not captured due to the limitations of the 3GPP model. The mmMAGIC model shows a fluctuation that has similar behaviour to the measured curve, but it slightly overestimates the measured attenuation.

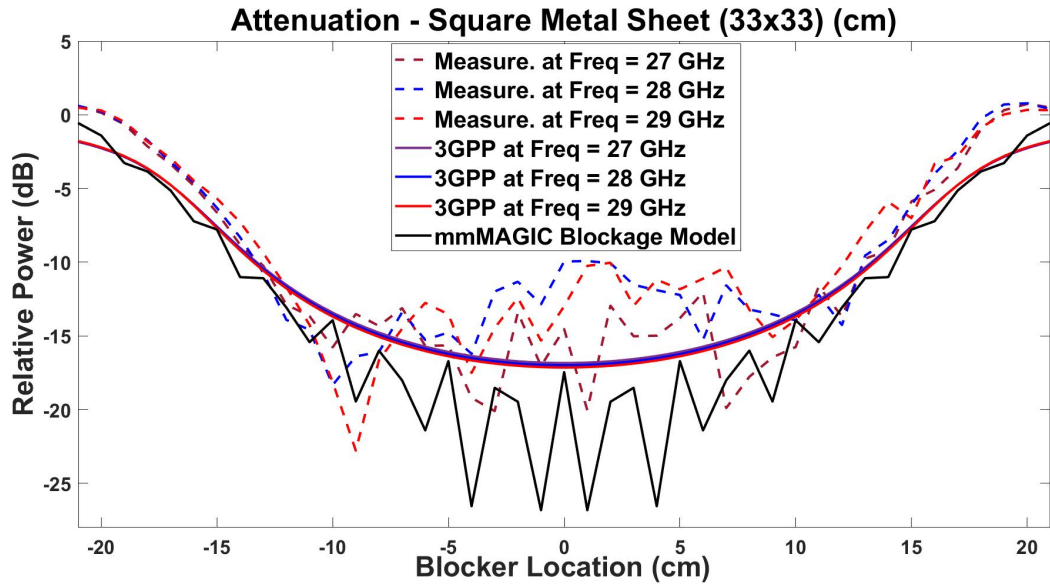


Figure 5.11: The attenuation of BL(3): (33 cm by 33 cm) metal sheet for three different frequencies. Comparison between measurements and the following models: a) 3GPP eq. (5.4), and b) mmMAGIC eq. (5.8)

5.5.2.4 Attenuation of BL(4): The Plastic Cylinder:

The cylinder blocker has a more complex structure in comparison to the metal sheet blocker. We have three scenarios for the cylinder blocker: two of them are for a plastic cylinder in different positions – blocking or not blocking the antenna main beam – in order to study the impact of adding the antenna gain to the loss calculation. The third

is for a cylinder wrapped in aluminium foil. The width here is even smaller than the width of all the previous metal sheet blockers: the cylinder diameter is 11.4 cm.

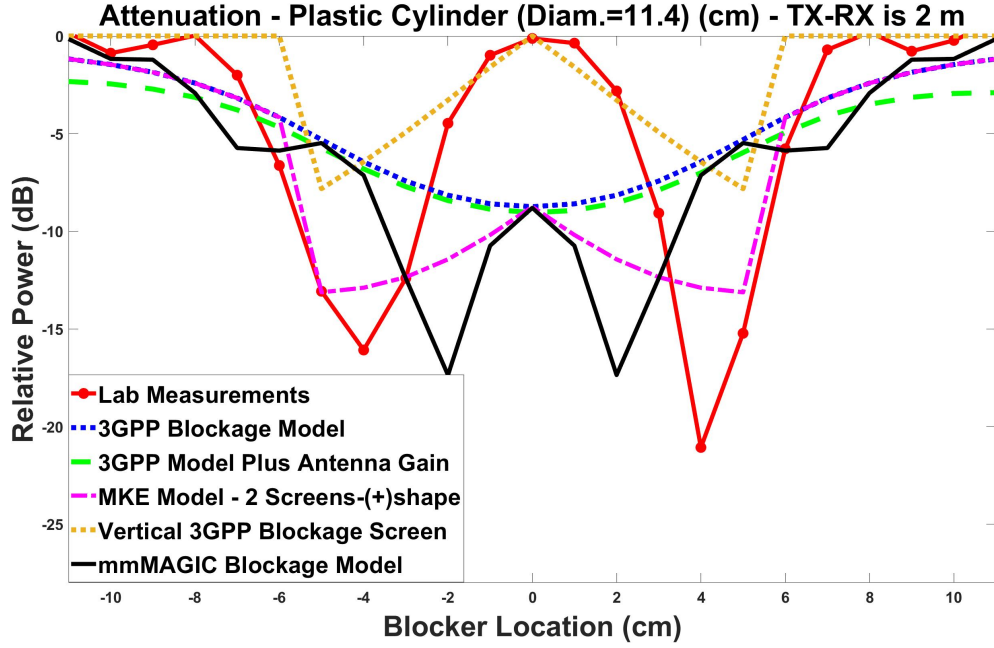


Figure 5.12: The attenuation of BL(4)- Scenario (1): the plastic cylinder. Comparison between measurements and these models: a) 3GPP eq. (5.4), b) Vertical 3GPP eq. (5.4), c) 3GPP (including the antenna gain) eq. (5.5), d) MKE (+)-shape eq. (5.7), and e) mmMAGIC eq. (5.8). The carrier frequency is 28 GHz.

Scenario (1): blocker is not close to the antenna (It does not completely block the entire main antenna beam, i.e. $W_{HPBW} > w$ in Fig. 5.2): In Fig. 5.12, the 3GPP blockage model fails to match the measurements. Given the cylinder width and location, the main beam of the directive antenna is not completely blocked. Thus, as explained in Section 5.2.2, including the antenna gain into the calculation of the 3GPP blockage does not show a significant improvement. However, the measurements show a W-shaped curve, where the attenuation in the middle is close to zero, and it peaks when the blocker is moved to either side. One possible justification for this is that the diffracted rays around the two vertical sides of the plastic cylinder are adding constructively, so they give the maximum value in the middle where the constructive interference occurs. This could happen when two waves are in-phase. However, making the orientation of the 3GPP blockage screen parallel to the LOS, i.e. the golden dotted line,

gives a closer behaviour for the measured attenuation than the case of having the 3GPP screen perpendicularly orientated to the LOS; however, it does not capture the peaks at (± 4) cm locations. The curve of the (+)-shaped MKE model shows behaviour that is close to the measurements, but it does not capture the zero attenuation at the middle, i.e. at zero distance. The mmMAGIC blockage model considers the fading resulting from summing the reflected paths, which is the advantage of the model over the 3GPP model. Although the mmMAGIC model shows the same behaviour as the measured curve, it does not match well. However, as stated in [178], due to the shape of the cylinder blocker, the KED model may not accurately capture the loss since it is based on a sharp edge assumption not a curved surface. Using a creeping wave linear model, as in [179, 180], may result in a better fit with the measured loss.

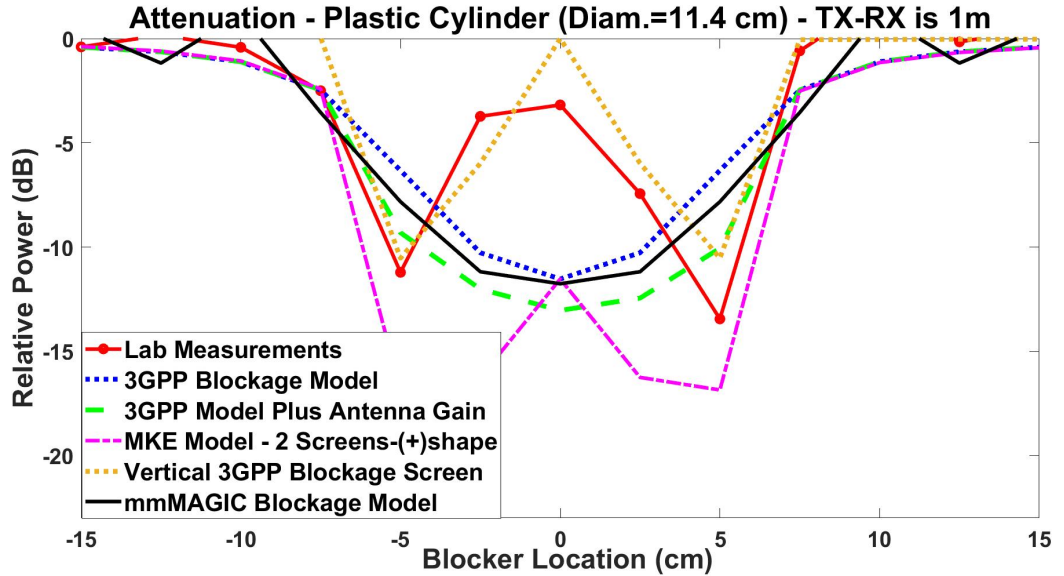


Figure 5.13: The attenuation of BL(4): the plastic cylinder. Comparison between measurements and the following models: a) 3GPP eq. (5.4), b) Vertical 3GPP eq. (5.4), c) 3GPP (including the antenna gain) eq. (5.5), d) MKE (+)-shape eq. (5.7), and e) mmMAGIC eq. (5.8). The centre carrier frequency is 28 GHz.

Scenario (2): blocker in the farfield but it is still close to the antenna (It completely blocks the entire main antenna beam, i.e. $W_{HPBW} \leq w$ in Fig. 5.2): Similar to the rectangular sheet in Fig. 5.13, we brought the plastic cylinder closer. As stated in Section 5.2.2, the 3GPP plus the antenna gain model shows improvement over the 3GPP blockage. The mmMAGIC model here behaves equally to the 3GPP model.

However, by changing the 3GPP screen orientation to be aligned in parallel to the LOS path, we get the best fit for the measurements, i.e. the golden dotted line in Fig. 5.13.

5.5.2.5 Attenuation of BL(5): The Metallic Cylinder:

As shown in Fig. 5.14, the measured attenuation of the metallic cylinder curve has a W-shape where in the middle it is around -15 dB, while it reaches -20 dB when the blocker is moved to either side. The behaviour of our measurements is consistent with the measurements of [162], who used a metal cylinder to model the attenuation caused by a human leg in the 60 GHz carrier frequency band. Both the 3GPP model with and without the antenna gain included in the loss computation underestimates the measured loss. The MKE model shows a similar trend to the measurements, but in the middle it underestimates it by around 5 dB. The best model here is the mmMAGIC model, which it has a good fit with the measured curve.

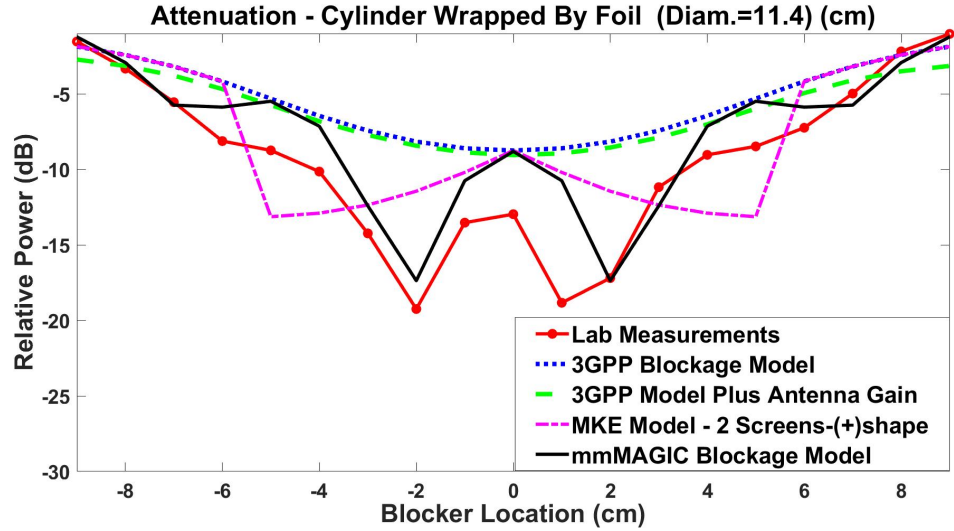


Figure 5.14: The attenuation of BL(5): the metallic cylinder. Comparison between measurements and the following models: a) 3GPP eq. (5.4), b) 3GPP (including the antenna gain) eq. (5.5), c) MKE (+)-shape eq. (5.7), and d) mmMAGIC eq. (5.8). The centre carrier frequency is 28 GHz.

Discussion: Thus, we can conclude from all the above results that the 3GPP blockage simulation model, i.e. model 1, works very well when the blocker width is roughly $\geq 30\lambda$. When the blocker is in the range of $10 - 20\lambda$, even including the antenna

gain into the 3GPP blockage calculations may not fit well with the measured results. Moreover, the second model, i.e. the 3GPP plus antenna gain model, only shows good agreement with the measured loss curve if the blocker completely blocks the main beam of either antenna, as in Fig. 5.10. Otherwise, this model tends to underestimate the measured losses. However, the MKE model shows a better fit with the measurements. The KED theory is based on a very sharp-edge assumption, and this sharpness dimension scales with the wavelength [173]. For $f_c = 28$ GHz even the metal sheet is not sharp. The structure becomes three dimensional concerning the mentioned wavelength, which explains the need for the MKE blockage model to fit the measured data better. Furthermore, the mmMAGIC model generally shows a good fit with the measured loss. A summary of all the previous results is presented in a simple flowchart in Fig. 5.15.

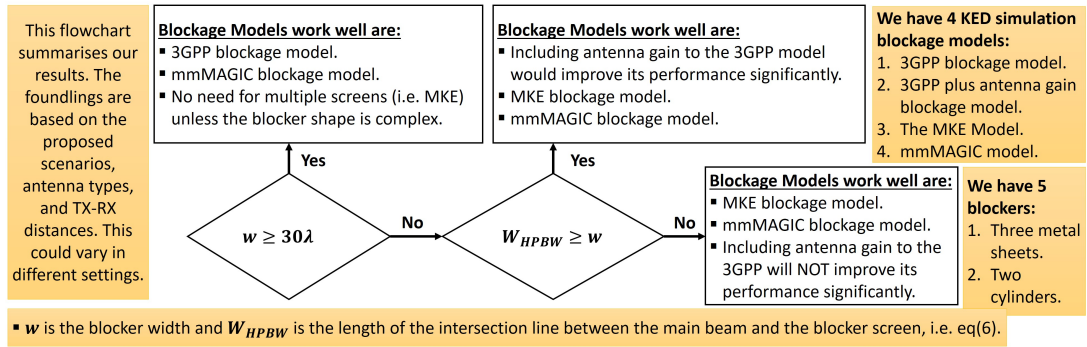


Figure 5.15: A flowchart summarizes Part 2 results, i.e. Section 5.5.2, and explains which blockage simulation model would fit the measurements better.

The attenuation values for both simulation and measurements do not change significantly with increasing the carrier frequency, as shown in Table 5.2. To evaluate the performance of each blockage simulation model for each blocker type, we have computed the mean squared error (MSE) considering the measurements as the reference point. For each blocker size, the whole attenuation curve of each model: 3GPP, 3GPP plus antenna gain, MKE, and mmMAGIC are compared with the whole measured attenuation curve using the MSE function. The results in Table 5.3 support the findings in the previous subsections. It is obvious from the table that the MKE model is the better option for blocker $BL(1)$. However, the 3GPP blockage model plus the antenna

gain is the best model for the rectangular sheet, i.e. $BL(2)$, but if we want to capture the highest attenuation value, we need the MKE model, as shown in Fig. 5.9. For the large square metal sheet, i.e. $BL(3)$, the 3GPP model works very well. In general, both the MKE and the mmMAGIC models work well for small blockers.

Mean Blockage Attenuation (dB)			
Blocker Type	Central Frequency		
	27 GHz	28 GHz	29 GHz
$BL(1)$: Small Square	-13.27	-14.12	-14.62
$BL(2)$: Rectangular	-17.76	-17.75	-16.6
$BL(3)$: Large Square	-14.71	-12.88	-12.83
$BL(4)$: Plastic Cylinder	-6.59	-6.17	-5.66
$BL(5)$: Metallic Cylinder	-12.47	-12.77	-12.45

Table 5.2: Frequency Comparison based on the Mean Value of the Main Body of the Measured Attenuation for All Blockage Models.

Mean Squared Error					
Blocker Type		Simulation Blockage Model			
		3GPP	3GPP+ Gain	MKE	mmMAGIC
$BL(1)$ Small Square		0.023	0.017	0.008	0.011
$BL(2)$ Rect.	Close	0.015	0.0129	0.0936	0.0186
	Far	0.0168	0.0164	0.08	0.0126
$BL(3)$ Large Square		0.0203	0.025	0.16	0.024
$BL(4)$ Plastic Cyl.	Close	0.0483	0.0482	0.0558	0.0444
	Far	0.088	0.104	0.08	0.115
$BL(5)$ Metallic Cyl.		0.0302	0.026	0.017	0.0086

Table 5.3: Comparisons Between the Simulation Blockage Models Based on MSE - Measurements are the Reference Point - $f_c=28$ GHz

5.5.3 Part 3 Results: Blocker effects on the mmWave channel

In this part, the chapter's focus moves to show how the measured attenuations are used in computer simulations to do an overall system evaluation of mmWave in the presence of blockers. As shown in Fig. 5.3 and Fig. 5.4 of Section 5.3, we have created an outdoor scenario for a moving transceiver using the EM-Terrano ray-tracing tool. The length of the moving transceiver's trajectory is 150 m, where the TX is on the side of the trajectory. The space between the sample points along the trajectory is 1λ . Both transmitter and receiver sides are implemented by 8-by-8 uniform plane array UPA, i.e. MIMO system. Also, at each side, we have several beams simultaneously, one directed at each possible path. From the ray-tracing tool, we found that for the trajectory scenario proposed in Fig. 5.3, the number of possible paths travelling from TX to RX is between 2 and 8 paths, depending on the location of the mobile transceiver. An arbitrary attenuation function has been applied randomly on each propagated path at different locations by using the two-states Markov chain blocking function [14]. The attenuation function represents the different blockage attenuation measurements provided in this chapter. In the following results, two out of the five blocker types, provided in this chapter, have been integrated into the ray-tracing tool. These blockers are $BL(3)$: the 33-by-33 cm square metal sheet, and $BL(5)$: the metallic cylinder. Most road-signs have similar shapes to these blockers.

Fig. 5.16 shows the received spectral efficiency (SE) of 200 sample points within a two-meter sector of the mobile track. We only consider the two strongest paths, plus the switching-paths technique. For each path, we have plotted three curves: 1- The green dotted curve that shows the received SE when there is no blocker at all. 2- The red curve which represents the received SE including blockage effects. The attenuation is taken from the measurements of this chapter. 3- The blue dashed curve represents the received SE with blockers effects, but the blockers are from the simulation models rather than the measurements. For blocker $BL(3)$, we choose the best fit simulation blockage model which is the 3GPP model, while for $BL(5)$ blocker, we applied the mmMAGIC model. From these curves, we conclude two points: 1- even small blockers could affect the signal significantly and attenuate the received SE by around 6-7 bits/s/Hz. 2- the simulation models (i.e. the blue curves) could be used instead of the

measured attenuation (i.e. the red curve) since they show a similar performance.

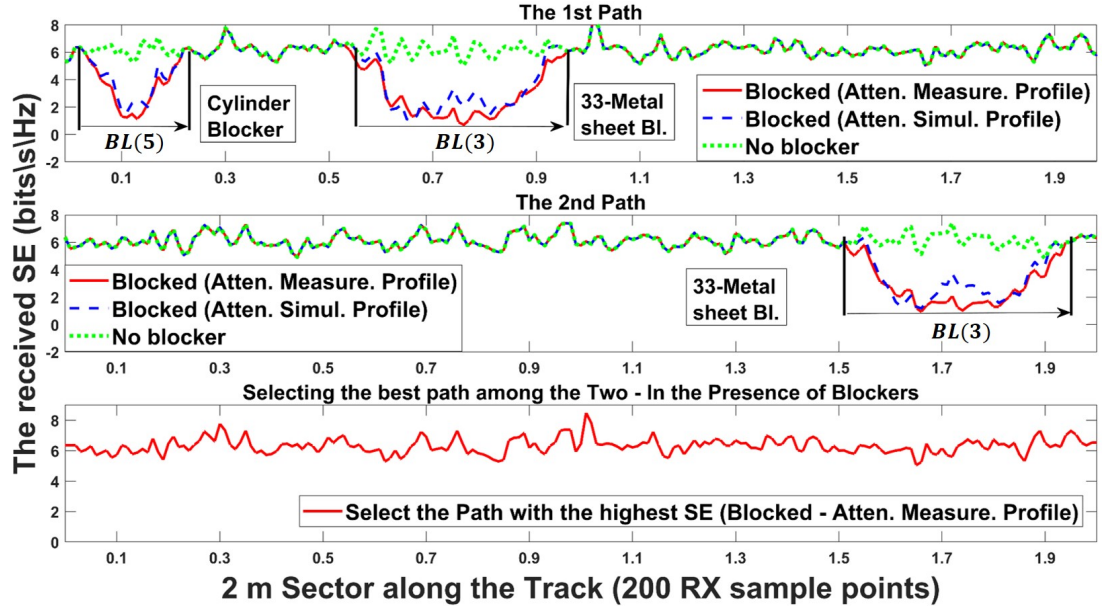


Figure 5.16: The received SE (1 run) at a sector of the RX track in the presence of two blocker-types: $BL(3)$ and $BL(5)$. The first path, the second path, and selecting the highest among the two. In the first two subplots, the red curves represent the lab-measured attenuation of the blockers while the blue curves are the simulated attenuation (3GPP for $BL(3)$ and mmMAGIC for $BL(5)$).

The LOS and reflected paths arrive from different angles; so if a blocker crosses one of these paths, the others may not be affected. Thus, the Markov chain blocking function is independently applied to each path. In Fig. 5.16, the LOS path is attenuated by two different blockers while only one blocker attenuates the signal of the second path. The width of the $BL(3)$ blocker is almost triple the width of $BL(5)$, so $BL(3)$ attenuates the signal for longer.

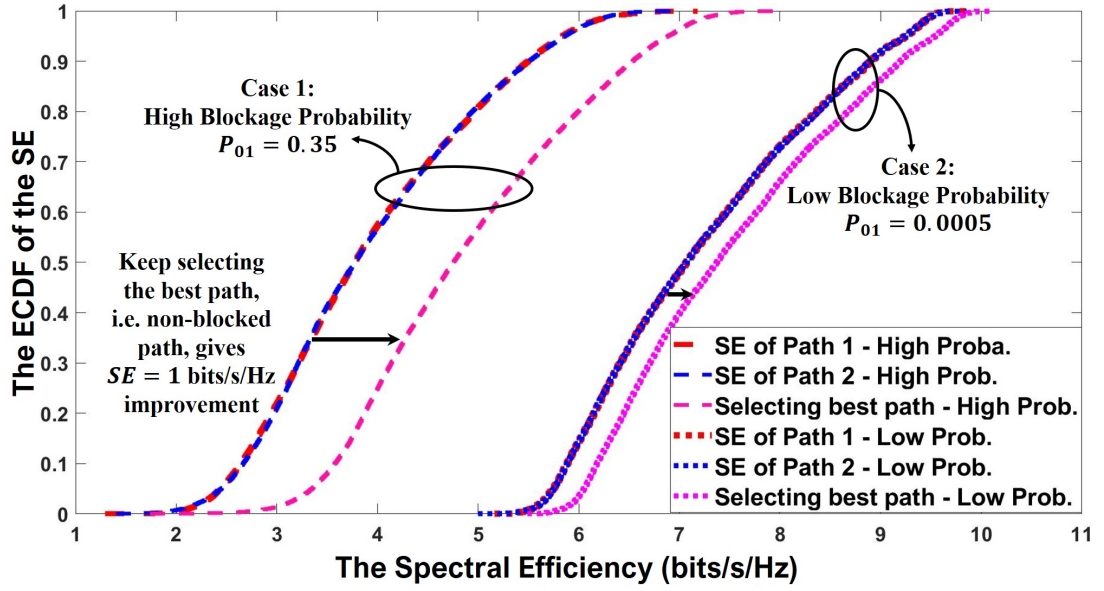


Figure 5.17: The ECDF of the received SE of 15000 RX sample points along the (150 m) RX trajectory - 20 runs. Two cases: high and low blockage probabilities, $P_{01} = 0.35$ & $P_{01} = 0.0005$. For each case, three curves: 1) LOS Path. 2) Reflected-Path. 3) Selecting the non-blocked path among them.

Blockage Probability (2-states Markov chain function)	ID of the Blocker Type	1 st Path		2 nd Path		Ave. SE of the Best Path of the two in the Presence of Blockers
		1) No-blocker Scenario		1) No-blocker Scenario		
		Ave. SE = 7.25 bits/s/Hz		Ave. SE = 7.23 bits/s/Hz		
		2) Scenario: Blockers are present in between TX and RX				
		Blocked (Simulation)	Blocked (Meas.)	Blocked (Simulation)	Blocked (Meas.)	
Low $P_{01}=0.0005$	$BL(3)$	6.99	6.95	6.98	6.94	7.46
	$BL(5)$	7.15	7.13	7.14	7.12	7.51
Medium $P_{01}=0.0095$	$BL(3)$	5.4	5.06	5.38	5.04	6.29
	$BL(5)$	6.2	6.01	6.19	6	6.99
High $P_{01}=0.35$	$BL(3)$	4.30	3.76	4.30	3.76	4.56
	$BL(5)$	4.77	4.31	4.78	4.32	5.27

Table 5.4: The average received spectral efficiency (bits/s/Hz) for the first path, second path, and the best of them. Three different blockage probabilities and two blockers type (BL(3) 33-Metal sheet and BL(5) Metallic cylinder).

Fig. 5.17 shows the empirical cumulative distribution function (ECDF) of the average SE over all sample points, in the presence of blockers, of two different blockage probabilities: high and low, where $P_{01} = 0.0005$ & 0.35 respectively. It is clear from Fig. 5.17 that the switching-paths technique works very well, especially in the high blockage probability case. It selects the strongest received path, and whenever this path is blocked, it automatically switches to the second strongest path to maximise the SE. In the case of high blockage probability, it shows a 1 bit/s/Hz improvement over each one of the two blocked paths. Table 5.4 shows the average received SE for three levels of blockage probabilities. The higher the probability, the lower the overall average SE. Due to the wider width of the $BL(3)$ sheet blocker, it attenuates the signal more than the $BL(5)$ cylinder blocker. Similar to the first two subplots in Fig. 5.17, each blocker is represented by two attenuation profiles: the lab-measured attenuation of the blockers and the simulated attenuation (3GPP for $BL(3)$ and mmMAGIC for $BL(5)$).

Discussion: This subsection shows that it is possible to integrate a lab-measured attenuation within a ray-tracing model without increasing the complexity. The results of the ray-tracing models show how these small blockers could affect the received signal and reduce the SE. Moreover, from Fig. 5.16, it is clear that the simulation models could be used as an alternative to measurements since they both lead to similar effect.

5.6 Conclusions

In mmWave frequencies, small objects such as metal road signs, etc., can cause significant attenuation that is in the range of 15–30 dB. In this study, we have taken measurements for five blockers of different sizes and types, i.e. metal sheets and cylinder blockers. We have adopted four blockage simulation models. We found that the 3GPP blockage model underestimates the measurements of small-size blockers by around 10 dB while using the multiple knife-edge model fits the measured attenuation curve. Additionally, the curve of the mmMAGIC blockage model, in general, performs closely to the measured attenuation. The wider the blocker, the better performance the 3GPP loss equation can achieve. The four-sided 3GPP blockage model gives a lower overall attenuation than the case of considering only the vertical sides.

We have also discussed in detail the impact of including the antenna gain to the 3GPP blockage model, which shows only a slight improvement of about 2 or 3 dB over the 3GPP model. Also, increasing the centre carrier frequency by 2 GHz does not lead to a significant difference in the 3GPP simulation results. However, this increase shows some fluctuations in the measurement curves. Moreover, the spectral efficiency results of the mmWave system for an outdoor environment, created using a ray-tracing tool, shows that even a small-size blocker attenuates the received signal by 6-7 bits/s/Hz. We have shown that beam-switching technique for choosing the most reliable path is an effective strategy for reducing the blockage effect.

The next chapter summarises the thesis work and highlights the main contributions of the thesis.

Chapter 6

Conclusions and Future Work

This thesis aimed to provide a better understanding of one of the main challenges that face operating at mmWave band which is sensitivity to blockage effects. This is done by implementing new efficient models that accurately capture the blockage effects on the mmWave signal strength. This thesis contributes to the field of 3D dynamic blockage modelling for mmWave communication systems by introducing new efficient mathematical models; also, by providing a set of lab measurements, which are compared to the state-of-the-art blockage models. This chapter briefly highlights the main achievements of this research by first stating the main problems that the thesis aimed to solve. Then, it succinctly summarises the thesis work, and states the limitations which provide possible directions for future work. Thus, the chapter is divided into three main sections to cover the three points mentioned above.

6.1 The Research Questions and The Novelty of the Work

The severe effects that blockages cause to mmWave signal strength is a serious problem. Not only the high power-loss but also the dynamics of this loss due to blockage motion makes the mmWave communication link unreliable. This impedes us from benefitting from the substantial advantages of mmWave band such as contiguous bandwidth. Although there are several engineering techniques to deal with power loss, that is not feasible without first capturing and understanding the behaviour of the dynamic attenuation caused by blockers. Modelling the dynamics of the blockage is essential for evaluating high gain beamforming techniques, which are used to improve the signal strength in the mmWave communication systems. Modelling the dynamic channel attenuation can be achieved by using several approaches, such as a ray-tracing tool or 3D geometric models. Although these modelling approaches show excellent performance

in capturing the channel attenuation, the higher complexity makes them less practical for the performance analysis of mmWave signal strength when blockers are present in the environment. This thesis comes to fulfil this research need by providing very efficient models that accurately capture the channel attenuations caused by blockers surrounding a moving transceiver. Our work also shows that even small size objects can block and severely affect the mmWave signal which has small Fresnel zones. The thesis contributed by providing a better understanding of the blockage effects of small-size blockers, which is achieved by experiments and simulation.

6.2 Conclusions of The Main Contributions

This section briefly summarises the novelty work of the three main achieved contributions: 1) Modelling the dynamic channel attenuation for V2I mmWave communications. 2) small-sized blockage propagation modelling for mmWave bands. 3) evaluation of the signal strength of mmWave MIMO systems for a multi-path scenario in the presence of time-varying blockers.

6.2.1 Modelling the Dynamic Channel Attenuation for V2I mmWave Communications

This thesis proposes two novel efficient Markov chain models that are designed to successfully perform the two main tasks: capturing the dynamics of blockers affecting a moving transceiver and computing the corresponding channel attenuation. The results of both models match well with the results of more complex propagation models. These approaches are: the *simple Markov chain model*, and the *adaptive sum of Markov chains model*. For simple scenarios with a stationary average number of blockers, both models work very well, and they show comparable performance. However, for non-stationary cases, i.e. the average number of blockers fluctuates, the simple Markov chain model, cannot capture the resulting attenuation directly with a single chain. However, for very complex cases, this model is less effective. The novel adaptive sum of Markov chains model, on the other hand, can be automatically adjusted to

any complex scenario. It is very computationally efficient compared with more complex models such as ray tracing or geometric models. Furthermore, unlike the simple Markov chain model that assigns a fixed attenuation value for each blocker, the novel adaptive sum of Markov chains approach can integrate any attenuation profile, including the 3GPP blockage model, and any measured attenuation profile. This significant advantage, combined with efficiency and simplicity, make the model very beneficial for network providers to undertake initial mmWave coverage studies in the presence of blockage effects. Both Markov chain models here are limited to V2I system and were applied for a single base station scenario. These suggest a potential opportunity for further investigation.

6.2.2 Small-sized Blockage Propagation Modelling for mmWave Bands

By considering the small Fresnel zones of the mmWave band, even small objects could block and severely affect the mmWave signal strength. There is a lack of literature investigating the attenuation resulting from blockers that are smaller than human bodies. This thesis carried out measurement campaigns which were to investigate the effect of five different small objects. We found that the resulting loss was in the range of 15-30 dB, which is comparable with the attenuation induced by far larger blockers. Based on these new results, we investigate the suitability of four state-of-art knife-edge diffraction (KED) blockage models for these blockers. Our results show that the third-generation partnership project (3GPP) blockage model, in general, underestimates the attenuation caused by narrow blockers, except when using the directional antenna model where the blocker is close to one of the antennas. We found that the best fit to the data is achieved by the recently developed mmMAGIC model that accounts for the phase differences of the diffracted rays in the deep shadow region behind the blocker. The work here was limited to investigate the effect of one blocker at a time.

6.2.3 Evaluation of the Signal Strength of mmWave MIMO Systems for a Multi-path Scenario in the Presence of Blockers

The third contribution brings the previous two together to undertake a comprehensive evaluation for blockage effects on the received SE for the multi-path mmWave MIMO system. Here, we apply several engineering techniques to minimise the blockage effects. Both transmitter and receiver sides contain a planar antenna array, i.e. forming a MIMO system. The Electronic beamforming is applied to have several directional beams that are steering to each possible propagating path. The results show that the dynamic blockages severely affect the received spectral efficiency. However, we found that by using the simple beam-switching technique, the blockage effects can be minimised by continually selecting the best arriving path. The evaluation work, here, was limited to the assumption that each blocker independently affects one propagated ray. Investigating the impact of having correlated propagation paths, where a blocker can affect two propagated paths simultaneously is an important future research direction.

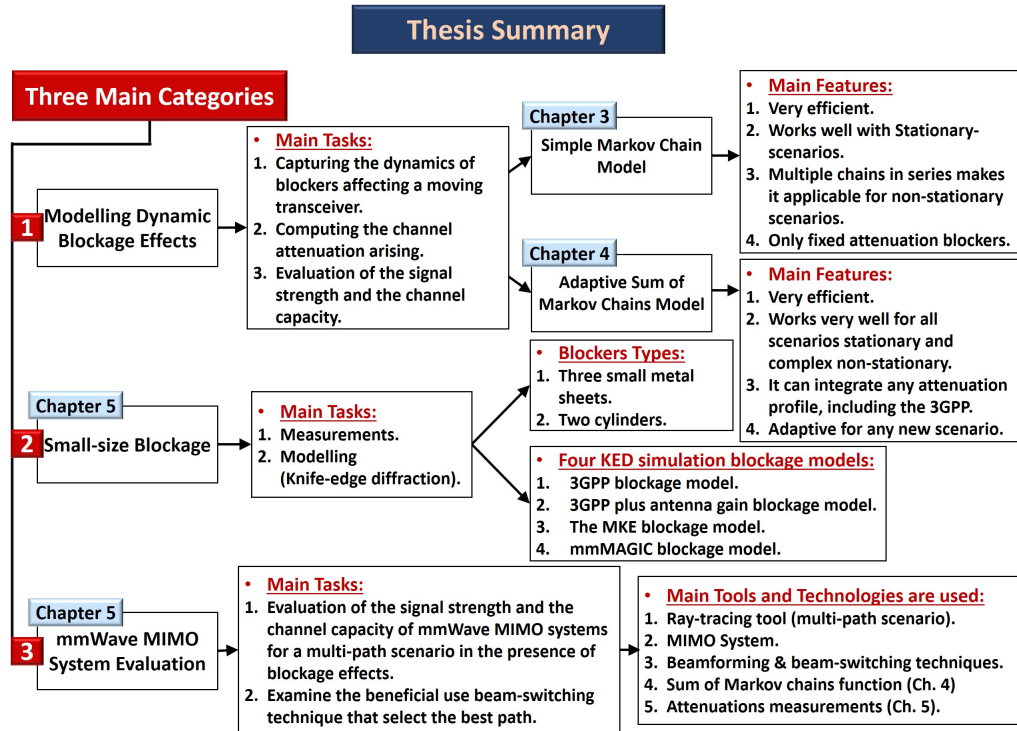


Figure 6.1: Flowchart summarises all the main points of the thesis.

All the above three main categories of this thesis are summarised in Fig. 6.1.

6.3 Future Work

Investigating mmWave signal strength and the overall system performance is a popular topic, and there are many interesting related subjects. However, here we only focus on some of the ideas that could build on the work of this thesis.

6.3.1 Multiple Transmitters and Small Cells

Across the whole thesis, all the results are based on having only one base station or transmitter. However, given that it is more likely that future mmWave communications will have ultra-dense small cells, it would be interesting to investigate the received signal strength at a moving transceiver in the presence of blockers where there are several possible base stations available. The blockage attenuation may make the blocked path from the nearest base station much weaker than the signal of a non-blocked path arriving from a further away one. Based on this, the better option is to switch to receiving from the latter base station. This research area could provide a possible extension of the work of this thesis.

6.3.2 Multiple Blocker Measurements

The blockage measurements provided in Chapter 5 are done one blocker at a time. It would be interesting to extend the results to investigate the effects of two or more blockers at one time. Also, investigating the case when one blocker is affecting two paths simultaneously.

6.3.3 The V2V Systems

Although the two proposed models – Markov chain and the sum of Markov chain – serve the V2I system, these models can also be modified to apply to more general models, such as vehicle-to-everything (V2X) systems. When both communication terminals are moving, the dynamic channel attenuation, caused by blockers, is expected to show a higher fluctuation rate than the case of V2I systems due to the simultane-

ous movement of both the transmitter and receiver. Capturing the resulting channel attenuation would be another interesting point to investigate.

Appendix A

List of Publications

A.1 Conference Papers

A.1.1 First Author

1. **F. Alsaleem**, J. S. Thompson, and D. I. Laurenson. “Markov chain for modeling 3D blockage in mmWave V2I communications”. In *2019 IEEE 89th Vehicular Technology Conference (VTC2019-Spring)*, pages 1–5, April 2019. DOI: <https://doi.org/10.1109/VTCSpring.2019.8746331>
2. **F. Alsaleem**, J. S. Thompson, D. I. Laurenson, S. K. Podilchak, and C. A. Alistarh, “Small-size blockage measurements and modelling for mmWave communications systems,” in *2020 IEEE 31st Annual International Symposium on Personal, Indoor and Mobile Radio Communications (PIMRC)*, September 2020.

A.1.2 Co-Author

1. Narengerile, **F. Alsaleem**, J. S. Thompson, and T. Ratnarajah, “Low-complexity beam training for tracking spatially consistent millimeter wave channels,” in *2020 IEEE 31st Annual International Symposium on Personal, Indoor and Mobile Radio Communications (PIMRC)*, September 2020.

A.2 Journal Papers

1. **F. Alsaleem**, J. S. Thompson, and D. I. Laurenson, “Adaptive sum of markov chains for modeling 3D blockage in mmWave V2I communications,” *IEEE Transactions on Vehicular Technology*, 2020. DOI: <https://doi.org/10.1109/TVT.2020.3003245>
2. **F. Alsaleem**, J. S. Thompson, D. I. Laurenson, S. K. Podilchak, and C. A. Alistarh, “Small-Size Blockage Propagation Modelling for mmWave Communications Systems,” *IEEE Transactions on Antennas and Propagation*, 2020, [Under Review].

The second PIMRC conference paper, under (A.1.2 Co-author) section, is not included in the thesis; however, it used the proposed Markov chain function to model the blockage effects.

References

- [1] “Nokia Networks,” https://www.lightreading.com/mobile/5g/tick-tock-or-why-5g-must-happen-soon-in-the-us/a/d-id/748918?f_src=lightreading_editorspicks_rss_latest.
- [2] M. Series, “IMT Vision–framework and overall objectives of the future development of IMT for 2020 and beyond,” *Recommendation ITU*, vol. 2083, 2015.
- [3] J. D. Parsons, *The mobile radio propagation channel*. Wiley, 2000.
- [4] S. V. Hum, “Radio and microwave wireless systems,” <http://www.waves.utoronto.ca/prof/svhum/ece422.html>, 2018.
- [5] J. Meredith, “Study on channel model for frequency spectrum above 6 GHz (release 14),” *Technical Report TR 38.900, 3GPP*, 2017.
- [6] W. C. Y. Lee., *Mobile Communications Engineering: Theory and Applications, Second Edition*. London: McGraw-Hill, 1998.
- [7] John, YA, “Calculations of knife edge diffraction model,” <http://www.raymaps.com/index.php/knife-edge-diffraction-model/>.
- [8] I. A. Hemadeh, K. Satyanarayana, M. El-Hajjar, and L. Hanzo, “Millimeter-wave communications: Physical channel models, design considerations, antenna constructions, and link-budget,” *IEEE Communications Surveys Tutorials*, vol. 20, no. 2, pp. 870–913, 2018.
- [9] J. S. Lu, D. Steinbach, P. Cabrol, and P. Pietraski, “Modeling human blockers in millimeter wave radio links,” *ZTE communications*, vol. 10, no. 4, pp. 23–28, 2012.
- [10] M. Marcus and B. Pattan, “Millimeter wave propagation: spectrum management implications,” *IEEE Microwave Magazine*, vol. 6, no. 2, pp. 54–62, 2005.

- [11] Hussam, “MIMO channel capacity,” <https://uk.mathworks.com/matlabcentral/fileexchange/30588-mimo-channel-capacity>.
- [12] V. Nurmela, A. Karttunen, A. Roivainen, L. Raschkowski, V. Hovinen, J. Y. EB, N. Omaki, K. Kusume, A. Hekkala, R. Weiler *et al.*, “Deliverable D1.4 METIS channel models,” in *Proc. Mobile Wireless Commun. Enablers Inf. Soc.(METIS)*, 2015, p. 1.
- [13] M.Jacob *et al.*, “A ray tracing based stochastic human blockage model for the IEEE 802.11ad 60 GHz channel model,” in *Proceedings of the 5th European Conference on Antennas and Propagation (EUCAP)*, April 2011, pp. 3084–3088.
- [14] F. Alsaleem, J. S. Thompson, and D. I. Laurenson, “Adaptive sum of markov chains for modelling 3D blockage in mmWave V2I communications,” *IEEE Transactions on Vehicular Technology*, 2020.
- [15] “DataReportal : Digital around the world,” <https://datareportal.com/global-digital-overview#:~:text=The%20number%20of%20mobile%20phone,in%20the%20past%2012%20months>.
- [16] “Ericsson : Ericsson mobility report: 5G subscriptions to top 2.6 billion by end of 2025,” <https://www.ericsson.com/en/press-releases/2019/11/ericsson-mobility-report-5g-subscriptions-to-top-2.6-billion-by-end-of-2025>.
- [17] F. Alsaleem, J. S. Thompson, and D. I. Laurenson, “Markov chain for modeling 3D blockage in mmWave V2I communications,” in *2019 IEEE 89th Vehicular Technology Conference (VTC2019-Spring)*, April 2019, pp. 1–5.
- [18] F. Alsaleem, J. S. Thompson, D. I. Laurenson, S. K. Podilchak, and C. A. Alistarh, “Small-size blockage measurements and modelling for mmWave communications systems,” in *2020 IEEE 31st Annual International Symposium on Personal, Indoor and Mobile Radio Communications (PIMRC)*, 2020.
- [19] F. Alsaleem, J. S. Thompson, D. I. Laurenson, S. K. Podilchak, and C. A. Alistarh, “Small-size blockage propagation modelling for mmwave communications systems,” *IEEE Transactions on Antennas and Propagation*, [Under Review].

- [20] T. S. Rappaport, R. W. Heath Jr, R. C. Daniels, and J. N. Murdock, *Millimeter wave wireless communications*. Pearson Education, 2015.
- [21] X. Wang, L. Kong, F. Kong, F. Qiu, M. Xia, S. Arnon, and G. Chen, “Millimeter wave communication: A comprehensive survey,” *IEEE Communications Surveys Tutorials*, vol. 20, no. 3, pp. 1616–1653, 2018.
- [22] F. Al-Ogaili and R. M. Shubair, “Millimeter-wave mobile communications for 5G: Challenges and opportunities,” in *2016 IEEE International Symposium on Antennas and Propagation (APSURSI)*, 2016, pp. 1003–1004.
- [23] S. Rangan, T. S. Rappaport, and E. Erkip, “Millimeter-wave cellular wireless networks: Potentials and challenges,” *Proceedings of the IEEE*, vol. 102, no. 3, pp. 366–385, 2014.
- [24] A. L. Swindlehurst, E. Ayanoglu, P. Heydari, and F. Capolino, “Millimeter-wave massive MIMO: the next wireless revolution?” *IEEE Communications Magazine*, vol. 52, no. 9, pp. 56–62, 2014.
- [25] A. Gupta and R. K. Jha, “A survey of 5G network: Architecture and emerging technologies,” *IEEE Access*, vol. 3, pp. 1206–1232, 2015.
- [26] V. Raghavan, S. Subramanian, J. Cezanne, and A. Sampath, “Directional beam-forming for millimeter-wave MIMO systems,” in *2015 IEEE Global Communications Conference (GLOBECOM)*, 2015, pp. 1–7.
- [27] T. S. Rappaport, S. Sun, R. Mayzus, H. Zhao, Y. Azar, K. Wang, G. N. Wong, J. K. Schulz, M. Samimi, and F. Gutierrez, “Millimeter wave mobile communications for 5G cellular: It will work!” *IEEE Access*, vol. 1, pp. 335–349, 2013.
- [28] E. Yaacoub, M. Hussein, and H. Ghaziri, “An overview of research topics and challenges for 5G massive MIMO antennas,” in *2016 IEEE Middle East Conference on Antennas and Propagation (MECAP)*. IEEE, 2016, pp. 1–4.

- [29] F. Boccardi, R. W. Heath, A. Lozano, T. L. Marzetta, and P. Popovski, “Five disruptive technology directions for 5G,” *IEEE Communications Magazine*, vol. 52, no. 2, pp. 74–80, 2014.
- [30] S. Mumtaz, J. Rodriguez, and L. Dai, *MmWave Massive MIMO: A Paradigm for 5G*. Academic Press, 2016.
- [31] T. Bai, A. Alkhateeb, and R. W. Heath, “Coverage and capacity of millimeter-wave cellular networks,” *IEEE Communications Magazine*, vol. 52, no. 9, pp. 70–77, 2014.
- [32] J. G. Andrews, S. Buzzi, W. Choi, S. V. Hanly, A. Lozano, A. C. K. Soong, and J. C. Zhang, “What will 5G be?” *IEEE Journal on Selected Areas in Communications*, vol. 32, no. 6, pp. 1065–1082, 2014.
- [33] B. Loong Ng, “3GPP 5G NR millimeter wave standards,” in *Proceedings of the 1st ACM Workshop on Millimeter-Wave Networks and Sensing Systems 2017*, 2017, pp. 25–25.
- [34] Remy Pascal, “Verizon’s new 5G fixed–wireless access proposition aims to attract cable cord-cutters,” https://www.analysysmason.com/globalassets/x_migrated-media/media/analysys_mason_verizon_fwa_offer_oct2018_rdmb03.pdf.
- [35] J. Foerster, J. Lansford, J. Laskar, T. Rappaport, and S. Kato, “Realizing gbps wireless personal area networks - guest editorial,” *IEEE Journal on Selected Areas in Communications*, vol. 27, no. 8, pp. 1313–1317, 2009.
- [36] C. Park and T. S. Rappaport, “Short-range wireless communications for next-generation networks: UWB, 60 GHz millimeter-wave WPAN, and ZigBee,” *IEEE Wireless Communications*, vol. 14, no. 4, pp. 70–78, 2007.
- [37] O. Abari, D. Bharadia, A. Duffield, and D. Katabi, “Cutting the cord in virtual reality,” in *Proceedings of the 15th ACM Workshop on Hot Topics in Networks*, ser. HotNets ’16. New York, NY, USA: Association for Computing Machinery, 2016, p. 162–168. [Online]. Available: <https://doi.org/10.1145/3005745.3005770>

- [38] L. Hobert *et al.*, “Enhancements of V2X communication in support of cooperative autonomous driving,” *IEEE Communications Magazine*, vol. 53, no. 12, pp. 64–70, December 2015.
- [39] P. B. Papazian *et al.*, “Study of the local multipoint distribution service radio channel,” *IEEE Transactions on Broadcasting*, vol. 43, no. 2, pp. 175–184, 1997.
- [40] World Health Organization, “Road traffic injuries fact sheet,” <http://www.who.int/mediacentre/factsheets/fs358/en/>, 2016.
- [41] L. Kong *et al.*, “Millimeter-wave wireless communications for IoT-Cloud supported autonomous vehicles: Overview, design, and challenges,” *IEEE Communications Magazine*, vol. 55, no. 1, pp. 62–68, January 2017.
- [42] D. T. Paris and F. K. Hurd, *Basic electromagnetic theory*. McGraw-Hill Companies, 1969.
- [43] J. A. Richards, *Radio Wave Propagation*. Springer-Verlag Berlin Heidelberg, Germany: Springer, 2008.
- [44] E. C. Jordan and K. G. Balmain, *Electromagnetic waves and radiating systems*. Prentice-Hall, 1968.
- [45] H. T. Friis, “A note on a simple transmission formula,” *Proceedings of the IRE*, vol. 34, no. 5, pp. 254–256, 1946.
- [46] A. V. Alejos, M. G. Sanchez, and I. Cuinas, “Measurement and analysis of propagation mechanisms at 40 GHz: Viability of site shielding forced by obstacles,” *IEEE Transactions on Vehicular Technology*, vol. 57, no. 6, pp. 3369–3380, 2008.
- [47] J. Griffiths, *Radio Wave Propagation and Antennas*. Prentice-Hall intern. Englewood Cliffs (NJ) et al, 1987.
- [48] T. S. Rappaport, *Wireless communications: Principles and practice*, 2nd ed., ser. Prentice Hall communications engineering and emerging technologies series. Prentice Hall, 2002, includes bibliographical references and index.

- [49] S. Cerwin, *Radio Propagation and Antennas: A Non-Mathematical Treatment of Radio and Antennas*. Bloomington: Author House, 2019.
- [50] J. Walfisch and H. L. Bertoni, "A theoretical model of UHF propagation in urban environments," *IEEE Transactions on Antennas and Propagation*, vol. 36, no. 12, pp. 1788–1796, 1988.
- [51] Y. Niu *et al.*, "A survey of millimeter wave (mmWave) communications for 5G: Opportunities and challenges," *Wireless Networks*, vol. 21, no. 8, pp. 2657–2676, 2015. [Online]. Available: <https://doi.org/10.1007/s11276-015-0942-z>
- [52] F. Giannetti, M. Luise, and R. Reggiannini, "Mobile and personal communications in the 60 GHz band: A survey," *Wirel. Pers. Commun.*, vol. 10, no. 2, p. 207–243, July 1999. [Online]. Available: <https://doi.org/10.1023/A:1018308429332>
- [53] M. Zhadobov, N. Chahat, R. Sauleau, C. Le Quement, and Y. Le Drian, "Millimeter-wave interactions with the human body: State of knowledge and recent advances," *International Journal of Microwave and Wireless Technologies*, vol. 3, no. 2, pp. 237–247, 2011.
- [54] F. Khan and Z. Pi, "mmWave mobile broadband (MMB): Unleashing the 3–300GHz spectrum," in *34th IEEE Sarnoff Symposium*, 2011, pp. 1–6.
- [55] E. Violette, R. Espeland, and K. C. Allen, "Millimeter-wave propagation characteristics and channel performance for urban-suburban environments," *NASA STI/Recon Technical Report N*, vol. 89, 1988.
- [56] J. Wells, "Faster than fiber: The future of multi-G/s wireless," *IEEE Microwave Magazine*, vol. 10, no. 3, pp. 104–112, 2009.
- [57] F. C. Commission *et al.*, "Millimeter wave propagation: spectrum management implications," *Bulletin*, vol. 70, pp. 1–24, 1997.
- [58] Recommendation, ITURP, "838-3. specific attenuation model for rain for use in prediction methods," *ITU-R Recommendations, P Series Fascicle, ITU, Geneva, Switzerland*, 2005.

- [59] Z. Pi and F. Khan, "An introduction to millimeter-wave mobile broadband systems," *IEEE Communications Magazine*, vol. 49, no. 6, pp. 101–107, 2011.
- [60] E. Violette, R. Espeland, and K. C. Allen, "Millimeter-wave propagation characteristics and channel performance for urban-suburban environments," *NASA STI/Recon Technical Report N*, vol. 89, 1988.
- [61] Y. S. Meng and Y. H. Lee, "Investigations of foliage effect on modern wireless communication systems: A review," *Progress In Electromagnetics Research*, vol. 105, pp. 313–332, 2010.
- [62] H. Zhao, R. Mayzus, S. Sun, M. Samimi, J. K. Schulz, Y. Azar, K. Wang, G. N. Wong, F. Gutierrez, and T. S. Rappaport, "28 GHz millimeter wave cellular communication measurements for reflection and penetration loss in and around buildings in New York city," in *2013 IEEE International Conference on Communications (ICC)*, 2013, pp. 5163–5167.
- [63] J. Ryan, G. R. MacCartney, and T. S. Rappaport, "Indoor office wideband penetration loss measurements at 73 GHz," in *2017 IEEE International Conference on Communications Workshops (ICC Workshops)*, 2017, pp. 228–233.
- [64] A. N. Uwaechia and N. M. Mahyuddin, "A comprehensive survey on millimeter wave communications for fifth-generation wireless networks: Feasibility and challenges," *IEEE Access*, vol. 8, pp. 62 367–62 414, 2020.
- [65] E. J. Violette, R. H. Espeland, R. O. DeBolt, and F. K. Schwing, "Millimeter-wave propagation at street level in an urban environment," *IEEE Transactions on Geoscience and Remote Sensing*, vol. 26, no. 3, pp. 368–380, 1988.
- [66] A. S. Abdulrasool, J. S. Aziz, and S. J. Abou-Loukh, "Calculation algorithm for diffraction losses of multiple obstacles based on epstein–peterson approach," *International Journal of Antennas and Propagation*, vol. 2017, 2017.
- [67] S. Nie, G. R. MacCartney, S. Sun, and T. S. Rappaport, "72 GHz millimeter wave indoor measurements for wireless and backhaul communications," in *2013 IEEE 24th Annual International Symposium on Personal, Indoor, and Mobile Radio Communications (PIMRC)*. IEEE, 2013, pp. 2429–2433.

- [68] R. J. Weiler, M. Peter, W. Keusgen, K. Sakaguchi, and F. Undi, "Environment induced shadowing of urban millimeter-wave access links," *IEEE Wireless Communications Letters*, vol. 5, no. 4, pp. 440–443, 2016.
- [69] C. E. Shannon, "Communication in the presence of noise," *Proceedings of the IRE*, vol. 37, no. 1, pp. 10–21, 1949.
- [70] D. Tse and P. Viswanath, *Fundamentals of wireless communication*. Cambridge University Press, 2005.
- [71] F. Rusek, D. Persson, B. K. Lau, E. G. Larsson, T. L. Marzetta, O. Edfors, and F. Tufvesson, "Scaling up MIMO: Opportunities and challenges with very large arrays," *IEEE Signal Processing Magazine*, vol. 30, no. 1, pp. 40–60, 2013.
- [72] T. L. Marzetta, "Noncooperative cellular wireless with unlimited numbers of base station antennas," *IEEE Transactions on Wireless Communications*, vol. 9, no. 11, pp. 3590–3600, 2010.
- [73] A. J. PAULRAJ, D. A. GORE, R. U. NABAR, and H. BOLCSKEI, "An overview of MIMO communications - a key to gigabit wireless," *Proceedings of the IEEE*, vol. 92, no. 2, pp. 198–218, 2004.
- [74] E. Biglieri, R. Calderbank, A. Constantinides, A. Goldsmith, A. Paulraj, and H. V. Poor, *MIMO wireless communications*. Cambridge University Press, 2007.
- [75] A. Kaushik, *Energy efficient and low complexity techniques for the next generation millimeter wave hybrid MIMO systems*. The University of Edinburgh, 2020.
- [76] O. Y. Kolawole, *On the performance of hybrid beamforming for millimeter wave wireless networks*. The University of Edinburgh, 2019.
- [77] P. F. Smulders and L. Correia, "Characterisation of propagation in 60 GHz radio channels," *Electronics & communication engineering journal*, vol. 9, no. 2, pp. 73–80, 1997.

- [78] H. Xu, V. Kukshya, and T. S. Rappaport, “Spatial and temporal characteristics of 60-GHz indoor channels,” *IEEE Journal on selected areas in communications*, vol. 20, no. 3, pp. 620–630, 2002.
- [79] A. Goldsmith, *Wireless communications*. Cambridge University Press, 2005.
- [80] R. Mohammadkhani, *Adaptive impedance matching to compensate mutual coupling effects on compact MIMO systems*. The University of Edinburgh, 2012.
- [81] O. E. Ayach, S. Rajagopal, S. Abu-Surra, Z. Pi, and R. W. Heath, “Spatially sparse precoding in millimeter wave MIMO systems,” *IEEE Transactions on Wireless Communications*, vol. 13, no. 3, pp. 1499–1513, 2014.
- [82] M. K. Samimi and T. S. Rappaport, “Ultra-wideband statistical channel model for non line of sight millimeter-wave urban channels,” in *2014 IEEE Global Communications Conference*. IEEE, 2014, pp. 3483–3489.
- [83] J. S. Bloch, J. Bloch, and L. L. Hanzo, *Third-generation systems and intelligent wireless networking: smart antennas and adaptive modulation*. John Wiley & Sons, 2002.
- [84] A. N. Uwaechia, N. M. Mahyuddin, M. F. Ain, N. M. Abdul Latiff, and N. F. Za’bah, “On the spectral-efficiency of low-complexity and resolution hybrid precoding and combining transceivers for mmWave MIMO systems,” *IEEE Access*, vol. 7, pp. 109 259–109 277, 2019.
- [85] Junyi Wang, Zhou Lan, Chang-woo Pyo, T. Baykas, Chin-sean Sum, M. A. Rahman, Jing Gao, R. Funada, F. Kojima, H. Harada, and S. Kato, “Beam codebook based beamforming protocol for multi-Gbps millimeter-wave WPAN systems,” *IEEE Journal on Selected Areas in Communications*, vol. 27, no. 8, pp. 1390–1399, 2009.
- [86] X. An, C. Sum, R. V. Prasad, J. Wang, Z. Lan, J. Wang, R. Hekmat, H. Harada, and I. Niemegeers, “Beam switching support to resolve link-blockage problem in 60 GHz WPANs,” in *2009 IEEE 20th International Symposium on Personal, Indoor and Mobile Radio Communications*, 2009, pp. 390–394.

- [87] G. R. MacCartney, S. Deng, S. Sun, and T. S. Rappaport, "Millimeter-wave human blockage at 73 GHz with a simple double knife-edge diffraction model and extension for directional antennas," in *2016 IEEE 84th Vehicular Technology Conference (VTC-Fall)*, September 2016, pp. 1–6.
- [88] M. Peter *et al.*, "Measurement results and final mmMAGIC channel models," *Deliverable D2*, vol. 2, p. 12, 2017. [Online]. Available: https://bscw.5g-mmmagic.eu/pub/bscw.cgi/d202656/mmMAGIC_D2-2.pdf
- [89] "IEEE Standard for information technology– local and metropolitan area networks– specific requirements– part 15.3: Amendment 2: Millimeter-wave-based alternative physical layer extension," *IEEE Std 802.15.3c-2009 (Amendment to IEEE Std 802.15.3-2003)*, pp. 1–200, 2009.
- [90] A. Maltsev, R. Maslennikov, A. Sevastyanov, A. Lomayev, and A. Khoryaev, "Statistical channel model for 60 GHz WLAN systems in conference room environment," in *Proceedings of the Fourth European Conference on Antennas and Propagation*, 2010, pp. 1–5.
- [91] M. R. Akdeniz, Y. Liu, M. K. Samimi, S. Sun, S. Rangan, T. S. Rappaport, and E. Erkip, "Millimeter wave channel modeling and cellular capacity evaluation," *IEEE Journal on Selected Areas in Communications*, vol. 32, no. 6, pp. 1164–1179, 2014.
- [92] M. K. Samimi, S. Sun, and T. S. Rappaport, "MIMO channel modeling and capacity analysis for 5G millimeter-wave wireless systems," in *2016 10th European Conference on Antennas and Propagation (EuCAP)*, 2016, pp. 1–5.
- [93] M. K. Samimi and T. S. Rappaport, "3-D millimeter-wave statistical channel model for 5G wireless system design," *IEEE Transactions on Microwave Theory and Techniques*, vol. 64, no. 7, pp. 2207–2225, 2016.
- [94] A. Maltsev *et al.*, "D5. 1-Channel modeling and characterization," *MiWEBA Project (FP7-ICT-608637), Public Deliverable*, 2014.
- [95] S. Jaeckel, L. Raschkowski, K. Börner, and L. Thiele, "QuaDRiGa: A 3-D multi-cell channel model with time evolution for enabling virtual field trials,"

- IEEE Transactions on Antennas and Propagation*, vol. 62, no. 6, pp. 3242–3256, 2014.
- [96] “Millimetre wave transmission (MWT): Applications and use cases of millimetre wave transmission,” https://www.etsi.org/deliver/etsi_gs/mWT/001_099/002/01.01.01_60/gs_mWT002v010101p.pdf, August 2015.
- [97] “Millimetre wave transmission (MWT): Analysis of antennas for millimetre wave transmission. European Telecommunications Standards Institute.” https://www.etsi.org/deliver/etsi_gs/mWT/001_099/006/01.01.01_60/gs_mWT006v010101p.pdf, December 2015.
- [98] “Millimetre wave transmission (MWT): V-band street level interference analysis. European Telecommunications Standards Institute,” https://www.etsi.org/deliver/etsi_gs/mWT/001_099/004/01.01.01_60/gs_mWT004v010101p.pdf, June 2016.
- [99] S. Niknam, B. Natarajan, and R. Barazideh, “Interference analysis for finite-area 5G mmWave networks considering blockage effect,” *IEEE Access*, vol. 6, pp. 23 470–23 479, 2018.
- [100] I. K. Jain, R. Kumar, and S. Panwar, “Driven by capacity or blockage? a millimeter wave blockage analysis,” in *2018 30th International Teletraffic Congress (ITC 30)*, vol. 01, September 2018, pp. 153–159.
- [101] B. Han *et al.*, “A 3D human body blockage model for outdoor millimeter-wave cellular communication,” *Physical Communication*, vol. 25, pp. 502–510, 2017. [Online]. Available: <https://doi.org/10.1016/j.phycom.2017.10.008>
- [102] M. Gapeyenko, A. Samuylov, M. Gerasimenko, D. Moltchanov, S. Singh, M. Akdeniz, E. Aryafar, S. Andreev, N. Himayat, and Y. Koucheryavy, “Spatially-consistent human body blockage modeling: A state generation procedure,” *IEEE Transactions on Mobile Computing*, pp. 1–1, 2019.
- [103] M. Abouelseoud and G. Charlton, “The effect of human blockage on the performance of millimeter-wave access link for outdoor coverage,” in *2013 IEEE 77th Vehicular Technology Conference (VTC Spring)*, June 2013, pp. 1–5.

- [104] M. Gapeyenko, A. Samuylov, M. Gerasimenko, D. Moltchanov, S. Singh, E. Aryafar, S. Yeh, N. Himayat, S. Andreev, and Y. Koucheryavy, “Analysis of human-body blockage in urban millimeter-wave cellular communications,” in *2016 IEEE International Conference on Communications (ICC)*, May 2016, pp. 1–7.
- [105] K. Haneda, J. Zhang, L. Tan, G. Liu, Y. Zheng, H. Asplund, J. Li, Y. Wang, D. Steer, C. Li, T. Balercia, S. Lee, Y. Kim, A. Ghosh, T. Thomas, T. Nakamura, Y. Kakishima, T. Imai, H. Papadopoulos, T. S. Rappaport, G. R. MacCartney, M. K. Samimi, S. Sun, O. Koymen, S. Hur, J. Park, C. Zhang, E. Mellios, A. F. Molisch, S. S. Ghassamzadeh, and A. Ghosh, “5G 3GPP-Like channel models for outdoor urban microcellular and macrocellular environments,” in *2016 IEEE 83rd Vehicular Technology Conference (VTC Spring)*, 2016, pp. 1–7.
- [106] M. Gapeyenko, A. Samuylov, M. Gerasimenko, D. Moltchanov, S. Singh, M. R. Akdeniz, E. Aryafar, N. Himayat, S. Andreev, and Y. Koucheryavy, “On the temporal effects of mobile blockers in urban millimeter-wave cellular scenarios,” *IEEE Transactions on Vehicular Technology*, vol. 66, no. 11, pp. 10 124–10 138, 2017.
- [107] C. Slezak *et al.*, “Empirical effects of dynamic human-body blockage in 60 GHz communications,” *IEEE Communications Magazine*, vol. 56, no. 12, pp. 60–66, December 2018.
- [108] I. K. Jain, R. Kumar, and S. S. Panwar, “The impact of mobile blockers on millimeter wave cellular systems,” *IEEE Journal on Selected Areas in Communications*, vol. 37, no. 4, pp. 854–868, April 2019.
- [109] V. Semkin *et al.*, “Estimation of optimum antenna configurations supported by realistic propagation models at 60 GHz,” in *The 8th European Conference on Antennas and Propagation (EuCAP 2014)*, April 2014, pp. 3434–3438.
- [110] V. Degli-Esposti *et al.*, “Ray-tracing-based mm-Wave beamforming assessment,” *IEEE Access*, vol. 2, pp. 1314–1325, 2014.

- [111] E. N. Gilbert, "Capacity of a burst-noise channel," *The Bell System Technical Journal*, vol. 39, no. 5, pp. 1253–1265, 1960.
- [112] P. Sadeghi, R. A. Kennedy, P. B. Rapajic, and R. Shams, "Finite-state Markov modeling of fading channels - a survey of principles and applications," *IEEE Signal Processing Magazine*, vol. 25, no. 5, pp. 57–80, 2008.
- [113] R. Prieto-Cerdeira, F. Perez-Fontan, P. Burzigotti, A. Bolea-Alamañac, and I. Sanchez-Lago, "Versatile two-state land mobile satellite channel model with first application to DVB-SH analysis," *International Journal of Satellite Communications and Networking*, vol. 28, no. 5-6, pp. 291–315, 2010.
- [114] N. Mhearain and F. S. Dunwoody, "A statistical model for the dual polarised mimo land mobile satellite channel at s-band," Ph.D. dissertation, Heriot-Watt University, 2018.
- [115] M. LLC, " PGoogle's self-driving car gathers nearly 1Gb/Sec," <https://www.kurzweilai.net/googles-self-driving-car-gathers-nearly-1-gbsec>.
- [116] N. Lu *et al.*, "Connected vehicles: Solutions and challenges," *IEEE Internet of Things Journal*, vol. 1, no. 4, pp. 289–299, August 2014.
- [117] G. Pocovi, M. Lauridsen, B. Soret, K. I. Pedersen, and P. Mogensen, "Automation for on-road vehicles: Use cases and requirements for radio design," in *2015 IEEE 82nd Vehicular Technology Conference (VTC2015-Fall)*, 2015, pp. 1–5.
- [118] H. Seo *et al.*, "LTE evolution for vehicle-to-everything services," *IEEE Communications Magazine*, vol. 54, no. 6, pp. 22–28, June 2016.
- [119] J. Choi *et al.*, "Millimeter wave vehicular communication to support massive automotive sensing," *CoRR*, vol. abs/1602.06456, 2016. [Online]. Available: <http://arxiv.org/abs/1602.06456>
- [120] V. Va, J. Choi, and R. W. Heath, "The impact of beamwidth on temporal channel variation in vehicular channels and its implications," *IEEE Transactions on Vehicular Technology*, vol. 66, no. 6, pp. 5014–5029, 2017.

- [121] J. M. Kelner and C. Ziolkowski, "Multi-elliptical geometry of scatterers in modeling propagation effect at receiver," in *Antennas and Wave Propagation*, P. Pinho, Ed. Rijeka: IntechOpen, 2018. [Online]. Available: <https://doi.org/10.5772/intechopen.75142>
- [122] P. Kyösti, J. Meinilä, L. Henttilä, X. Zhao, T. Jämsä, C. Schneider, M. Narandzić, M. Milojević, A. Hong, J. Ylitalo, V.-M. Holappa, M. Alatossava, R. Bultitude, Y. Jong, and T. Rautiainen, "IST-4-027756 WINNER II D1.1.2 v1.2 WINNER II channel models," *Inf. Soc. Technol*, vol. 11, February 2008.
- [123] Z. Yun and M. F. Iskander, "Ray tracing for radio propagation modeling: Principles and applications," *IEEE Access*, vol. 3, pp. 1089–1100, 2015.
- [124] W. C. Y. Lee, "Estimate of local average power of a mobile radio signal," *IEEE Transactions on Vehicular Technology*, vol. 34, no. 1, pp. 22–27, 1985.
- [125] S. Dehnie, "Markov chain approximation of rayleigh fading channel," in *2007 IEEE International Conference on Signal Processing and Communications*, November 2007, pp. 1311–1314.
- [126] I. Kashiwagi, T. Taga, and T. Imai, "Time-varying path-shadowing model for indoor populated environments," *IEEE Transactions on Vehicular Technology*, vol. 59, no. 1, pp. 16–28, January 2010.
- [127] G. R. MacCartney, T. S. Rappaport, and S. Rangan, "Rapid fading due to human blockage in pedestrian crowds at 5G millimeter-wave frequencies," in *GLOBE-COM 2017 - 2017 IEEE Global Communications Conference*, December 2017, pp. 1–7.
- [128] R. Ford, S. Rangan, E. Mellios, D. Kong, and A. Nix, "Markov channel-based performance analysis for millimeter wave mobile networks," in *2017 IEEE Wireless Communications and Networking Conference (WCNC)*, 2017, pp. 1–6.
- [129] A. Samuylov, M. Gapeyenko, D. Moltchanov, M. Gerasimenko, S. Singh, N. Himayat, S. Andreev, and Y. Koucheryavy, "Characterizing spatial correla-

- tion of blockage statistics in urban mmWave systems,” in *2016 IEEE Globecom Workshops (GC Wkshps)*, 2016, pp. 1–7.
- [130] M. Boban, X. Gong, and W. Xu, “Modeling the evolution of line-of-sight blockage for V2V channels,” in *2016 IEEE 84th Vehicular Technology Conference (VTC-Fall)*, 2016, pp. 1–7.
- [131] D. C. Hogg, “Fun with the Friis free-space transmission formula,” *IEEE Antennas and Propagation Mag.*, vol. 35, no. 4, pp. 33–35, 1993.
- [132] P. Brémaud, “Shannon’s capacity theorem. in: Discrete probability models and methods. probability theory and stochastic modelling,” *Springer, Cham*, vol. 78, 2017.
- [133] “Markov chains,” <http://www.imperial.ac.uk/~ejm/M3S4/NOTES3.pdf>.
- [134] J. Rocca, “Introduction to Markov chains,” <https://towardsdatascience.com/brief-introduction-to-markov-chains-2c8cab9c98ab>.
- [135] V. N. Gudivada, D. Rao, and V. V. Raghavan, “Chapter 9 - Big data driven natural language processing research and applications,” in *Big Data Analytics*, ser. Handbook of Statistics, V. Govindaraju, V. V. Raghavan, and C. Rao, Eds. Elsevier, 2015, vol. 33, pp. 203 – 238. [Online]. Available: <http://www.sciencedirect.com/science/article/pii/B9780444634924000095>
- [136] F. Gebali, *Reducible Markov Chains*. Boston, MA: Springer US, 2008, pp. 1–32. [Online]. Available: https://doi.org/10.1007/978-0-387-74437-7_5
- [137] R. Billinton and R. Allan, “Discrete Markov chains. in: Reliability evaluation of engineering systems,” *Springer, Boston, MA*, 1983.
- [138] S. Singh *et al.*, “Blockage and directivity in 60 GHz wireless personal area networks: from cross-layer model to multihop MAC design,” *IEEE Journal on Selected Areas in Communications*, vol. 27, no. 8, pp. 1400–1413, October 2009.

- [139] C. Gustafson, K. Haneda, S. Wyne, and F. Tufvesson, "On mm-Wave multipath clustering and channel modeling," *IEEE Transactions on Antennas and Propagation*, vol. 62, no. 3, pp. 1445–1455, March 2014.
- [140] M. Jacob *et al.*, "Extension and validation of the IEEE 802.11ad 60 GHz human blockage model," in *2013 7th European Conference on Antennas and Propagation (EuCAP)*, April 2013, pp. 2806–2810.
- [141] M. Jacob *et al.*, "Fundamental analyses of 60 GHz human blockage," in *2013 7th European Conference on Antennas and Propagation (EuCAP)*, April 2013, pp. 117–121.
- [142] Y. Dalveren, A. H. Alabish, and A. Kara, "A simplified model for characterizing the effects of scattering objects and human body blocking indoor links at 28 GHz," *IEEE Access*, vol. 7, pp. 69 687–69 691, 2019.
- [143] S. H. Aftabi Momo and M. Munjure Mowla, "Effect of human blockage on an outdoor mmWave channel for 5G communication networks," in *2019 22nd International Conference on Computer and Information Technology (ICCIT)*, 2019, pp. 1–6.
- [144] X. Zhao, Q. Wang, S. Li, S. Geng, M. Wang, S. Sun, and Z. Wen, "Attenuation by human bodies at 26- and 39.5-GHz millimeter wavebands," *IEEE Antennas and Wireless Propagation Letters*, vol. 16, pp. 1229–1232, 2017.
- [145] W. Qi *et al.*, "Measurements and modeling of human blockage effects for multiple millimeter wave bands," in *2017 13th International Wireless Communications and Mobile Computing Conference (IWCMC)*, June 2017, pp. 1604–1609.
- [146] T. Bai and R. W. Heath, "Analysis of self-body blocking effects in millimeter wave cellular networks," in *2014 48th Asilomar Conference on Signals, Systems and Computers*, 2014, pp. 1921–1925.
- [147] K. Venugopal, M. C. Valenti, and R. W. Heath, "Analysis of millimeter wave networked wearables in crowded environments," in *2015 49th Asilomar Conference on Signals, Systems and Computers*, 2015, pp. 872–876.

- [148] J. S. Romero-Peña and N. Cardona, “Applicability limits of simplified human blockage models at 5G mm-Wave frequencies,” in *2019 13th European Conference on Antennas and Propagation (EuCAP)*, March 2019, pp. 1–5.
- [149] T. S. Rappaport, R. W. Heath Jr, R. C. Daniels, and J. N. Murdock, *Millimeter wave wireless communications*. Englewood Cliffs, NJ, USA: Pearson Education, 2015.
- [150] A. Thornburg, T. Bai, and R. W. Heath, “Performance analysis of outdoor mmWave Ad Hoc networks,” *IEEE Transactions on Signal Processing*, vol. 64, no. 15, pp. 4065–4079, 2016.
- [151] A. K. Gupta, J. G. Andrews, and R. W. Heath, “Macrodiversity in cellular networks with random blockages,” *IEEE Transactions on Wireless Communications*, vol. 17, no. 2, pp. 996–1010, 2018.
- [152] K. Venugopal, M. C. Valenti, and R. W. Heath, “Device-to-device millimeter wave communications: Interference, coverage, rate, and finite topologies,” *IEEE Transactions on Wireless Communications*, vol. 15, no. 9, pp. 6175–6188, 2016.
- [153] P. Mogensen *et al.*, “LTE capacity compared to the Shannon bound,” in *2007 IEEE 65th Vehicular Technology Conference - VTC2007-Spring*, April 2007, pp. 1234–1238.
- [154] T. Bai, R. Vaze, and R. W. Heath, “Analysis of blockage effects on urban cellular networks,” *IEEE Transactions on Wireless Communications*, vol. 13, no. 9, pp. 5070–5083, 2014.
- [155] Feldman, Joel, “JoelFel’s Webpage,” <http://www.math.ubc.ca/~feldman/>.
- [156] C. Seker, M. T. Güneser, and T. Ozturk, “A review of millimeter wave communication for 5G,” in *2018 2nd International Symposium on Multidisciplinary Studies and Innovative Technologies (ISMSIT)*, October 2018, pp. 1–5.

- [157] M. K. Samimi and T. S. Rappaport, “3-D millimeter-wave statistical channel model for 5G wireless system design,” *IEEE Transactions on Microwave Theory and Techniques*, vol. 64, no. 7, pp. 2207–2225, 2016.
- [158] S. Sun, G. R. MacCartney, M. K. Samimi, and T. S. Rappaport, “Synthesizing omnidirectional antenna patterns, received power and path loss from directional antennas for 5G millimeter-wave communications,” in *2015 IEEE Global Communications Conference (GLOBECOM)*, December 2015, pp. 1–7.
- [159] S. Sun, T. S. Rappaport, R. W. Heath, A. Nix, and S. Rangan, “MIMO for millimeter-wave wireless communications: beamforming, spatial multiplexing, or both?” *IEEE Communications Magazine*, vol. 52, no. 12, pp. 110–121, 2014.
- [160] T. W. C. Brown and M. Khalily, “Integrated shield edge diffraction model for narrow obstructing objects,” *IEEE Transactions on Antennas and Propagation*, vol. 66, no. 12, pp. 6588–6595, 2018.
- [161] V. Raghavan, A. Partyka, L. Akhoondzadeh-Asl, M. A. Tassoudji, O. H. Koy-men, and J. Sanelli, “Millimeter wave channel measurements and implications for PHY layer design,” *IEEE Transactions on Antennas and Propagation*, vol. 65, no. 12, pp. 6521–6533, 2017.
- [162] C. Gustafson and F. Tufvesson, “Characterization of 60 GHz shadowing by human bodies and simple phantoms,” in *2012 6th European Conference on Antennas and Propagation (EUCAP)*, March 2012, pp. 473–477.
- [163] A. G. Aguilar, P. H. Pathak, and M. Sierra-Pérez, “A canonical UTD solution for electromagnetic scattering by an electrically large impedance circular cylinder illuminated by an obliquely incident plane wave,” *IEEE Transactions on Antennas and Propagation*, vol. 61, no. 10, pp. 5144–5154, October 2013.
- [164] J. Kunisch and J. Pamp, “Ultra-wideband double vertical knife-edge model for obstruction of a ray by a person,” in *2008 IEEE International Conference on Ultra-Wideband*, vol. 2, September 2008, pp. 17–20.

- [165] J. Medbo and F. Harrysson, “Channel modeling for the stationary UE scenario,” in *2013 7th European Conference on Antennas and Propagation (EuCAP)*, April 2013, pp. 2811–2815.
- [166] J. George R. MacCartney and T. S. Rappaport, “Millimeter-wave base station diversity and human blockage in dense urban environments for coordinated multi-point (CoMP),” NYU Tandon School of Engineering, NYU WIRELESS, NYU Tandon School of Engineering, 2 MetroTech Center, Brooklyn, NY 11201, Tech. Rep. NYU WIRELESS TR 2018-002, May 2018.
- [167] U. T. Virk and K. Haneda, “Modeling human blockage at 5G millimeter-wave frequencies,” *IEEE Transactions on Antennas and Propagation*, pp. 1–1, 2019.
- [168] V. Raghavan, L. Akhoondzadeh-Asl, V. Podshivalov, J. Hulten, M. A. Tassoudji, O. H. Koymen, A. Sampath, and J. Li, “Statistical blockage modeling and robustness of beamforming in millimeter-wave systems,” *IEEE Transactions on Microwave Theory and Techniques*, vol. 67, no. 7, pp. 3010–3024, 2019.
- [169] V. Raghavan, S. Noimanivone, S. K. Rho, B. Farin, P. Connor, R. A. Motos, Y.-C. Ou, K. Ravid, M. A. Tassoudji, O. H. Koymen, and J. Li, “Hand and body blockage measurements with form-factor user equipment at 28 ghz,” 2019.
- [170] N. Tran, T. Imai, and Y. Okumura, “Study on characteristics of human body shadowing in high frequency bands: Radio wave propagation technology for future radio access and mobile optical networks,” in *2014 IEEE 80th Vehicular Technology Conference (VTC2014-Fall)*, 2014, pp. 1–5.
- [171] X. Chen, L. Tian, P. Tang, and J. Zhang, “Modelling of human body shadowing based on 28 GHz indoor measurement results,” in *2016 IEEE 84th Vehicular Technology Conference (VTC-Fall)*, 2016, pp. 1–5.
- [172] S. Collonge, G. Zaharia, and G. E. Zein, “Influence of the human activity on wide-band characteristics of the 60 GHz indoor radio channel,” *IEEE Transactions on Wireless Communications*, vol. 3, no. 6, pp. 2396–2406, November 2004.

- [173] J. D. Kraus and K. R. Karver, *Electromagnetics*. Mc Graw-Hill, 1973.
- [174] B. Neekzad, K. Sayrafian-Pour, J. Perez, and J. S. Baras, “Comparison of ray tracing simulations and millimeter wave channel sounding measurements,” in *2007 IEEE 18th International Symposium on Personal, Indoor and Mobile Radio Communications*, 2007, pp. 1–5.
- [175] EM.CUBE Company, “EM Terrano program WiKi,” <http://www.emagtech.com/wiki/index.php?title=EM.Terrano>.
- [176] Narengerile, F. Alsaleem, J. S. Thompson, and T. Ratnarajah, “Low-complexity beam training for tracking spatially consistent millimeter wave channels,” in *2020 IEEE 31st Annual International Symposium on Personal, Indoor and Mobile Radio Communications (PIMRC)*, 2020.
- [177] J. Rocca, “Everything RF,” <https://www.everythingrf.com/rf-calculators/antenna-near-field-distance-calculator>.
- [178] T. S. Rappaport, G. R. MacCartney, S. Sun, H. Yan, and S. Deng, “Small-scale, local area, and transitional millimeter wave propagation for 5G communications,” *IEEE Transactions on Antennas and Propagation*, vol. 65, no. 12, pp. 6474–6490, 2017.
- [179] T. Mavridis, L. Petrillo, J. Sarrazin, D. Lautru, A. Benlarbi-Delai, and P. De Doncker, “Creeping wave model of diffraction of an obliquely incident plane wave by a circular cylinder at 60 GHz,” *IEEE Transactions on Antennas and Propagation*, vol. 62, no. 3, pp. 1372–1377, 2014.
- [180] L. Piazzzi and H. L. Bertoni, “Effect of terrain on path loss in urban environments for wireless applications,” *IEEE Transactions on Antennas and Propagation*, vol. 46, no. 8, pp. 1138–1147, 1998.